

Zsolt SzilvÁgyi

Dynamic Soil Properties of Danube Sands

PhD Dissertation

Supervisor:

Professor Dr. Richard P. Ray PhD

Department of Structural and Geotechnical Engineering

Faculty of Architecture, Civil Engineering and Transport Sciences

Széchenyi István University

Modeling and Development of Infrastructural Systems

Multidisciplinary Doctoral School of Engineering Sciences

Széchenyi István University

Győr, Hungary

2018

Acknowledgments

First, I would like to extend my appreciation and gratitude to my supervisor, Prof. Richard P. Ray. He introduced me to the challenging topics of soil dynamics and laboratory testing and guided me through this research with valuable oversight, while allowing the very necessary independent research as well.

I would also like to thank Dr. Robert Szepeshazi, for bringing me into his Geotechnical Workshop in Gyor. Our collective work induced great professional challenges and has resulted in many fruitful discussions and exciting experiences. I would like to express my gratitude to my colleagues in Gyor at the Department of Structural and Geotechnical Engineering, especially Akos Wolf, Dr. Edina Koch, Peter Hudacsek and Dr. Orsolya Kegyes-Brassai for all their help and collaboration.

I would also like to thank my fellow PhD student, Jakub Panuska, from the Department of Geotechnics at the Slovak University of Technology, for his always-positive attitude and for the enormous work that he contributed to our mutual research papers.

Finally, my sincere thanks to my family for their love and support; and for encouraging me to challenge myself repeatedly.

Summary

This PhD dissertation concerns with the dynamic behavior of Danube Sands. Recently in Hungary the adaptation of Eurocode 8 standard has created a greater need to define dynamic behavior of local soils such as Danube Sands. Seismicity in Hungary can be considered moderate, however expected earthquake loading could cause serious damage in structures and infrastructure, therefore engineers need to consider it in design. Due to the fact, that the previous Hungarian design standards did not consider earthquake loading, there has not been any research focusing on soil dynamics in Hungary, and their lack hinders economic design and construction of engineering structures, and the precise specification of local earthquake risk.

In order to obtain information about the response of Danube Sands to dynamic and cyclic loading, state-of-the art laboratory measurement methods have been applied and the most important properties needed to describe dynamic behavior were measured. The laboratory investigations included the use of the Resonant Column test method and the Torsional Simple Shear test method. Both methods are used widely around the world for dynamic laboratory testing, however they have not been used before in Hungary. The device used for testing can be considered unique worldwide, since it is capable of performing both tests on a single hollow cylinder soil specimen, while commonly used devices are usually capable of performing only one type of test. The most important feature of the behavior of soil subjected to dynamic loading is that deformation response is depending on the induced level of deformations. In other words stiffness is depending on strain and their relationship is highly nonlinear. The biggest advantage of the combined device used in this study, is the capability of measuring soil response over a very wide range of strains, which makes it possible to define soil behavior more precisely.

The specific scope of the study was to measure the very small strain stiffness, the stiffness degradation and the damping characteristics of Danube Sands and to obtain correlations which describe how these parameters depend on state variables. This was achieved by the development of measurement data interpretation procedures, comparison of measurement results to existing correlations and development of correlations to better describe these local soils. Since the measurement techniques are quite complex, data interpretation is an important task in the procedure. Interpretation includes the task of choosing material model parameters which requires the solution of an inverse problem. To solve the problem, a thorough literature review on the modeling of small strain stiffness had to be performed and a procedure was developed which allows obtaining parameters of a nonlinear material model, the Ramberg-Osgood model, based on the laboratory measurement results.

Összefoglalás

Disszertációm Dunai homokok dinamikus viselkedésével foglalkozik. Hazánkban az Eurocode 8 szabvány bevezetése miatt jelentős igény merült fel a helyi talajok dinamikus viselkedésének leírására. A földrengésveszély Magyarországon mérsékeltnek tekinthető, ugyanakkor a várható földrengések komoly károkat okozhatnak szerkezeteinkben és az infrastruktúra hálózatban, ezért a mérnöki tervezés során figyelembe kell venni a földrengésterhet. Mivel a korábbi magyar szabványok nem számoltak ezzel a teherrel, a talajdinamika témaköréhez kapcsolódó hazai kutatás eddig még nem volt. A témára vonatkozó kutatások hiánya nem csak a szerkezetek gazdaságos tervezését és kivitelezését gátolja, de nehezíti a földrengésveszély helyi értékének pontos meghatározását is.

Kutatásomban a legkorszerűbb laboratóriumi mérési módszereket alkalmaztam tipikus Dunai homokok dinamikus és ciklikus terhelésekre adott válaszának jellemzéséhez és megmértem a dinamikus viselkedés leírásához szükséges legfontosabb talajjellemzőket. Laboratóriumi méréseim Rezonanciás vizsgálatból és Torziós Nyírásvizsgálatból álltak. Mindkét mérési módszer fejlett dinamikai laboratóriumi mérési módszernek számít az egész világon, ugyanakkor Magyarországon még nem használták egyiket sem. A kutatáshoz használt és továbbfejlesztett mérőberendezés pedig világszinten is egyedinek számít, mivel a két mérési módszert egyetlen üreges hengeres talajmintán képes egymás után alkalmazni, míg az elterjedt berendezések szinte mind csak az egyik mérést képesek elvégezni. A dinamikus terhelésnek kitett talajok viselkedésének legfontosabb jellemzője, hogy a terhelés okozta elmozdulások mértéke függ az elmozdulások nagyságától. Másképp megfogalmazva, a talaj merevsége függ a fajlagos alakváltozásoktól és a kettejük közötti kapcsolat erősen nemlineáris. A kutatáshoz használt és továbbfejlesztett berendezés legnagyobb előnye, hogy a talaj dinamikus teherre adott válaszáat a fajlagos alakváltozások mértékének széles tartományában képes megmérni és ez által pontosabban le lehet írni a talaj viselkedését.

Kutatásom legfőbb célja volt tipikus Dunai homokok nagyon kis alakváltozások tartományában érvényes nyírási modulusának mérése, továbbá a modulus növekvő alakváltozások melletti leromlási és a csillapítási jellemzőinek mérése, valamint olyan korrelációk felállítása, melyek leírják, hogyan függnek ezek a mennyiségek a befolyásoló állapotjellemzőktől. Ehhez szükséges volt a mérési eredmények interpretációjának továbbfejlesztése, valamint a mérési eredményeket össze kellett vetni meglévő, szakirodalomban található korrelációkkal és felállítani új korrelációkat, amelyek jobban leírják ilyen talajok viselkedését. Mivel a mérési módszerek meglehetősen bonyolultak, az eredmények interpretációja fontos feladata a folyamatnak. Ebbe bele tartozik a választott anyagmodell paramétereinek megválasztása is, amely egy inverz

feladat megoldst igrnyli. A megoldshoz irodalomkutatst vgeztem a kis alakvltozsok esetn rvnyes, nemlineris modulus modellezsre vonatkozan s kidolgoztam egy eljrst, amellyel a nemlineris Ramberg-Osgood anyagmodell paramterei pontosan meghatrozhatok a laboratriumi mrsi eredmnyek alapjn.

Contents:

1	Introduction	1
1.1	Background	1
1.2	Scope of study and organization of thesis	3
1.3	Research methodology	4
2	Dynamic behavior of soils	5
2.1	Small strain nonlinearity	7
2.1.1	Modeling small strain nonlinearity	11
2.1.2	Equivalent linear model.....	13
2.1.3	Modeling irreversible small strain behavior.....	17
2.1.4	Modified Ramberg-Osgood model.....	18
2.2	Measurement of dynamic soil properties	22
2.2.1	In-situ tests	23
2.2.2	Laboratory tests	26
2.3	Determination of dynamic soil parameters based on correlations	28
2.3.1	Small strain stiffness	29
2.3.2	Modulus reduction.....	35
2.3.3	Damping	42
3	RC-TOSS testing	44
3.1	Basic testing concepts of RC and TOSS	44
3.2	Device.....	46
3.3	Sample preparation.....	49
3.4	Interpretation of measurement results	50
3.5	Application of measurement results in numerical modeling.....	55
4	Testing program and results	65
4.1	Materials investigated and test matrix.....	65
4.2	Measured G_{max} compared to correlations from literature and BE.....	69
4.3	Modulus reduction curves	82
4.4	Damping curves.....	97
5	Thesis statements.....	110
5.1	Thesis #1	111
5.2	Thesis #2	111
5.3	Thesis #3	112
5.4	Thesis #4	112

5.5 Thesis #5	113
6 Summary and future research	113
References	115
List of figures	124
List of symbols	128
Annex A – Device assembly and sample preparation for RC-TOSS testing	a
Annex B – Developed Visual Basic codes	s
Annex C – RC-TOSS measurement results	w

1 Introduction

"The finding that at small strains the ground exhibits high stiffness and, frequently, nonlinear properties, has far-reaching practical and fundamental consequences. ...nonlinearity of stress-strain response has very significant effects on soil-structure interaction, stress distributions in the soil mass, and displacement profiles around loaded areas and excavations. ...There is enormous scope for the development of improved instruments and techniques and for the experimental study of stiffness properties of soils and weak rocks at small strains." (Burland, 1989)

"The limit of classical laboratory testing coincides ... with characteristic shear strains that can be measured near geotechnical structures. However, the soil stiffness that should be used in the analysis of geotechnical structures is not the one that relates to these final strains. Instead, very small-strain soil stiffness and its non-linear dependency on strain amplitude should be properly taken into account in all analysis that strive for reliable predictions of displacements." (Benz, 2006)

1.1 Background

The adaptation of Eurocode 8 for seismic design and the continuous development of the rail system in Hungary have created a greater need to define dynamic behavior of local soil groups. Seismic design includes geotechnical and structural engineering tasks e.g. design of foundations, retaining structures, buildings and other engineering structures for earthquake loads; as well as earthquake engineering tasks e.g. site response evaluation, seismic risk assessment etc. Most of these tasks require knowledge about dynamic behavior of soils to some extent. Seismic design and earthquake engineering are challenging tasks for the designer. Earthquake loading acts over a very short period of time compared to other loads and its rare occurrence makes it difficult to gather useful design data.

This is especially true in Hungary where seismic risk can be considered moderate, but it is high enough to impose a risk, which engineers must address. Meeting the especially strict design criteria concerning vibrations and settlements set for high-speed rails also require comprehensive knowledge about geotechnical dynamic modeling. This topic will gain more attention in the near future since the development of the Hungarian high-speed rail system is essential and will be required from us by the European Union. Due to these tendencies, several topics of seismic design have been studied in Hungary recently, such as in-situ geophysical measurement methods (Toros, 2006), (Kegyes-Brassai, Ray, & Tildy, 2015); seismic design of struc-

tures (Zsarnoczay, 2014), (Simon & Vigh, 2017), (Ther & Kollar, 2017); and liquefaction assessment (Ban, Katona, & Mahler, 2016); however, measurement and modeling of local soils under dynamic loading has never been studied yet.

Recently, the importance of numerical modeling in geotechnical engineering has increased greatly in research studies and everyday practice as well. As a result, geotechnical material models have developed tremendously to meet the increasing demands of numerical modeling. On the one hand, this is a result of the rapid and continuous progress of computer technology; on the other hand, the many advantages of achieving more accurate and economical solutions help these approaches become more widespread. Generally, models developed for scientific calculations tend to get implemented into commercial software faster and faster.

However, another tendency can be observed in Hungary, and perhaps elsewhere, that it is difficult to convince clients to spend on elaborate laboratory testing programs even in larger projects. This may be due to a lack of appreciation of the complexities of geotechnical modeling by engineers from related fields; they don't understand the difficulties or the benefits of a more sophisticated model. It is the author's hope that this study will help practicing engineers understand, how material models can be used to describe the dynamic behavior of soils and how small strain stiffness can be assessed in the laboratory. Besides, since there is often no room in the project for complex and time-consuming laboratory testing, the study will also provide correlations which can be used to estimate dynamic material parameters of soils similar to those tested and analyzed in this study.

In the past 7-8 years, a research team has been formed at the Department of Structural and Geotechnical Engineering at Szechenyi Istvan University under the supervision of Prof. Richard P. Ray. My research focuses on laboratory testing and modeling connected to small strain stiffness of a typical local granular soil, while other team members consider related topics, such as: earthquake hazard analysis and seismic risk assessment of existing buildings (Kegyes-Brassai, 2016), pile foundations under seismic loading (Wolf & Ray, 2017) and finite element modeling of dynamic loading of trains (Koch & Hudacsek, 2017).

For the research presented in my Dissertation, the continuous development of the Geotechnical Laboratory was essential, especially the improvement of the combined Resonant Column-Torsional Simple Shear device which was built by Prof. Ray at the University of Michigan (Ray R. P., 1983) and rebuilt, recalibrated and further developed by the author at the Geotechnical Laboratory of Szechenyi Istvan University with the supervision of Prof. Ray.

1.2 *Scope of study and organization of thesis*

The scope of the study concerns laboratory testing and modeling of selected granular soils from Hungary. Danube sands compose an important segment of local soils and present the geotechnical engineer with several design challenges. These soils are present at river crossings and major development parcels throughout Hungary. Although their engineering behavior can vary over a wide range, they retain some common characteristics that will help the engineer make decisions about geotechnical and structural designs. Field and laboratory measurements are usually complex and time consuming. In practice, the designer often has to use existing correlations derived from testing of various soils. Therefore, my research aims to answer the following questions:

- Is there a material model available, which may be used to model the dynamic behavior of Danube sands?
- Can existing correlations be used to obtain reliable material parameters for the model?
- How can the dynamic properties of Danube sands be quantified by laboratory measurements?

To answer these questions, a logical order of general theory, literature review, laboratory testing methods and equipment, data interpretation and finally test results and discussion will be presented.

In Chapter 2, first the dynamic behavior of soils is discussed from a theoretical point-of-view. Then applicable soil models are presented and the measurement methods for model parameters are detailed together with a review of literature on correlations. The aim of this chapter is to introduce the reader to the modeling of small strain nonlinearity for soils as well as draw attention to appropriate correlations for dynamic soil properties of sands and provide insight about likely errors involved from such estimations.

Chapter 3 first presents the basic testing methodology used for the Resonant Column and Torsional Shear testing. Next, the laboratory testing device used in this study is described and testing procedure is presented. Then, since data interpretation is very important in this challenging field of measurements, it is shown how measured data can be turned into material parameters. Finally, as the last step of interpretation, the inverse problem of obtaining model parameters for a numerical model is solved and presented within the finite element modeling of a Torsional Shear Test.

Chapter 4 presents the performed comprehensive laboratory testing program, starting with the description and index parameters of the selected typical Danube sands. Then main

results of the measurements are summarized and compared to correlations from literature. Three main branches of results are presented separately: small strain stiffness, modulus degradation and damping of the soils are described. The summary of a comprehensive study is also shown, which concerned the comparison of the test results to an independent set of laboratory measurements made with Bender Elements at the Slovak University of Technology in Bratislava by an independent researcher.

Summary of findings and thesis statements are given in Chapter 5.

Device assembly and sample preparation is further detailed in Annex A. Developed VBA codes for data interpretation are given in Annex B. All laboratory test results are documented in Annex C.

1.3 Research methodology

In order to provide background to the topic of the research and to gather existing correlations for the dynamic properties of soils, a comprehensive literature review has been performed. The review focused on two main topics: the theoretical description of modeling the dynamic behavior of soils, and correlations for obtaining material model parameters for sands.

The research consisted of an extensive laboratory measurement program; two laboratory measurement methods (Resonant Column Test and Torsional Simple Shear Test) have been used to obtain information about the dynamic behavior of nine selected Danube sands. Both methods are considered state-of-the-art in the field of geotechnical earthquake engineering and while they are used all over the world, in Hungary this research is the first to apply them. It also has to be noted that most measurement devices use either the Resonant Column or the Torsional Shear method for testing. In contrast to them, the device used and improved in this study is a combined one, capable of performing both tests on a single specimen, which makes it rather unique. The benefit of combined testing is that the soil response can be measured throughout the whole range of strains from very small strains (10^{-4} %) up to large strains (10^{-1} %) on one single specimen. Analysis of the data and interpretation of results are the most important steps in the measurement procedure, hence this study focused on both of them. Visual Basic for Applications in MS Excel has been used to improve measurement result interpretation; the developed codes are presented in the Annex of the thesis.

Applying a material model to the measured set of data is also an important task and can be considered as another method of measurement data interpretation. For simple cases, this task is often done with the trial and error method, while complex models require solving an inverse

problem. Some programs used for geotechnical finite element modeling (e.g. Plaxis) provide built-in tools (Soil Test module) to perform this task for commonly used laboratory tests and material models, however there is no such tool available for any of the two laboratory measurement methods or any material model which considers the small strain stiffness of soils. Therefore, in order to obtain material parameters that provide the best fit for a certain model, a procedure has been developed to solve the inverse problem and provide material parameters by regression analysis based on measured behavior. For this MS Excel Solver's Generalized Reduced Gradient method was used to minimize the sum of residual squares between values provided by the model and measured values.

Finally, to preview the solution of the inverse problem, a 3 dimensional finite element model has been developed and the modeling of several loading stages of the Torsional Shear Test has been performed using the Ramberg-Osgood material model. Analysis results are compared to measurement results to provide verification of the material model implemented in the computer program used.

2 Dynamic behavior of soils

A couple of decades ago geotechnical engineers thought that deformation of soils should be separately assessed for the dynamic and static loading cases. Distinction has been made between a so-called dynamic and static modulus. It was thought, that the former is only valid for dynamic calculations and has no relation with the latter, which is used for traditional geotechnical problems, which consider larger and permanent strains. At that time, soil response for dynamic loading was thought to be linear elastic.

Based on this approach laboratory observations were used to estimate the ratio of these moduli for different soil types, see e.g. Figure 2-1. Correlations like this are still popular, since they seem easy to use; similar graphs can still be found in handbooks, see (DGGT, 2001) or (Smolczyk, 2002). However, this method of interpretation of static and dynamic modulus could lead to serious under- or overestimation of the dynamic modulus; see the comprehensive discussion by (Wichtmann & Triantafyllidis, 2009).

Later more precise static laboratory measurements revealed that the higher stiffness is not connected to dynamic loading (i.e. the frequency of loading), but to the achieved strain amplitude. These observations were made first in the 1980s when triaxial laboratory tests were per-

formed at Imperial College, London (Burland, 1989), with strains measured locally on the sample. Earlier the standard testing method suggested to measure strains externally between the end platens. The concept and basic findings are summarized in Figure 2-2.

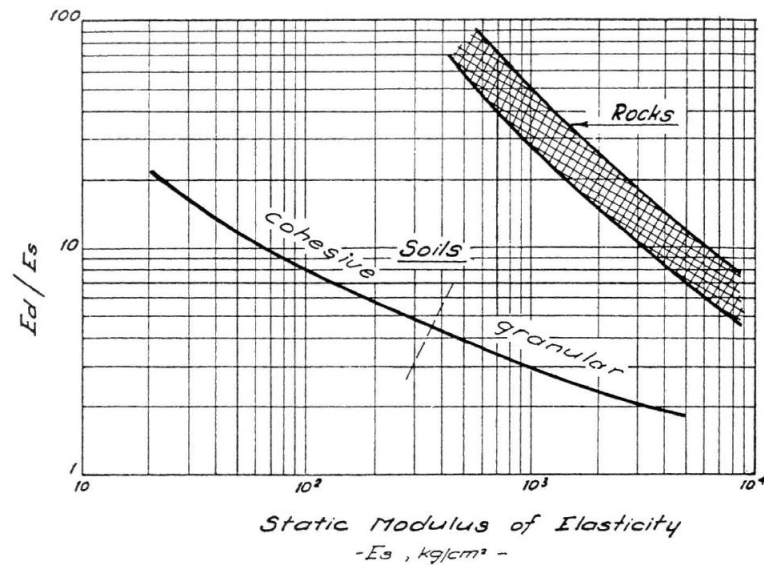


Figure 2-1 Ratio of dynamic and static moduli presented by (Alpan, 1970)

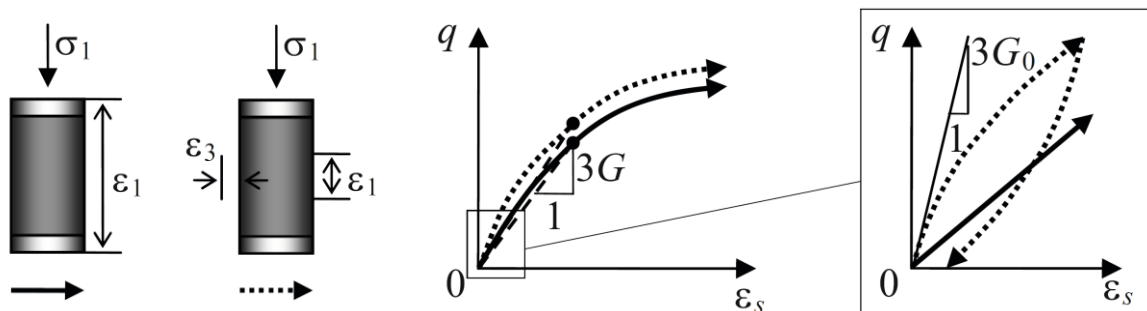


Figure 2-2 External and local measurements in a triaxial test: setup (left) and deviatoric stress-strain curves with zoom into small strains (right) (Puzrin, 2012)

The obtained deviatoric stress-strain curves are close to each other, but when focusing on the very small strains (up to 0.01-0.1%) the curve of the local strain measurement (dashed) is highly nonlinear while the curve of the external strain measurement (solid) is almost linear. Beside this, the initial tangent shear modulus G_0 is almost an order of magnitude higher than the pre-yielding secant modulus, G . They also found that even at small strains, stress-strain behavior is not entirely reversible; some very small permanent strain was measured (showed by dashed unloading curve in Figure 2-2). These observations were very important, because in many practical geotechnical calculations deformations are overestimated. This might be due to the fact, that in classical geotechnical problems large strains only appear in a relatively small

volume of the soil. The strains in the remaining part of the model are very small, but to calculate displacements, strains are integrated over a relatively large area and the contribution of small strains can be significant. Therefore, ignoring the stiffer small strain response will lead to over-estimation of displacements in geotechnical calculations.

As measurement techniques further developed, a transition from the small strain stiffness or dynamic stiffness and the static stiffness has been observed. Further, more precise laboratory test results made it clear, that a limit of strains can be found experimentally, above which soils exhibit damping and non-linear stiffness response, therefore the assumption of linear elasticity is no longer valid; and that larger strain response is connected through the so-called modulus degradation or modulus reduction curve, which introduced the concept of strain dependent stiffness.

2.1 Small strain nonlinearity

Recently many studies have shown that the accurate modeling of stiffness degradation with strain is a key aspect in many dynamic as well as static geotechnical numerical calculations (e.g. earthquake vibrations, high-speed railway induced vibrations, settlement calculations around retaining walls or tunnels etc.). It has been recognized, that soils behave linear-elastically only at very low strains (10^{-6} or 10^{-4} %) and as the strains (and stresses) increase, the initially constant shear stiffness or as they often call it in literature, small strain stiffness (G_{max} or G_0) decreases gradually, as shown in Figure 2-3, while damping or hysteretic behavior becomes more pronounced. Decrease of the stiffness is caused by separation or slippage of intergranular contacts as shear strain increases, which means these contacts contribute less and less to the elastic stiffness of the assembly. However, if cyclic loading is performed, after load reversal the reduction disappears, as previously slipping contacts re-engage in the opposite direction. Naturally, if loading is continued in this direction, elastic contacts will once again be lost and stiffness will reduce as before.

Modulus reductions to 5-10% of the original, low-strain value are common. The strain level, at which this stiffness degradation starts is called threshold level and depends on soil type. If the strains in the soil increase above this level, non-linear behavior can be observed.

This very small strain level is typical in earthquake induced waves and different kinds of vibrations. It is well known, that the released energy of the earthquake induces seismic waves

that propagate in the rock and soil volume (primary/compression/p-waves and secondary/shear/s-waves) and on the ground surface (Rayleigh waves and Love waves), see Figure 2-4.

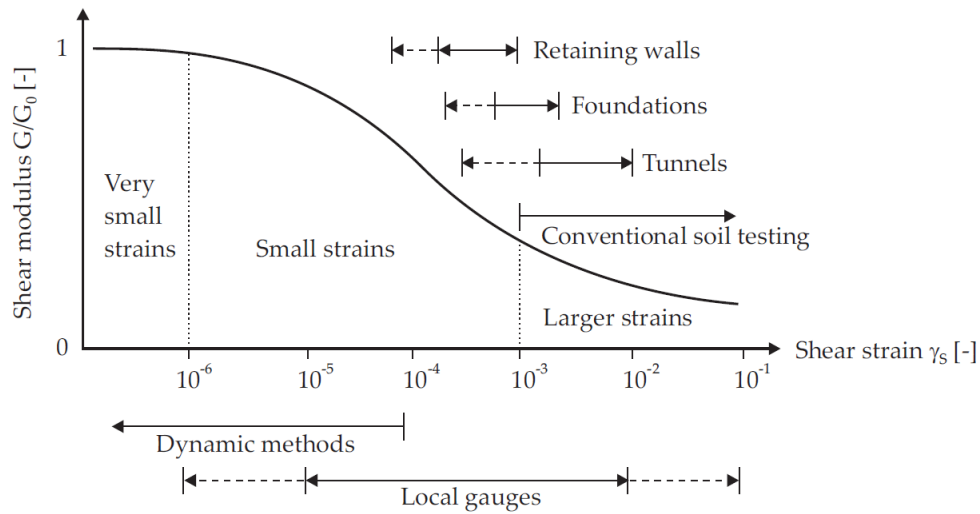


Figure 2-3 Stiffness degradation of soil with typical strain ranges after (Atkinson & Salfors, 1991)

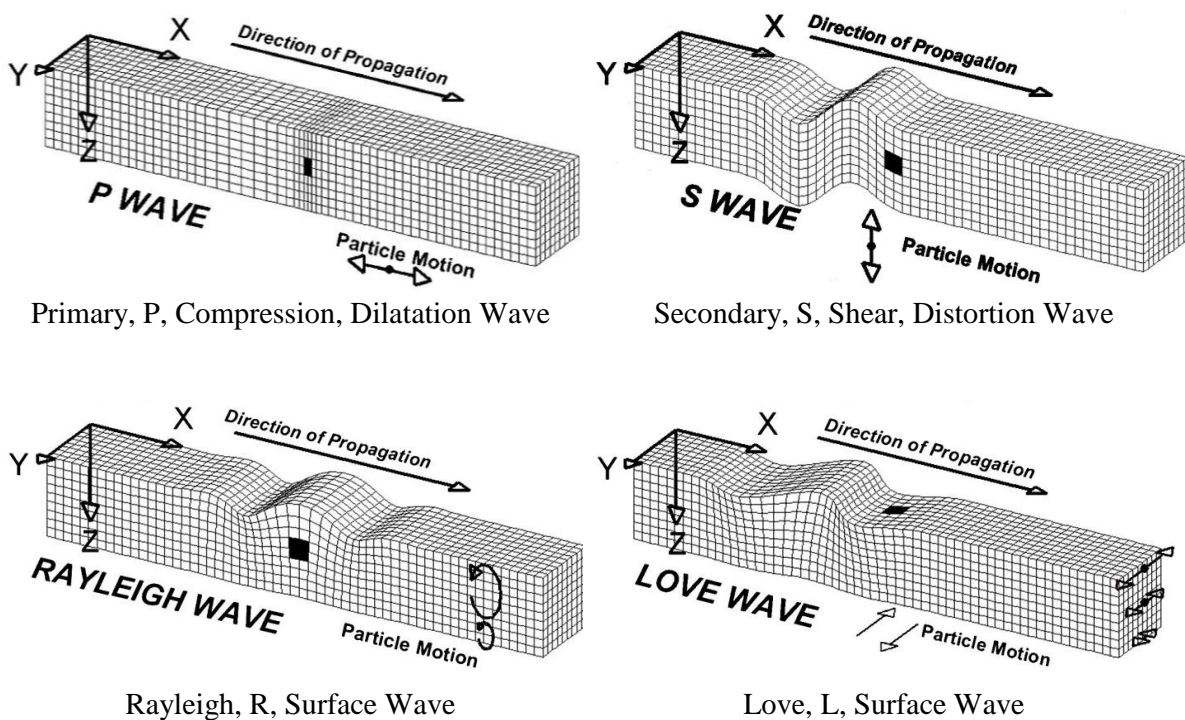


Figure 2-4 Seismic waves (original image by Prof. L. Braile ©)

The most important waves from an engineering point-of-view are shear waves, as they carry a considerable amount of the energy and they interact with engineering structures in a

very destructive way. These waves tend to refract on layer boundaries and when propagating to the ground surface, they usually exit stiffer and enter into softer layers; hence they tend to lean more and more upwards. As a result, when getting in interaction with engineering structures they are usually already almost vertically propagating, horizontally polarized shear waves; which induce horizontal shear strains in the soil, as shown in Figure 2-5. This is one of the main reasons that the description of small strain stiffness is approached usually by introducing shear modulus and shear strain level.

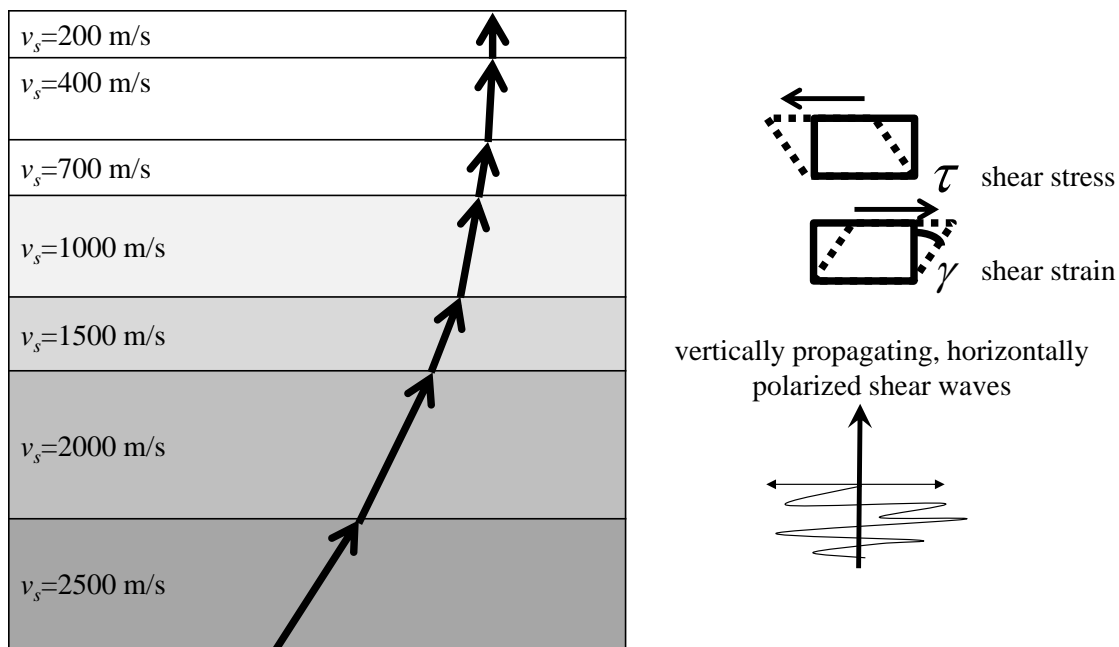


Figure 2-5 Propagation of shear waves in layered medium and induced deformation

A detailed discussion about the small strain stiffness of soils is presented in the Rankine lecture of (Clayton, 2011) where first the historical development of elastic theory and the constitutive frameworks for its use in soil modeling is elaborated. Afterwards it is shown, how the comprehensive theoretical description of anisotropic elasticity can be simplified for practical calculations regarding soils. It should be emphasized, that beside anisotropy, several other factors have an effect on both the small strain stiffness and the stiffness at larger strains.

The most important factors that affect small strain stiffness are:

- void ratio
- grain properties (grain size and shape)
- effective overburden stress
- stress history
- rate of loading

- structure and fabric of soil
- discontinuities

Factors that control the degradation of stiffness at larger strains are:

- strain level
- loading path (change in effective stress)
- destructuring
- change in rate of loading

Some of these factors can be assessed by detailed laboratory investigations, however in many practical cases there is no room for such elaborate testing, hence simplifications are made i.e. some factors are neglected. As (Clayton, 2011) discussed it, anisotropy may have a significant effect in overconsolidated soils. Rate effects are now considered relatively unimportant at very small strain levels. At higher strain levels, however three main effects connected to strain rates can be observed. The first one is that the elastic range, where small strain stiffness can be observed increases with strain rate. Because of this tests with different strain rate (e.g. resonant column and cyclic triaxial tests) tend to show different stiffness degradation at small strains. Second, shear stiffness depends on the strain rate the most at intermediate strains, i.e. between 10^{-2} % and 10^{-1} % strain. Last, tests with higher strain rates (e.g. resonant column) are likely to provide a lower limit for the degradation curve when compared to other test methods with lower strain rates. The effects of structure and fabric are more difficult to describe, for soils exhibiting these features, detailed field investigations can be suggested. The remaining factors can be investigated in laboratory in detail and several approaches have already been presented for specific soils in literature for handling them, see (Kramer, 1995), (Benz, 2006) and (Clayton, 2011).

Naturally, the three-phase model for soils, where the soil mass is considered to consist of solid particles, groundwater and air in the voids, can be applied within this modeling task too. A distinction should be made between the ‘undrained’, ‘short term’ or ‘end of construction’ case and the ‘drained’, ‘long term’ or ‘total stress’ case. It should be noted that the shear stiffness remains the same in the undrained and drained cases, since shearing usually involves change in shape without change in volume and the contribution of water to shear stiffness is negligible at low rates of strain. However, other elastic parameters (Young’s modulus, Poisson’s ratio, bulk modulus) depend significantly on whether the effective or total stress approach is used for their determination.

2.1.1 Modeling small strain nonlinearity

Several analytical functions have been considered for curve-fitting the deviatoric stress-strain behavior of soils at small strains in literature. The two most often mentioned are the hyperbolic and the Ramberg-Osgood function; see (Puzrin, 2012). Because nonlinearity is most dominant in the small strain range the normalization of stress-strain curves is often used in these models (Puzrin, 2012). After reaching a limiting deviatoric stress q_L the stress strain curve can be approximated well enough with by a straight line with the inclination $3G_L$, which is then followed up to the yield stress q_y . G_L is the tangent shear modulus corresponding to q_L . Then normalization of the curve by q_L is done and an analytical function is used to describe the behavior up to q_L , this is shown in Figure 2-6.

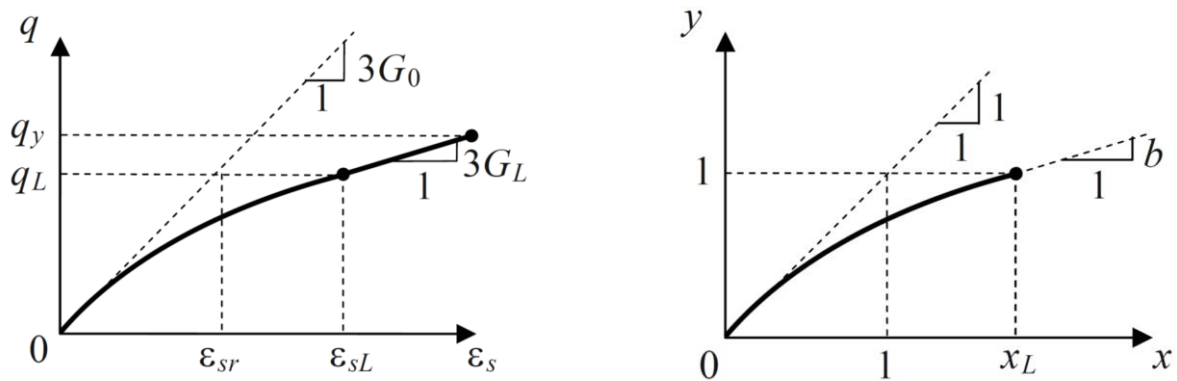


Figure 2-6 Deviatoric stress-strain curve: true (left) and normalized (right) (Puzrin, 2012)

For the normalization, the following notation is used:

$$y = \frac{q}{q_L}, \quad x = \frac{\varepsilon_s}{\varepsilon_{sr}}, \quad \varepsilon_{sr} = \frac{q_L}{3G_0}, \quad x_L = \frac{\varepsilon_{sL}}{\varepsilon_{sr}} \quad \text{Equation 2-1}$$

where y and x are the normalized deviator stress and strain, respectively; G_0 is the initial tangent shear modulus; x_L is the normalized limiting shear strain. A similar normalization is used with the hyperbolic function, which is implemented into the Hardening Soil model where q_L is taken as 90% of q_y (Benz, 2006). The way this normalization is used will be shown more in detail for the Ramberg-Osgood model in Chapter 2.1.4.

As mentioned before in most nonlinear cyclic stress-strain models the relationship between the shear stress and shear strain is defined; and this is usually done by setting up two basic functions: an initial loading curve and a hysteresis loop. The initial nonlinear loading curve can be expressed in the form:

$$\tau = f(\gamma) \quad \text{Equation 2-2}$$

where τ is shear stress and γ is shear strain.

This relationship is usually obtained from some kind of monotonic loading test. If the load at a given (τ_p, γ_p) turnaround point is then reversed, the formulation of the hysteresis loop is used, which is derived from the original function as follows:

$$\frac{\tau - \tau_p}{2} = f\left(\frac{\gamma - \gamma_p}{2}\right) \quad \text{Equation 2-3}$$

This implies that the curve of the unloading and opposite direction loading is the same shape as the initial loading curve, but it is stretched by a factor of 2, see Figure 2-7. This is because previously slipping contacts must first recoil elastically until they are unloaded. Then, if the loading in the opposite direction is continued, they will distort backward by the same amount. After a second load reversal at this second turnaround point $(-\tau_p, -\gamma_p)$, the hysteresis curve is formed. This third part of the curve can be calculated by:

$$\frac{\tau + \tau_p}{2} = f\left(\frac{\gamma - \gamma_p}{2}\right) \quad \text{Equation 2-4}$$

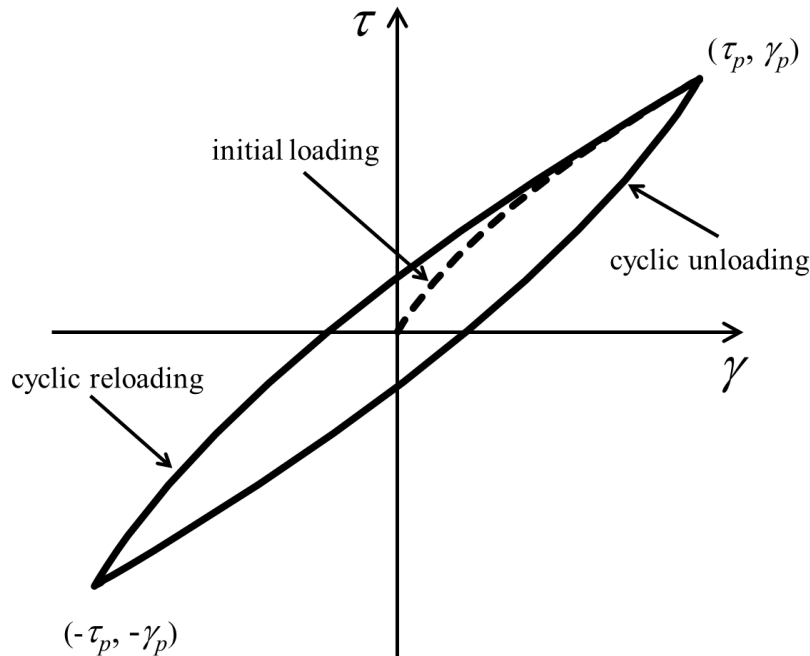


Figure 2-7 Nonlinear stress-strain curve for initial loading and hysteresis curve for cyclic loading

The hysteresis loop is formed with always keeping track of the last turnaround point which will be the origin for the next half loop. This means during cyclic harmonic loading the

origin of loading will not be reached any more. Each point of the initial loading curve (shown dashed in Figure 2-7) can be considered to be a turnaround point of a smaller hysteresis loop and it is also called backbone curve or skeleton curve (Ishihara, 1996). The rule of formulating the hysteresis curve as described above is called the Masing rule. A more detailed elaboration about this is given in Chapter 2.1.3.

Hysteretic behavior is caused by energy dissipation i.e. damping. To describe damping it is usual to assess the energy that is lost during one load cycle. This is equal to the area enclosed by the hysteresis loop. Energy loss is then usually normalized by the elastic stored energy, for a detailed description see (Ishihara, 1996). Similarly to stiffness, damping is also depending on strain level, but an opposite tendency can be observed, namely damping increases with strain amplitude. This tendency is usually captured by the damping curve.

Several complex soil models have been developed to capture the nonlinear cyclic behavior of soils. In general, these models define a stiffness degradation curve and a damping curve, and they can only produce accurate results, if sophisticated laboratory and field test are used to determine their key model parameters. (Kramer, 1995) categorized the models into three classes:

- equivalent linear model
- cyclic nonlinear models
- advanced constitutive models

Of these the first is the simplest but most frequently used in geotechnical earthquake engineering for ground response analysis, although it is not capable to model the actual path of the hysteresis loop. The last class contains complex material models which are used in finite element software and can describe several important aspects of soil behavior (e.g. initial stress conditions, different stress paths, rotating principal stresses, cyclic loading, different strain rates, and undrained condition). Due to this they usually require many model parameters and their careful calibration. Models in the middle class focus on the description of hysteretic behavior and strain dependent modulus and damping. In the following the equivalent linear and a cyclic nonlinear model, the Ramberg-Osgood model are presented. The practical formulation of the Ramberg-Osgood model is shown detailed, because it will be used later in this study.

2.1.2 Equivalent linear model

This model uses a linear calculation approach and iteration to account for the strain dependent stiffness. For very small shear strains soils usually respond according to linear elastic behavior.

As discussed in (Kramer, 1995) based on Hooke's law, it is possible to relate the elastic properties of soils and the wave propagation velocities:

$$v_p = \sqrt{\frac{G(2-2\nu)}{\rho(1-2\nu)}} \quad \text{Equation 2-5}$$

where v_p is p-wave velocity, G is shear modulus, ν is Poisson ratio, ρ is density.

$$v_s = \sqrt{\frac{G}{\rho}} \quad \text{Equation 2-6}$$

where v_s is s-wave velocity.

In these equations from a practical point of view, since induced strains are usually very small, G can be considered to be G_{max} . However, at larger strains, elasticity is no longer valid. To distinguish the strain range of these two behaviors the concept of linear cyclic threshold strain was introduced in (Vucetic, 1994). If the induced shear strains are larger than the threshold strain, a cyclic loading pattern will result in a hysteretic stress-strain response, as shown in Figure 2-7. The description of the behavior is detailed more in Figure 2-8, which introduces two shear moduli.

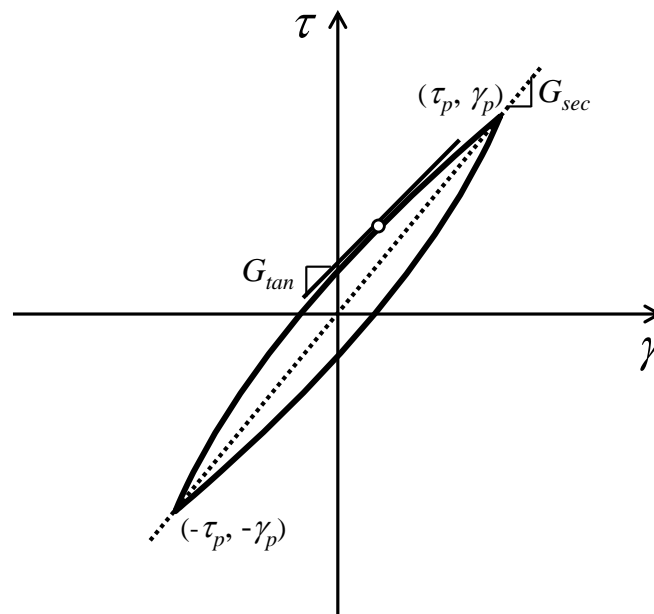


Figure 2-8 Secant shear modulus and tangent shear modulus

In each point of the loop a tangent can be obtained, the slope of which defines the actual shear stiffness, usually called tangent shear stiffness G_{tan} . For describing one full cycle the stiffness can be defined as the secant shear stiffness G_{sec} which can be considered the average stiffness during the whole cycle:

$$G_{sec} = \frac{\tau_p}{\gamma_p} \quad \text{Equation 2-7}$$

where τ_p and γ_p are shear stress and shear strain at the peak respectively. This model only uses the G_{sec} modulus to calculate the total shear strain induced by a given shear stress and therefore it is not capable of modeling each point of the cycle. Instead of modeling the whole nonlinear cycle, the ‘‘average’’ of the response is obtained by a linear calculation, hence the name equivalent linear model. While this is an approximation, this model can still produce acceptable results e.g. in ground response analysis with considerably faster calculation time.

The breadth of the hysteresis loop or more precisely the area within the loop is connected to the energy dissipation during that loop and it can be quantified by the damping ratio D :

$$D = \frac{W_D}{4\pi W_S} = \frac{1}{4\pi} \frac{A_{loop}}{\frac{\tau_p \gamma_p}{2}} = \frac{1}{2\pi} \frac{A_{loop}}{G_{sec} \gamma_p^2} \quad \text{Equation 2-8}$$

where W_D is the dissipated energy, W_S is the maximum strain energy of the equivalent elastic material, and A_{loop} is the area of the hysteresis loop.

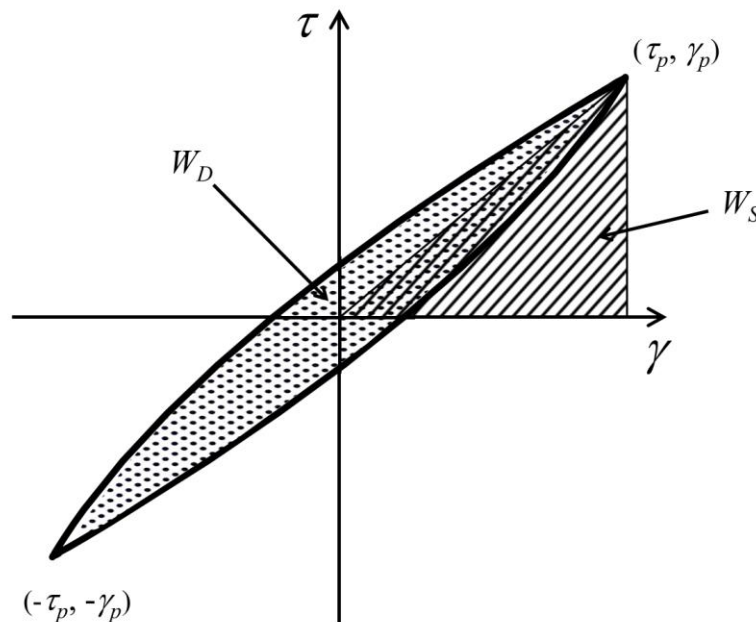


Figure 2-9 Hysteresis loop of one cycle showing dissipated energy W_D , and equivalent elastic strain energy W_S

Energy dissipation occurs mainly due to friction between particles and as a consequence due to heat emission. If the loading is repeated with different amplitudes, different hysteresis loops can be obtained, see Figure 2-10. Two observations can be made. The larger the induced strain, the more inclined to loop gets; hence the secant modulus gets smaller with increasing

strain. This is how the stiffness degradation shown in Figure 2-3 can be observed in a test. Second, the larger the strain, the wider the loop gets; therefore, damping gets larger with increasing strain. The stiffness degradation can be characterized by the degradation curve or by the backbone curve, which can be obtained by connecting the peaks of hysteresis loops at increasing strain.

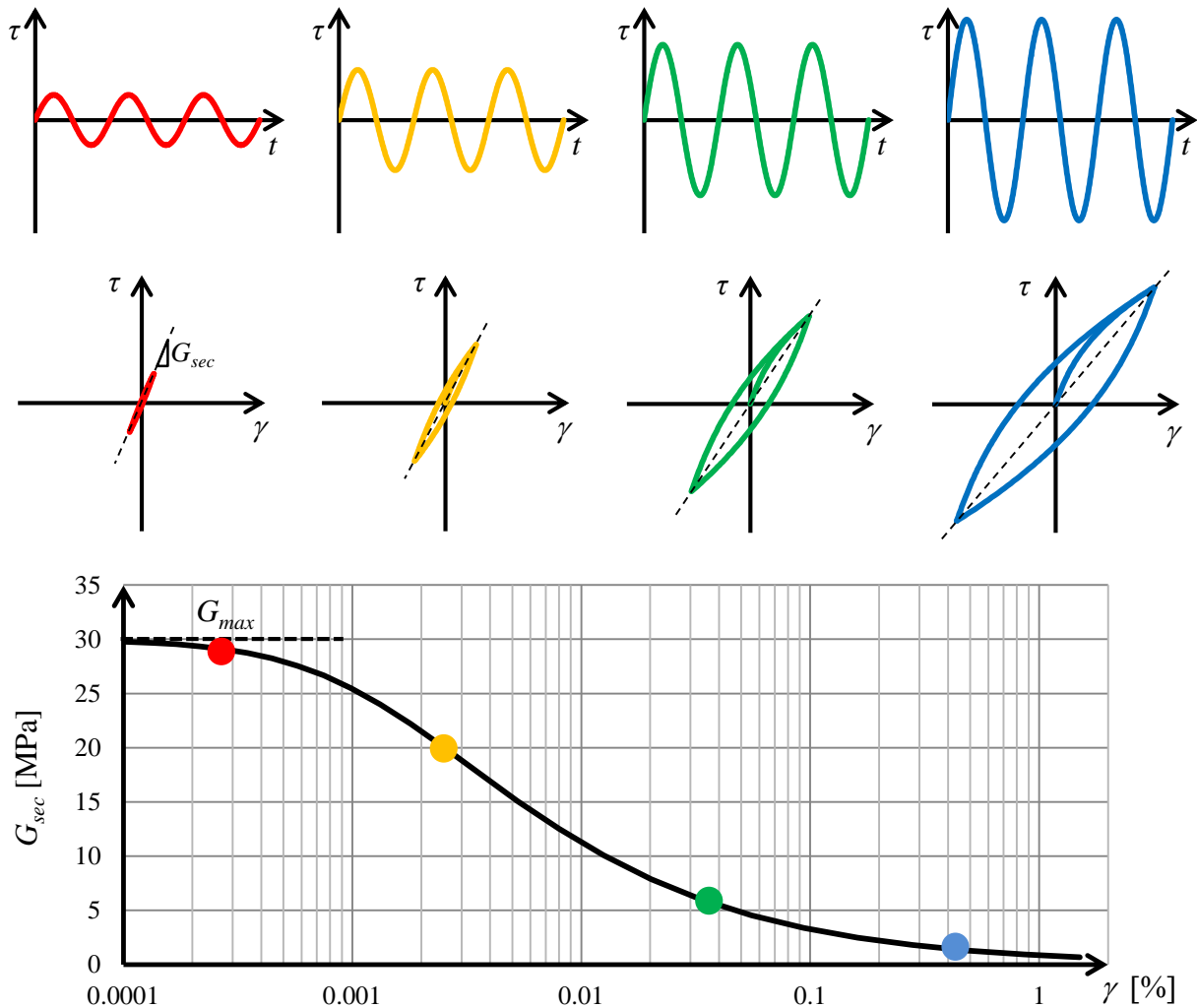


Figure 2-10 Hysteresis loops at different strain levels due to harmonic cyclic loading

When trying to describe the nonlinear cyclic behavior of soil with a material model, it is clear that a linear model is not suitable for precise calculations. However, if a stiffness degradation curve is defined in the model, an iterative approximate solution can be developed which produces acceptable results. Initially the soils are assigned a stiffness of G_{max} . Following each round of computations, shear strain histories are tabulated for every element. Based on those histories, new reduced G values are assigned to each element. The response is recalculated and the new strain histories are compared to the previous ones. If the difference between them is

less than a prescribed error value, the analysis is finished. If not, a new stiffness is determined and response is calculated again. This method usually converges after 4 or 5 iterations.

Since linearization is just an approximation of real soil behavior, there are drawbacks. The reduced modulus is applied for the entire duration of shaking, giving a very poor simulation of high frequency response and allowing soft layers to absorb too much energy. No permanent deformations can be calculated with this model, after unloading the strain will always return to zero. It is also important to note, that failure cannot be modeled with this approach either, because it has no limiting strength.

2.1.3 Modeling irreversible small strain behavior

A simplified approach for considering irreversible strains which are often used for extending the nonlinear small strain models is the deformational plasticity (Puzrin, 2012). For this the so called Masing rules have to be introduced which were first published in (Masing, 1926) to describe the behavior of brass under cyclic loading and have been since adopted to soils and extended as well (Pyke, 1979). In (Benz, 2006) the following comprehensive summary is given about them:

1. The shear modulus in unloading is equal to the initial tangent modulus for the initial loading curve.
2. The shape of the unloading and reloading curve is equal to the initial loading curve, except that its scale is enlarged by a factor of two in both directions.

The first two rules are sufficient to describe regular, symmetric cyclic loading. If the loading is more general or irregular, meaning not symmetrical or periodic, the following two additional rules are commonly added to the two original Masing rules:

3. Unloading and reloading curves should follow the initial curve in case the previous maximum shear strain is exceeded.
4. If the current loading or unloading curve intersects a previous one, it should follow the previous curve.

The four rules together are known in literature as the extended Masing rules. Figure 2-11 shows hysteresis loops in symmetric and irregular loading that comply with these four rules. It should be noted that Rule 4 has been a topic of discussion in literature, see (Benz, 2006). Figure 2-11 (b) shows three possible paths (A, B and C) the curve could follow after unloading and reloading within a previous larger loop.

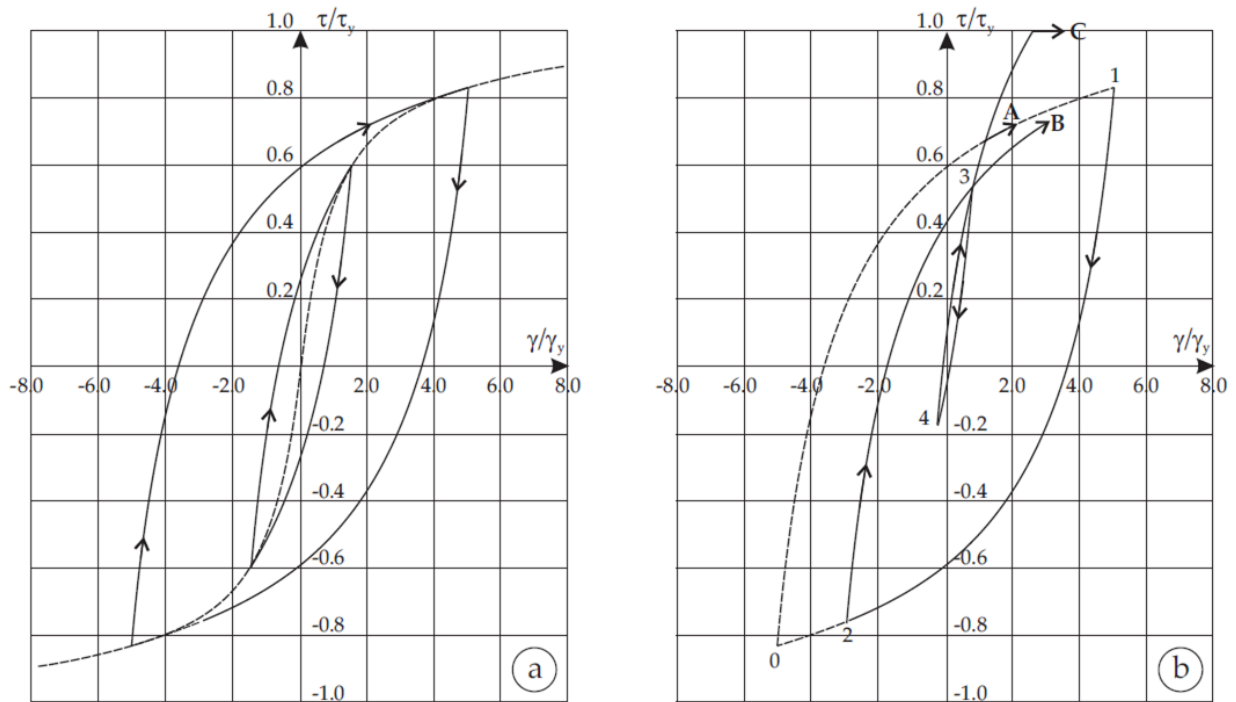


Figure 2-11 Hysteresis loops in symmetric (a) and irregular loading (b) according to the extended Masing rules (redrawn from (Benz, 2006), after (Pyke, 1979))

2.1.4 Modified Ramberg-Osgood model

The Ramberg-Osgood model originally was introduced in (Ramberg & Osgood, 1943). The proposed model used three parameters for describing stress-strain curves of aluminum-alloy and steel sheets. Later in (Idriss, Dobry, & Singh, 1978) an adaptation of the model was proposed in order to obtain the shear modulus reduction. Since then it was used in several studies to model small strain soil behavior, e.g. (Ray & Woods, 1988).

In general form, the proposed function for the normalized stress-strain relationship introduced in Figure 2-6 and its first derivative are:

$$x = y + \alpha y^R \quad \text{and} \quad \frac{dy}{dx} = \frac{1}{1 + \alpha R y^{R-1}} \quad \text{Equation 2-9}$$

where parameters

$$\alpha = x_L - 1 \quad \text{and} \quad R = \frac{1-b}{(x_L-1)b} \quad \text{Equation 2-10}$$

are chosen to fit curves obtained by laboratory measurements.

The derived formulation to be used in practical calculations is detailed in the following. Shear stress-strain relation is described by a hyperbola:

$$\gamma = \frac{\tau}{G_{max}} \left(1 + \alpha \left| \frac{\tau}{C \tau_{max}} \right|^{R-1} \right) \quad \text{Equation 2-11}$$

where γ and τ are shear strain and stress, G_{max} is the small strain shear modulus, τ_{max} is maximum shear stress, α , C and R are model constants. Note that in this formulation shear stress is normalized by the maximum shear stress which is usually obtained from triaxial test results. The stress-strain formulation is straightforward, although it is very difficult to invert. Figure 2-12 shows typical stress strain curves obtained with the model.

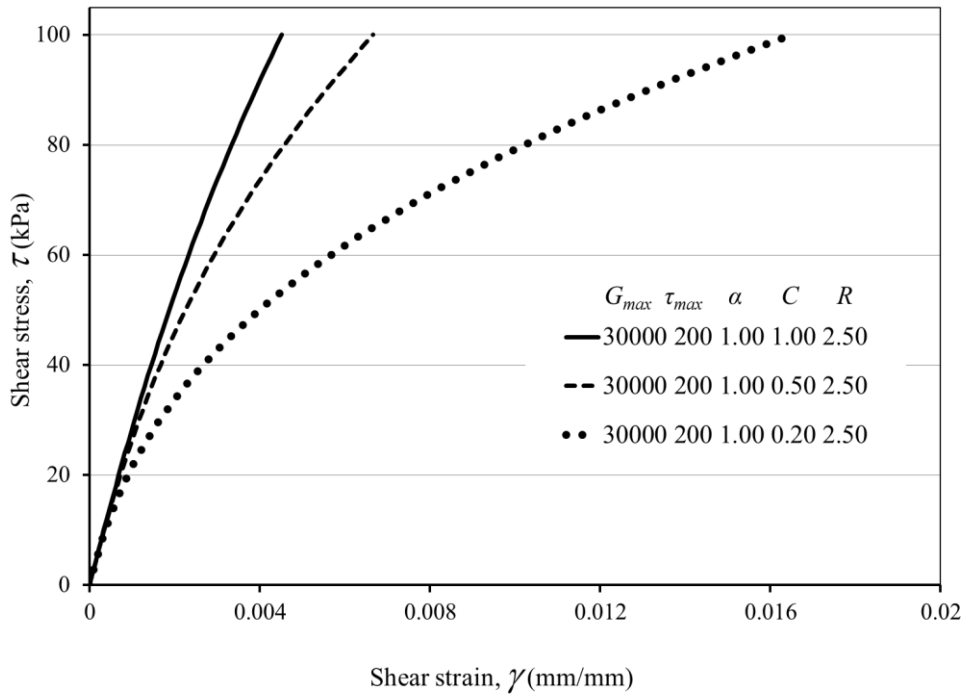


Figure 2-12 Stress-strain curves obtained with the Ramberg-Osgood model

Definitions for secant and tangent modulus follow directly from their definitions such that:

$$G_{sec} = \frac{\tau}{\gamma} = \frac{G}{\left(1 + \alpha \left| \frac{\tau}{C \tau_{max}} \right|^{R-1} \right)} \quad \text{Equation 2-12}$$

and for tangent modulus:

$$G_{tan} = \frac{\partial \tau}{\partial \gamma} = \frac{G}{\left(1 + \alpha R \left| \frac{\tau}{C \tau_{max}} \right|^{R-1} \right)} \quad \text{Equation 2-13}$$

Secant modulus is often used for equivalent linear ground response analysis calculations, while tangent modulus is used in calculations which use time-stepping such as the method of characteristics.

The degradation curve for secant modulus is given by:

$$\frac{G_{sec}}{G_{max}} = \frac{1}{1 + \alpha \left| \frac{\tau}{C \tau_{max}} \right|^{R-1}} \quad \text{Equation 2-14}$$

Plots of normalized secant and tangent modulus vs. strain are given in Figure 2-13. Note that the computation of moduli vs. strain is not a straightforward process, since strain does not appear in the formulation of the degradation curve. However, one may choose a value of τ , and then compute both moduli with Equation 2-12 and Equation 2-13 then compute strain via Equation 2-11. This can easily be done with spreadsheets.

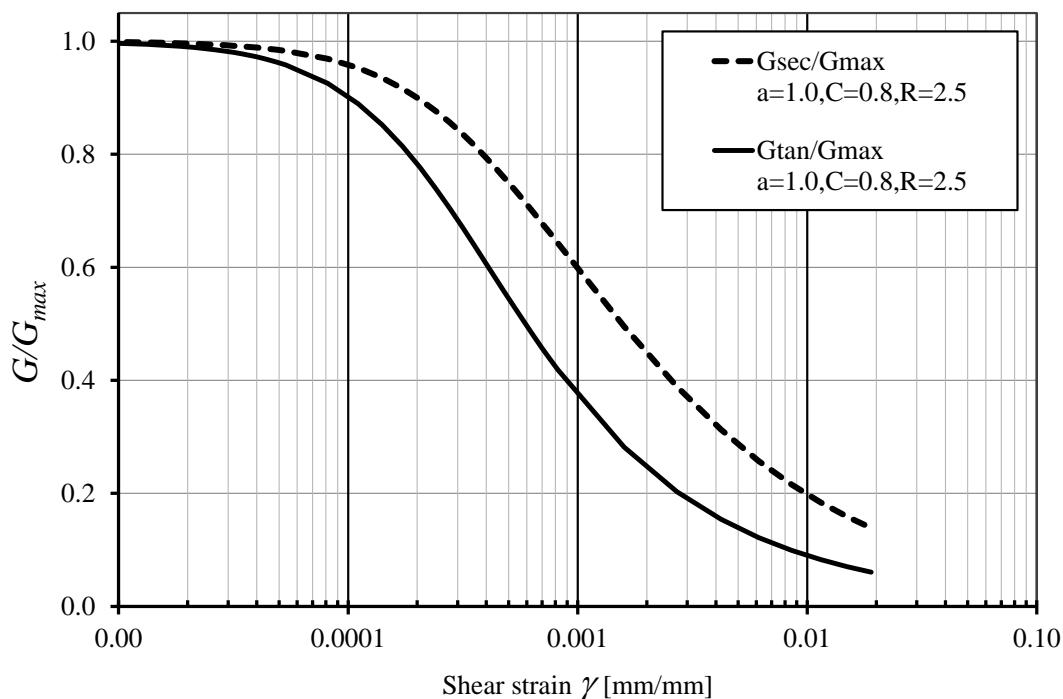


Figure 2-13 Normalized secant and tangent modulus vs. strain obtained with the Ramberg-Osgood model

Some obvious behavior from Figure 2-13 is worth noting. First; strain is plotted on the horizontal axis using a logarithmic scale. This shows typical soil behavior more clearly than a linear scale would and so it is often done in literature. One has to keep in mind that strain is often expressed in percent (%) instead of (mm/mm) and is generally single amplitude, peak value. Some laboratory testing will measure RMS value (0.707x single amplitude) or peak-to-peak (2x single amplitude). Another treatment of strain occurs when equivalent linear models

(e.g. SHAKE, Strata, FLUSH) are used and an effective strain ($\gamma_{eff} = 0.65 \times$ single amplitude) may be used. These are very common blunders in transposing various authors' data from one graph to another. Second; tangent modulus will always be less than secant modulus at any given strain. Third; modulus ratios become significantly less than 1.0 at fairly low strain levels ($\gamma = 0.001$). Finally; soils can behave significantly different from what is shown here. These curves can slide horizontally by an order of magnitude in either direction or change shape.

The dimensionless form allows for comparing test data for the same soil at different confining stresses. These data then can be applied to the entire soil layer while considering the effects of confining stress. The dimensionless form of the formulation follows as:

$$\frac{\gamma}{\gamma_r} = \frac{\tau}{\tau_{max}} \left(1 + \alpha \left| \frac{\tau}{C \tau_{max}} \right|^{R-1} \right) \quad \text{Equation 2-15}$$

where γ_r is reference shear strain at τ_{max} shear stress:

$$\gamma_r = \frac{\tau_{max}}{G} \quad \text{Equation 2-16}$$

Using dimensionless values is not difficult; however, some agreement must be made about the evaluation of τ_{max} for each specific soil layer. A typical assumption is Mohr-Coulomb failure envelope strength with effective stress properties. Such an envelope is shown in Figure 2-14. Based on the diagram the maximum shear strength is:

$$\tau_{max} = \left(\frac{c'}{\tan \phi'} + \sigma'_0 \right) \sin \phi' \cos \phi' \quad \text{Equation 2-17}$$

$$\tau_{max} = \sqrt{\left(\left(\frac{1+K_0}{2} \right) \sigma'_v \sin \phi' + c' \cos \phi' \right)^2 - \left(\left(\frac{1-K_0}{2} \right) \sigma'_v \right)^2} \quad \text{Equation 2-18}$$

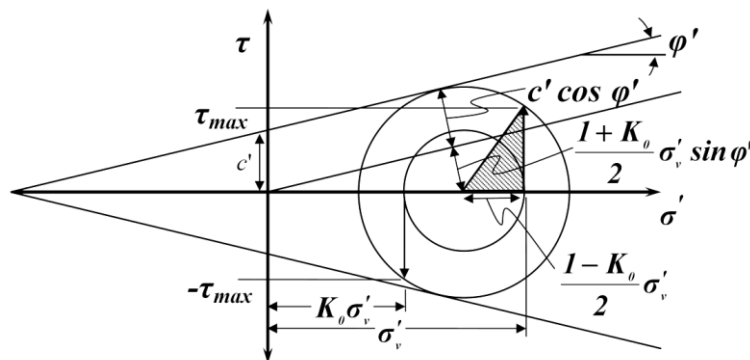


Figure 2-14 Mohr diagram for maximum shear stress

The value of maximum strength will vary with average confining stress σ'_0 . Dimensionless stress-strain curves can be generated in the same manner as the curves in Figure 2-12 by simply substituting values into Equation 2-15. The dimensionless strain values are different than “regular” strain values shown in Figure 2-12 by a factor of about 1000. While this may first seem to be a waste of effort, when viewed from the perspective of laboratory data, it is very valuable since specimens under different confining stress will exhibit different reduction curves. The process of normalizing collapses the curves onto one common curve if they are similar soils. The curves can then be reconstructed for any confining stress or depth of interest, by reversing the process.

The formulation by Midas (MIDAS Information Technology Co., 2014) is slightly different than the one presented above, and it is shown here because this notation is used in Chapter 3.5. The main equation for initial loading is given as:

$$G_0 \gamma = \tau + \alpha |\tau|^\beta \tau \quad \text{Equation 2-19}$$

where G_0 is the small strain stiffness (shear modulus), γ and τ are shear strain and shear stress respectively, α and β are model parameters given by:

$$\alpha = \left(\frac{2}{\gamma_r G_0} \right)^\beta \quad \text{and} \quad \beta = \frac{2\pi h_{max}}{2 - \pi h_{max}} \quad \text{Equation 2-20}$$

where γ_r is the reference shear strain and h_{max} is the maximum damping constant.

For unloading and reloading the hysteresis curve is as follows:

$$G_0 \left(\frac{\gamma \pm \gamma_1}{2} \right) = \left(\frac{\tau \pm \tau_1}{2} \right) \left(1 + \alpha \left(\tau \frac{\tau \pm \tau_1}{2} \right)^\beta \right) \quad \text{Equation 2-21}$$

where γ_1 and τ_1 are the shear strain and stress values at the turnaround point.

2.2 Measurement of dynamic soil properties

The assessment of dynamic soil behavior presents quite a big challenge for geotechnical engineers due to numerous reasons. First of all, the loads to be considered are quite different than the usual loads civil engineers need to consider. To be precise the loading itself is dynamic (or cyclic) and not the soil behavior or soil properties, however since these expressions are widely used in literature, they are used in this study also. Most dynamic problems are connected to some kind of wave propagation (e.g. vibrations of machine foundation, cyclic loading of waves in water or earthquake loading) and it is already difficult to describe and quantify the loading. Secondly, these loads can induce strains ranging from a very low level ($\sim 10^{-4}$ %) to a high level

(~1 %). As shown in Chapter 2.1 the governing soil properties for very low strain problems are stiffness and damping. In some cases of large strains, the failure of soil masses has to be assessed as well; hence the strength has to be determined too.

The behavior of soils subjected to dynamic loads is governed by dynamic soil properties. There are many tests used for determining parameters, which are describing soil behavior. These can be organized into two main types, field tests and laboratory tests. There are advantages and disadvantages to both groups. Field tests are particularly useful, because they are commonly used for examining a bigger section of the subsoil in contrary with laboratory tests, where only a number of smaller samples are studied and their properties are then carefully used to describe a larger part of the subsoil. There are of course exceptions, e.g. pressuremeter testing, where installation and bedding effects can still be significant, because here a relatively small soil surrounding is tested close to the pressuremeter. The main disadvantage of field tests is that can only be used to monitor the soil behavior in the in-situ state, no changes of state, e.g. change of water content, void ratio can be studied. Laboratory tests can naturally be used for such assessments; although for those the effects of sampling and disturbance during sample preparation make the examinations difficult. The disturbance usually appears through the change of the in-situ stress state (air entry, swelling, destructuring). The selection of testing method should be based on considerations of initial stress state, stress history and the anticipated dynamic loading conditions of the specific problem as well as the variability of the ground. If the variability of the ground is much higher in the vertical direction than the horizontal, as in most cases, basic soil testing can be used to identify main layers (profiling) and the determination of stiffness and stiffness degradation can be focused on samples taken from these layers. However, if lateral continuity cannot be established, the priority is to perform in situ tests, which describe the behavior of the larger area (e.g. MASW profiling) or use more regular in situ tests (e.g. CPT) and approximate correlations based on them.

2.2.1 In-situ tests

Field tests can be categorized into groups based on different aspects; whether they are performed on the surface or not, whether they induce low strains or larger strains etc. Seismic geophysical tests are an important group of field tests. They are usually performed by inducing transient or steady state stress waves and the propagation of them are then observed at different locations. These tests are particularly advantageous because they induce similar soil deformations that are induced by the considered dynamic load e.g. earthquake loads or waves generated by machine foundations. In a noisy environment, the induced small deformations can be

difficult to distinguish from other deformations originating from traffic or other man-made vibrations. In such cases a number of measurements are ‘stacked’ i.e. added and then random noise portions of the obtained signal tend to cancel each other while the actual induced waves are magnified. Many traditionally used in-situ soil investigation methods induce large strains in the subsoil (e.g. CPT, SPT, DP, pressuremeter etc.). Although these tests cannot be used directly for determining dynamic soil properties, their results have been correlated to low-strain soil properties by numerous authors, e.g. (Wolf & Ray, 2017), so they can be used for a first estimate. The most commonly used field tests are discussed shortly in the following. A common feature is, that they all are based on the measurement of the shear wave velocity and they can only be used for determining the small strain stiffness G_{max} , so no damping or modulus reduction properties can be obtained with them. The choice of method depends on the geologic profile, the maximum profiling depth, the size of the investigated site and the importance of the structure or facility. In many cases the field investigation is limited to the top 30 m of the soil layers in order to assess the site based on code regulations (e.g. soil classes in Eurocode 8).

Cross hole seismic test

Cross hole testing is performed within two or more PVC-cased vertical boreholes. The contact between casing and soil can significantly affect the measurement; therefore, usually grouting is used to reduce voids outside the casing. The quality of the contact can be checked with sonic logging methods prior to the seismic test. During the test itself the velocity of two types of horizontally travelling seismic waves can be measured; primary compression (P-wave) and secondary shear (S-wave) waves. In one borehole, a wave generator is used as a source at the test depth and in another borehole (or more boreholes) velocity transducers are used as receivers in the same depth. Both source and receiver are usually fixed in position by pneumatic packers pushing them to the casing. Before testing the verticality of the casing is established with inclinometers to obtain the exact distance between source and receiver. Wave propagation velocity is obtained by measuring the travel time and using the travel distance. Data acquisition is usually done by digital systems, evaluation is based on first arrival times or interval arrival times over the measured distance. From the measured velocities in situ maximum shear modulus can be calculated. Soil density is often estimated only from other investigations. Cross hole tomography can also be used instead of regular cross hole testing. In this case, arrays of receivers are used and therefore multiple paths can be recorded for each signal. Then tomographic processing consisting of inversion is performed (McMechan, 1983) and more precise stiffness profiles can be obtained.

Down hole seismic test

In the seismic down hole test a surface source is used to induce shear waves, usually a sledgehammer striking a metal object pushed into the soil and weighted. A receiver is located in a cased borehole that can be moved to different depth to obtain a shear wave velocity profile. The source is usually offset from the top of the borehole in order to avoid vibration energy travelling down the casing; the travel distance has to be determined accordingly. It is beneficial if the receiver consists of two sets of three orthogonally oriented geophones separated by a known distance. This way the travel time can be measured between them and a more precise measurement can be made which corresponds to the actual depth and not to all layers above. For assessing the travel time, either P or S waves can be used. For P waves, usually the first arrival is assessed, while for S waves the peak to peak method is used. Material and radiation damping reduce wave amplitudes and make measurements below 30-60 m unfeasible.

Suspension PS logging

This method is used in an uncased borehole with use of drilling fluid and its main advantage is that it can be used to obtain both P and S wave velocity data down to great depths (several hundred meters). A 6-7 m long probe containing a source and two receivers is lowered down the borehole suspended by a cable. At the specific test depth, the source generates pressure waves in the drilling fluid which are converted to P and S waves at the borehole wall and travel in the surrounding soil towards the receivers where they convert back to pressure waves coming back to the fluid and finally they reach the receivers. To enhance identification of arrival of P and S waves the test is repeated with an impulse of opposite polarity. Disadvantage of the method is, that the induced S waves have a much higher frequency (0,5-2,0 kHz) than those of interest in geotechnical earthquake engineering.

Seismic cone penetration test (SCPT) and seismic flat dilatometer (SDMT)

These tests are very similar to the down hole test except that there is no need for a borehole which makes them faster and cheaper. The SCPT is performed in the same manner as the regular CPT with the addition of usually two geophones or accelerometers located in the CPT tip. The S and P wave velocity is measured at selected intervals (typically 1 to 2 m) by striking a steel or wood beam pressed firmly against the ground and calculated based on the difference in travel time between the consecutive geophones at a given depth. The benefit of the SCPT is that regular CPT data can be used for soil classification, typically based on interpreted Soil Behavior Type, and determining other related parameters such as ground water table, density etc. (Robertson & Cabal, 2014). The SDMT test is also similar to the regular flat dilatometer test

with a down hole like wave velocity measurement extension. Advantage of the SDMT test over the SCPT is, that the penetration of the dilatometer induces somewhat smaller disturbance (compaction) of the soil while the CPT tends to induce large strains while penetration which changes the state of the soil prior to the low strain seismic testing.

Spectral analysis of surface waves (SASW) and multichannel analysis of surface waves (MASW)

Both methods can be performed on the ground surface without boreholes and are based on the ideas behind the seismic refraction test. They both use the dispersive characteristics of surface waves to determine the variation of shear wave velocity with depth. The earlier method, the SASW uses a source (hammer weight or explosive) and two receivers, later researchers developed the method into the MASW which uses a set of receivers (24 or more) deployed along a line at regular intervals. The maximum depth of investigation with the SASW can even be several km, while the MASW is used for more detailed investigation of the top 30-50 m of soils. The maximum reachable depth is depending on site and source conditions and is dictated by the longest wavelength made by the impact source. Greater impact power translates to longer wavelengths and deeper sampling depths. Vertical low-frequency geophones (<4.5Hz) are recommended as receivers. The length of the receiver spread usually limited to 50-100 m and it is directly related to the longest wavelength detected while receiver spacing (distance between receivers) relates to the shortest wavelength detected. The source and receiver spread distance is one of the variables that affect the horizontal resolution of the dispersion curve. For MASW different types of waves are recorded through the multichannel array. The dispersive nature of different types of waves is imaged through wave-field transformation of seismic record by frequency wavenumber or slowness-frequency transform. From the dispersion image, a dispersion curve of the fundamental mode of Rayleigh waves is selected, which is then inverted for a v_s profile.

2.2.2 Laboratory tests

The following laboratory tests can be performed on soil specimens which are obtained from either undisturbed samples or from reconstructed disturbed samples. Undisturbed samples can be produced by borings and sampling devices of high standard. In many cases their use is unfeasible and reconstituted samples have to be used. Naturally, there is a difference in soil fabric, structure, anisotropy etc. between natural and reconstituted specimens; hence there is always an inherent uncertainty in these tests. However, if a careful and thorough testing program is

performed the effect of the differences can be assessed, and test results on reconstituted samples can be used for a wide range of applications.

Resonant column test

The resonant column test is the most commonly used laboratory test for determining the small strain stiffness and damping properties of soils. After a cylindrical soil sample is prepared and consolidated, a cyclic torsional load with very small strain amplitude is applied to the sample by an electromagnetic loading system. The response of the sample is measured by an accelerometer. The frequency of the harmonic load is changed until the maximum strain amplitude response is reached, which corresponds to the fundamental or resonance frequency. The shear modulus can be obtained by assessing the geometry of the specimen and certain characteristics of the device. Some devices use a hollow cylinder, which is beneficial because in such a sample the variation of shear strain and stress in the sample induced by the torsional load is smaller than in a full cylinder. Advantage of the measurement is that the strain amplitude examined with it is in the small strain range (10^{-4} %) and effect of confining pressure, void ratio and time can be investigated. However usually only isotropic stress states can be investigated and pore water pressure is difficult to measure. Since this thesis focuses on resonant column and torsional shear testing the detailed description of the test is given in Chapter 3.

Bender element

Bender elements can be used for determining shear wave velocity of soil samples. This method is often used in combination with a more sophisticated laboratory test, e.g. cyclic or regular triaxial testing, resonant column or oedometer test. The bender element itself consists of small piezoelectric plates (in the cm range), which are attached to the base and top plates used in the test, protruding into both ends of the cylindrical sample. They are capable of inducing a controlled movement when an electrical signal is imposed on them. Usually two plates are used so that P and S waves can also be generated by their coupled movement. Some piezoelectric crystals can also be used as receivers. This means they induce an electrical signal if they undergo a certain deformation. Based on sample size and recorded travel time of the induced seismic waves, shear wave velocity can be obtained. Several wave types are used (single sine, sine sweep etc.) for the test. Data analysis and interpretation can be quite difficult and is still the topic of research, see e.g. (Szilvgyi, Panuska, & Ray, 2018).

Cyclic triaxial test

The regular triaxial device can be supplemented with a loading piston capable of cyclic loading and be used for obtaining dynamic soil properties at high strain levels. In this test, a cylindrical

specimen is tested in a triaxial cell. The specimen is surrounded with a rubber membrane and a top cap with a porous stone is attached to the top of it. The cell is either filled with water or just with air and the pressure in the cell can be regulated while a vertical loading piston is connected to the top cap. This setup allows for simulating axisymmetric stress states and complex stress paths. Drained and undrained tests can also be run. For the cyclic test, usually the deviator stress is changed harmonically with time and pore pressure increase due to the cyclic load is carefully logged. This type of testing is widely used for assessing liquefaction potential. The biggest advantage is the wide range of anisotropic stress states that can be simulated; however, shear stress conditions during seismic wave propagation cannot be modeled.

Cyclic direct simple shear test

This test is capable of simulating shear stresses in a soil sample which are acting during earthquakes much better than the cyclic triaxial test. The most important waves of an earthquake from a geotechnical engineering point of view are vertically propagating, horizontally polarized shear waves (Figure 2-5) which can be simulated in this test. A short cylindrical sample is loaded vertically by a constant normal pressure while a horizontal cyclic loading is also applied. The sample is restrained against lateral expansion by a series of rings, a wired membrane or rigid boundary platens. Since the shear stress is applied at the top and bottom of the specimen this load will induce non-uniformly distributed shear and normal stresses in the sample. Sample height enlarges this effect, therefore short samples are recommended (diameter/height ratio greater than 8:1).

Cyclic torsional shear test

This test also uses cylindrical soil samples enclosed in a rubber membrane. The horizontal cyclic load is applied on top of the specimen in a torsional manner, similarly to the resonant column test. Some devices are capable of imposing a vertical load on the top of the sample also and this allows for testing under anisotropic stress conditions. The test can be used to obtain shear stiffness and damping over a wide range of strain levels. Some devices use hollow cylindrical samples which allow for an almost uniform distribution of shear stress and strain in the sample. This has an advantageous effect on precision but at the same time it makes sample preparation quite difficult.

2.3 Determination of dynamic soil parameters based on correlations

In the following, a literature review is presented for obtaining dynamic soil properties of sands with correlations. These correlations can be used for initial estimates in case there are no field

or laboratory measurement data available or to check the order-of-magnitude of experimental measurements. They were obtained by fitting equations to laboratory test results. They are also often used for normalization of laboratory measurement results, to be able to compare them to other researcher’s findings without the need to perform the tests under the exact same conditions.

2.3.1 Small strain stiffness

The most common correlations for G_{max} include the use of a void ratio function and a confinement stress component. A well-known general equation was introduced by (Hardin & Richart, 1963), (Hardin & Black, 1966) which correlates shear modulus in [MPa] to void ratio and confinement pressure as:

$$G_{max} = A F(e) p'^n \quad \text{Equation 2-22}$$

where A and n are experimentally found coefficients, p' is the mean effective stress in [kPa] and $F(e)$ is the function of void ratio usually taken as:

$$F(e) = \frac{(2.17 - e)^2}{1 + e} \quad \text{Equation 2-23}$$

It should be noted that form of $F(e)$ varies from researcher to researcher and the constant 2.17 can be treated as an additional coefficient a so that:

$$F(e) = \frac{(a - e)^2}{1 + e} \quad \text{Equation 2-24}$$

The dimensionless form of Equation 2-22 is also frequently used with normalized pressure:

$$G_{max} = A F(e) \left(\frac{p'}{p_{atm}} \right)^n \quad \text{Equation 2-25}$$

where the use of atmospheric pressure p_{atm} allows for any convenient units of measure. Equation 2-25 is the most often used correlation for estimating G_{max} and the coefficients A , a and n are also called intrinsic (state-independent) parameters associated with small-strain stiffness (Carraro, Prezzi, & Salgado, 2009).

A summarizing table about many author’s correlations for G_{max} values (in MPa) of cleans sands using Equation 2-25 (with p' in [kPa]) was presented in (Benz, 2006) and is shown in Table 2-1.

From Table 2-1 it is clear that many tests have been made on sands, although most of them are poorly graded clean sands; which means sands without fines and a maximum uniformity coefficient C_U of 2. Researchers early on observed, that the gradation curve of sands have a significant effect on G_{max} . (Iwasaki & Tatsuoka, 1977) stated that shear modulus decreases with increase of uniformity coefficient and also decreases with the increase in the content of fine particles FC ; therefore, the correlations obtained for clean sands usually overestimate G_{max} of sands with a higher C_U and sands with fines content. To account for the effect of fines and higher C_U (Iwasaki & Tatsuoka, 1977) introduced an additional variable B to Equation 2-22 as a multiplier smaller than 1.0, although they did not specify a way to determine its value based on a given C_U and FC . Figure 2-15 shows obtained values for B .

It should be noted that FC in this paper meant mass % of particles smaller than 0.074 mm and not the usual 0.063 mm. Furthermore, the use of the reduction factor B is difficult, because it is not specified, how to obtain B if both C_U and FC has to be accounted for. Reduction values of 60-90% were measured for C_U values of 2-5. A FC of 5% means a reduction of G_{max} to 70% which is significant.

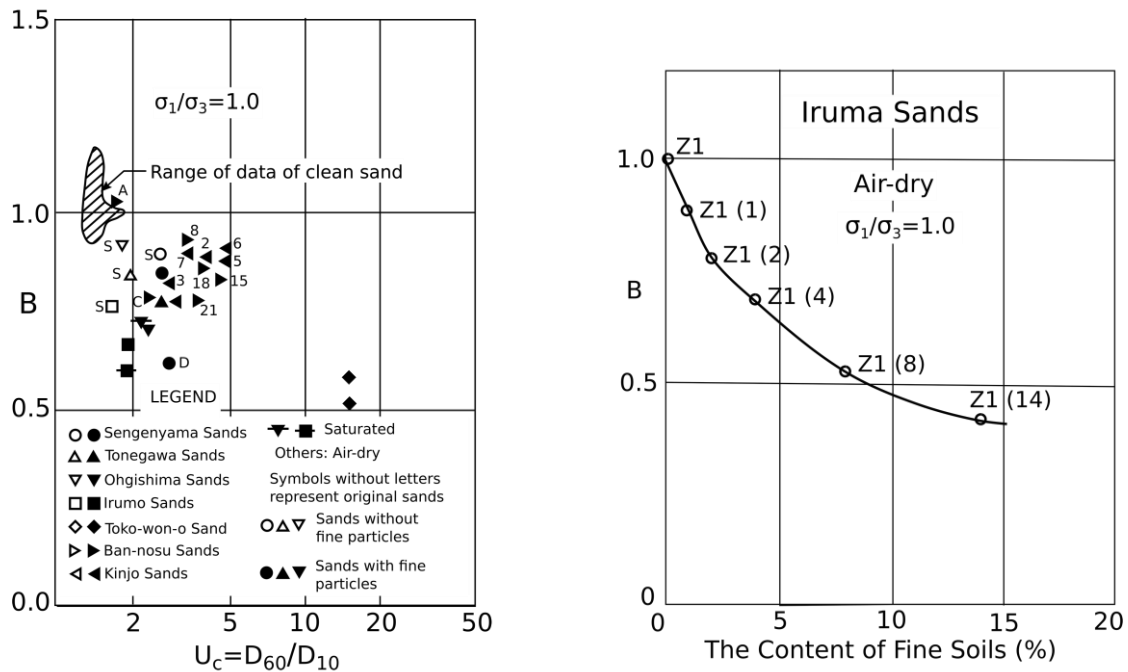


Figure 2-15 Reduction factor B to account for higher C_U and FC obtained by (Iwasaki & Tatsuoka, 1977)

Table 2-1 Correlations for shear modulus G_{max} of clean sands based on (Benz, 2006)(using Equation 2-22 for G_{max} in [MPa] with p' in [kPa])

Soil tested	d_{50} [mm]	C_U [-]	A [-]	$F(e)$ [-]	n [-]	Reference
Kenya carbonate sand	0.13	1.86	101-129	$e^{-0.8}$	0.45-0.52	(Fioravante, 2000)
Toyoura sand (subangular)	0.16	1.46	71-87	$\frac{(2.17-e)^2}{1+e}$	0.41-0.51	(Hoque & Tatsuoka, 2004)
Toyoura sand (subangular)	0.19	1.56	84-104	$\frac{(2.17-e)^2}{1+e}$	0.50-0.57	(Chaudhary, Kuwano, & Hayano, 2004)
Silica sand (subangular)	0.20	1.10	80	$\frac{(2.17-e)^2}{1+e}$	0.5	(Kallioglou, Papadopoulou, & Pitilakis, 2003)
Silica sand (subangular)	0.20	1.70	62	$\frac{(2.17-e)^2}{1+e}$	0.5	(Kallioglou, Papadopoulou, & Pitilakis, 2003)
Silica sand (subangular)	0.20	1.10	62	$\frac{(2.17-e)^2}{1+e}$	0.5	(Kallioglou, Papadopoulou, & Pitilakis, 2003)
Toyoura sand (subangular)	0.22	1.35	72	$e^{-1.3}$	0.45	(Lo Presti, Pallara, Lancellotta, Armandi, & Maniscalco, 1993)
H.River sand (subangular)	0.27	1.67	72-81	$\frac{(2.17-e)^2}{1+e}$	0.50-0.52	(Kuwano & Jardine, 2002)
Glass ballotini (spheres)	0.27	1.28	64-69	$\frac{(2.17-e)^2}{1+e}$	0.55-0.56	(Kuwano & Jardine, 2002)
Hostun sand (angular)	0.31	1.94	80	$\frac{(2.17-e)^2}{1+e}$	0.47	(Hoque & Tatsuoka, 2000)
Silica sand (angular)	0.32	2.80	48	$\frac{(2.17-e)^2}{1+e}$	0.5	(Kallioglou, Papadopoulou, & Pitilakis, 2003)
Ticino sand (subangular)	0.50	1.33	61-64	$\frac{(2.17-e)^2}{1+e}$	0.44-0.53	(Hoque & Tatsuoka, 2004)
Ticino sand (subangular)	0.54	1.50	71	$\frac{(2.27-e)^2}{1+e}$	0.43	(Lo Presti, Pallara, Lancellotta, Armandi, & Maniscalco, 1993)
Silica sand	0.55	1.80	275	$\frac{(2.17-e)^2}{1+e}$	0.42	(Wichtmann & Triantafyllidis, 2004)
Ticino sand (subangular)	0.55	1.66	79-90	$e^{-0.8}$	0.43-0.48	(Fioravante, 2000)
SLB sand (sub-round)	0.62	1.11	82-130	$\frac{(2.17-e)^2}{1+e}$	0.44-0.53	(Hoque & Tatsuoka, 2004)
Ottawa sand No. 20-30	0.72	1.20	69	$\frac{(2.17-e)^2}{1+e}$	0.5	(Hardin & Richart, 1963)
Quiou carbonate sand	0.75	4.40	71	$e^{-1.3}$	0.62	(Lo Presti, Pallara, Lancellotta, Armandi, & Maniscalco, 1993)

Another approach has been presented recently by (Wichtmann, Navarrete Hernandez, & Triantafyllidis, 2015) based on an extensive lab testing program and their earlier correlations given for clean sands in (Wichtmann & Triantafyllidis, 2009). They introduced formulas depending on C_U and FC for the intrinsic parameters a , n and A for sands with non-cohesive fines. They modified Equation 2-22 as:

$$G_{max} = A \frac{(a-e)^2}{(1+e)} p'^n p_{atm}^{1-n} \quad \text{Equation 2-26}$$

$$a = 1.94 \exp(-0.066 C_U) \exp(0.065 FC) \quad \text{Equation 2-27}$$

$$n = 0.40 C_U^{0.18} [1 + 0.116 \ln(1 + FC)] \quad \text{Equation 2-28}$$

$$A = (1563 + 3.13 C_U^{2.98}) 0.5 [\exp(-0.030 FC^{1.10}) + \exp(-0.28 FC^{0.85})] \quad \text{Equation 2-29}$$

These correlations can be used for $FC < 10\%$. For $FC > 10\%$ C_U should be taken as the average inclination of the gradation curve above 0.063 mm and not as the regular d_{60}/d_{10} . It should be noted, that their tested soils were obtained by mixing a natural quartz sand with quartz powder, so the fines investigated were nonplastic. Also, if $FC=0\%$ is substituted into Equations 2-27 to 2-29, they lead back to their correlations given for clean sands in (Wichtmann & Triantafyllidis, 2009).

The effect of plasticity of fines was studied more in detail in (Carraro, Prezzi, & Salgado, 2009). They investigated and compared the behavior of Ottawa sand mixed with plastic and nonplastic fines to clean Ottawa sand. Concerning small strain stiffness, they made several important observations: large reductions were observed in G_{max} for mixtures of sand with nonplastic fines compared to clean sands; however, the addition of plastic fines up to 10% did not result in a change at the same relative density and stress state. This can be explained by micro-mechanical considerations according to the authors. They argued that nonplastic fines usually do not have well-developed contacts with the sand particles and hence do not contribute to shear stiffness, only reduce void ratio. For the range of fines content studied (15%), clayey fines (plastic fines) are more compressible and get entrapped between sand contacts and they reshape themselves during isotropic compression better than silt (nonplastic fines), which leads to a fabric that transmits loads more effectively at very small strains. This shows the importance of the role of soil fabric and structure on the mechanical behavior of soils.

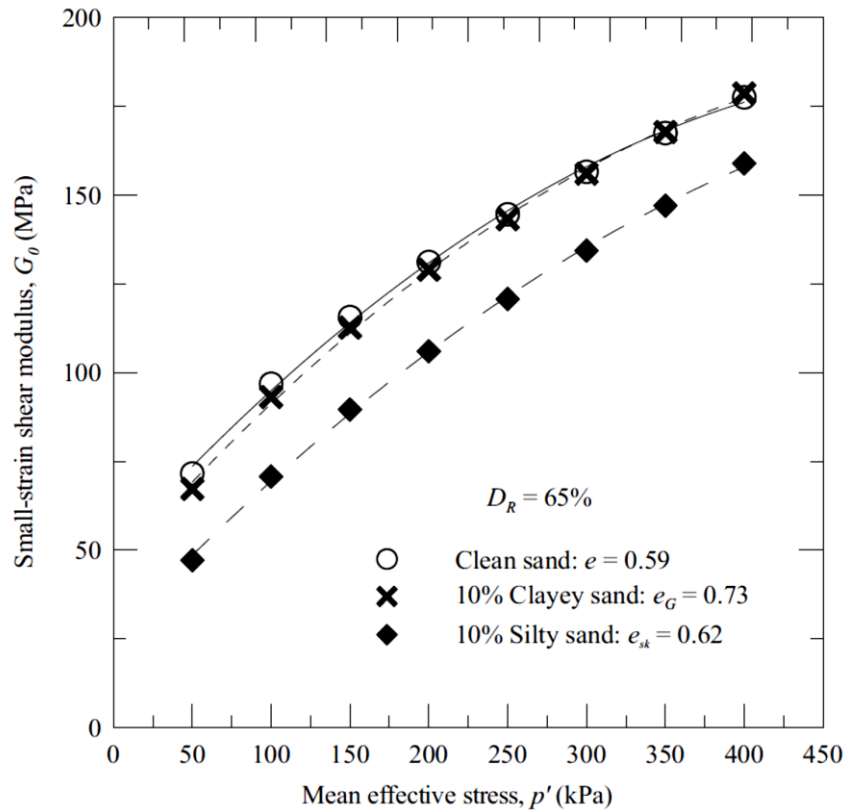


Figure 2-16 Effect of plasticity on the small strain shear modulus of mixtures of Ottawa sand with fines based on (Carraro, Prezzi, & Salgado, 2009). Note: Clayey sand is sand with plastic fines; silty sand is sand with nonplastic fines

Although (Carraro, Prezzi, & Salgado, 2009) did not give a general equation for G_{max} of sands with plastic fines, their results for their Ottawa sand mixed with different % of Kaolin clay (PI=26%) is shown here:

Table 2-2 Obtained intrinsic parameters for Ottawa sand with plastic fines based on (Carraro, Prezzi, & Salgado, 2009)(using Equation 2-22 for G_{max} in MPa with p' in kPa)

FC of Ottawa sand [%]	d_{50} [mm]	C_U [-]	A [-]	$F(e)$ [-]	n [-]
0 (clean)	0.31	1.89	61.1	$\frac{(2.17-e)^2}{1+e}$	0.437
2	-	-	60.2	$\frac{(2.17-e)^2}{1+e}$	0.492
5	-	-	56.9	$\frac{(2.17-e)^2}{1+e}$	0.480
10	-	-	56.0	$\frac{(2.17-e)^2}{1+e}$	0.470

A different void ratio function was suggested by (Biarez & Hicher, 1994) for all soils with liquid limit $w_l < 50\%$, see Table 2-3.

Table 2-3 Correlation for G_{max} of entire soil group given by (Biarez & Hicher, 1994)

Soil tested	e_{min}	e_{max}	A	$F(e)$	n
	[-]	[-]	[-]	[-]	[-]
All soils with $w_l < 50\%$	0.4	1.8	59	$\frac{1}{e}$	0.5

Another correlation is often used because of its simplicity to estimate G_{max} of coarse grained soils which was introduced in (Seed & Idriss, 1970) and used later in (Seed, Wong, Idriss, & Tokimatsu, 1986) (converted here to SI units):

$$G_{max} = 218.8 K_{2,max} p^{0.5} \quad \text{Equation 2-30}$$

with G_{max} and p in [kPa] and a dimensionless coefficient $K_{2,max}$. (Seed, Wong, Idriss, & Tokimatsu, 1986) suggested $K_{2,max}$ values obtained from laboratory tests from 30 for loose sands to about 75 to dense sands (Table 2-4) and values between 80-180 for gravelly soils.

Table 2-4 Estimation of $K_{2,max}$ for sands based on (Seed & Idriss, 1970)

Void ratio e [-]	$K_{2,max}$ [-]	Rel. density D_r	$K_{2,max}$ [-]
		[%]	
0.4	70	30	34
0.5	60	40	40
0.6	51	45	43
0.7	44	60	52
0.8	39	75	59
0.9	34	90	70

Based on resonant column tests on different soils and comparing results of a number of researches (Santos & Correira, 2000) suggested a lower- and upper bound curve for sands and clays which can be used as a check for the order-of-magnitude of the obtained G_{max} value. The curves are defined by:

$$G_{max} = 4000 e^{-1.3} p'^{0.5} \quad \text{Equation 2-31}$$

$$G_{max} = 8000 e^{-1.1} p'^{0.5} \quad \text{Equation 2-32}$$

for the lower-and upper bound respectively.

2.3.2 Modulus reduction

As with G_{max} , the modulus reduction curve can also be estimated with correlations. Equation 2-25 can also be used to model the shear modulus degradation with increasing strain (Jovicic & Coop, 1997). In this approach, coefficients A and n are dependent on shear strain and thus cover a wide range of values. The parameter n is generally 0.5 for very small strains and then increases toward 1.0 for large strains. This approach was used recently by (Oztoprak & Bolton, 2013) who compiled a comprehensive laboratory test database for their state-of-the-art paper with 454 tests gathered from 65 references. The database covers a wide variety of granular soils, such as clean sands, gravels, sands with fines and/or gravels and gravels with sand and fines, altogether 60 different soils. Based on this they developed new correlations for strain dependent shear modulus and normalized degradation curves. They modified Equation 2-25 and suggested a different void ratio function for the strain dependent stiffness:

$$G(\gamma) = \frac{A(\gamma)p_{atm}}{(1+e)^3} \left(\frac{p'}{p_{atm}} \right)^{n(\gamma)} \quad \text{Equation 2-33}$$

where $A(\gamma)$ and $n(\gamma)$ are strain dependent parameters, given by Table 2-5.

Table 2-5 Coefficients for Equation 2-33 in (Oztoprak & Bolton, 2013)

Shear strain amplitude γ [%]	$A(\gamma)$	$n(\gamma)$
0.0001	5760	0.49
0.001	5520	0.51
0.01	4500	0.53
0.1	1810	0.73
1	370	0.86

Using shear strain amplitude of 0.0001%, Equation 2-33 can be used to estimate G_{max} . An important remark about the correlations given in (Oztoprak & Bolton, 2013) is that the accuracy of the fit was also described in detail by the authors: Equation 2-33 with the suggested constants for G_{max} will provide estimates within a factor of 1.6 for one standard deviation of random error (determined from 379 tests). This fairly large scatter suggests that it is extremely difficult to

give a general correlation for G_{max} which would be reliable for such a wide variety of granular soils.

Another approach to account for shear strain effects in laboratory testing, is to normalize secant shear modulus $G_{sec}(\gamma)$ as a function of shear strain by first dividing it by G_{max} . If not stated otherwise, the modulus G is G_{sec} in these normalized relationships. Then shear strain is normalized by dividing it by a reference shear strain γ_{ref} . Reference shear strain has an effect similar to the confining stress correction. It may be obtained by two approaches:

$$\gamma_{ref} = \gamma_{G/G_{max}=Ratio} \quad \text{or} \quad \gamma_{ref} = \frac{\tau_{max}}{G_{max}} \quad \text{Equation 2-34}$$

where *Ratio* is some ratio less than 1.0, usually 0.7 or 0.5. This means the reference strain is taken as a point of the degradation curve; corresponding to 70 or 50% degradation. This approach is used e.g. in the formulation of the Hardening Soil Small material model (Benz, 2006) with 70% and in (Oztoprak & Bolton, 2013) with 50%. In the second approach, τ_{max} is the measured shear strength of the soil at a confining stress equal to that used in the test aiming at measuring dynamic soil parameters. In this study the second approach was used. These normalizations are beneficial and frequently used by researchers because measured degradation curves can be more easily compared to each other this way.

One of the earliest set of modulus degradation curves was published by (Seed & Idriss, 1970) to be used in ground response analysis. They obtained them from 75 tests on a total of 30 sands with a wide range of confinement pressure and void ratio. Together with the curves of (Vucetic & Dobry, 1991) these are still frequently used because computer software such as FLUSH (Lysmer, Udaka, Tsai, & Seed, 1975) and STRATA (Kottke, Wang, & Rathje, 2013) offer them and they are easy to apply. The curves of (Vucetic & Dobry, 1991) were based on a number of cyclic loading tests for a wide range of soils and the main focus was on the effect of plasticity and over-consolidation, however the authors suggested a curve for coarse grained soils ($PI=0$ curve) too. Both curves for sand are presented in Figure 2-17 and the original set of curves by (Vucetic & Dobry, 1991) is given in Figure 2-18. While for clays the over-consolidation ratio OCR has a significant effect on the shear modulus, for sands this is not the case and the influence of OCR on G_{max} is negligible (Jamiolkowski, Lancellotta, & Lo Presti, 1995).

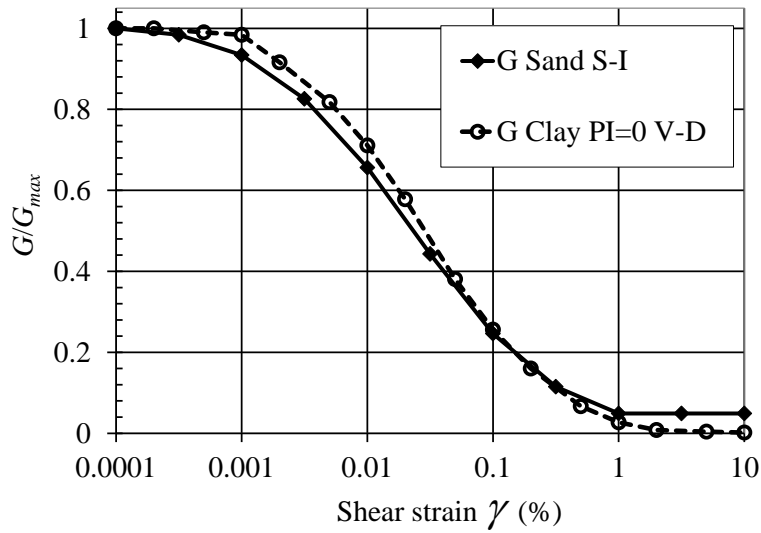


Figure 2-17 Modulus reduction curves for sand by (Seed & Idriss, 1970) and (Vucetic & Dobry, 1991)

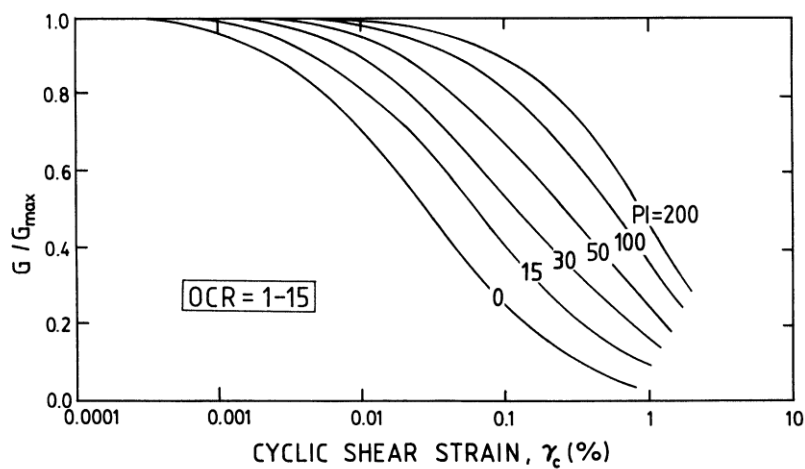


Figure 2-18 Modulus degradation curves for clays and sand ($PI=0$) by (Vucetic & Dobry, 1991)

Many authors also focus on the effect of cyclic degradation of stiffness; the decrease of stiffness with cycle number can be seen in Figure 2-19. The higher number of cycles, the lower G/G_{max} value can be observed. This is due to contact deterioration, which decreases inter-particle friction.

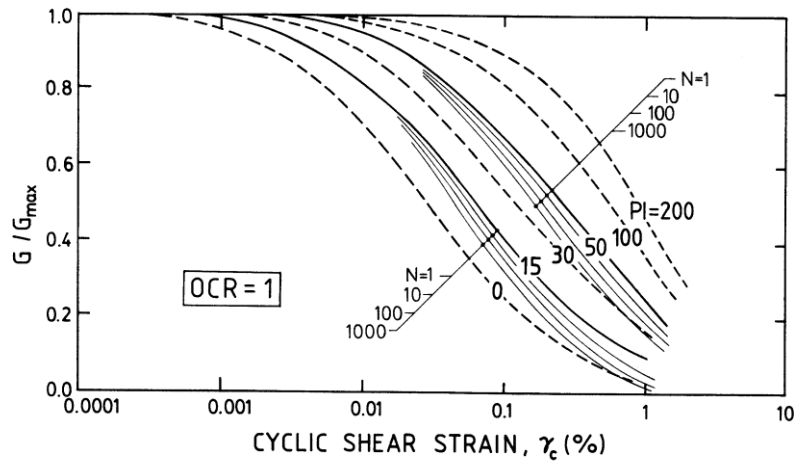


Figure 2-19 Effect of cyclic stiffness degradation on modulus reduction curves of clays and sand ($PI=0$) by (Vucetic & Dobry, 1991)

While these degradation curves are useful, since they were not given with a formulation, just as a set of numbers, their use is somewhat difficult, a more comprehensive mathematical description allows for better modeling. For this, the most commonly used formula is the hyperbolic law for the normalized degradation curve, first proposed by (Hardin & Drnevich, 1972):

$$\frac{G}{G_{max}} = \frac{1}{1 + \left| \frac{\gamma}{\gamma_{ref}} \right|} \quad \text{Equation 2-35}$$

In this approach, γ_{ref} is taken as τ_{max}/G_{max} . While the formulation was clear, the authors observed, that this true hyperbolic relationship did not generally fit their data, so they introduced a modification to the strain scale by using ‘hyperbolic shear strain’ which replaced γ/γ_{ref} on the horizontal axis. For similar reasons, later (Darendeli, 2001) suggested a modified hyperbolic model based on testing of intact sand and gravel samples:

$$\frac{G}{G_{max}} = \frac{1}{1 + \left(\frac{\gamma}{\gamma_{ref}} \right)^a} \quad \text{Equation 2-36}$$

where exponent a is called curvature coefficient. It should not be confused with the coefficient in the void ratio function in Equation 2-24 or Equations 2-26 and 2-27. Here γ_{ref} is the shear strain amplitude where the shear modulus reduces to 50%. To account for pressure dependence, γ_{ref} can be calculated as:

$$\gamma_{ref} = \gamma_{ref_1} \left(\frac{p'}{p_{atm}} \right)^k \quad \text{Equation 2-37}$$

where γ_{ref_1} is the reference shear strain at $p' = p_{atm} = 100$ kPa with an exponent k . In their detailed study on the effect of the uniformity coefficient on G/G_{max} , (Wichtmann & Triantafyllidis, 2013) suggested to use $a=1.03$, $k=0.4$ and

$$\gamma_{ref_1} = 6.52 \cdot 10^{-4} \exp[-0.59 \ln(C_U)] \quad \text{Equation 2-38}$$

A similar formulation for the degradation curve was also used by (Oztoprak & Bolton, 2013). They formulated their fit as a modified hyperbolic equation and provided mean, upper- and lower bound curves based on the gathered vast quantity of earlier test data:

$$\frac{G}{G_{max}} = \frac{1}{1 + \left(\frac{\gamma - \gamma_e}{\gamma_{ref}} \right)^a} \quad \text{Equation 2-39}$$

with the constants as

- $\gamma_e = 0\%$; $\gamma_{ref} = 0.02\%$; $a = 0.88$ for the lower bound,
- $\gamma_e = 0.0007\%$; $\gamma_{ref} = 0.044\%$; $a = 0.88$ for the mean,
- $\gamma_e = 0.003\%$; $\gamma_{ref} = 0.1\%$; $a = 0.88$ for the upper bound,

where γ_e is the elastic threshold strain, beyond which the modulus drops below its maximum; the reference shear strain γ_{ref} is once again the strain at which $G/G_{max}=0.5$; and a is the curvature parameter. The additional strain parameter γ_e allows covering effects of cementation and interlocking effects at small strains. Figure 2-20 shows the degradations curves and the constants with slightly different notation.

If there is no further data available, the authors suggested calculating the elastic threshold strain and the reference strain for the most common confining stresses (70 kPa – 600 kPa) as:

$$\gamma_e [\%] = 8 \cdot 10^{-5} \left(\frac{p'}{p_a} \right) + 6 \cdot 10^{-4} \quad \text{Equation 2-40}$$

$$\gamma_{ref} [\%] = 0.008 \left(\frac{p'}{p_a} \right) + 0.032 \quad \text{Equation 2-41}$$

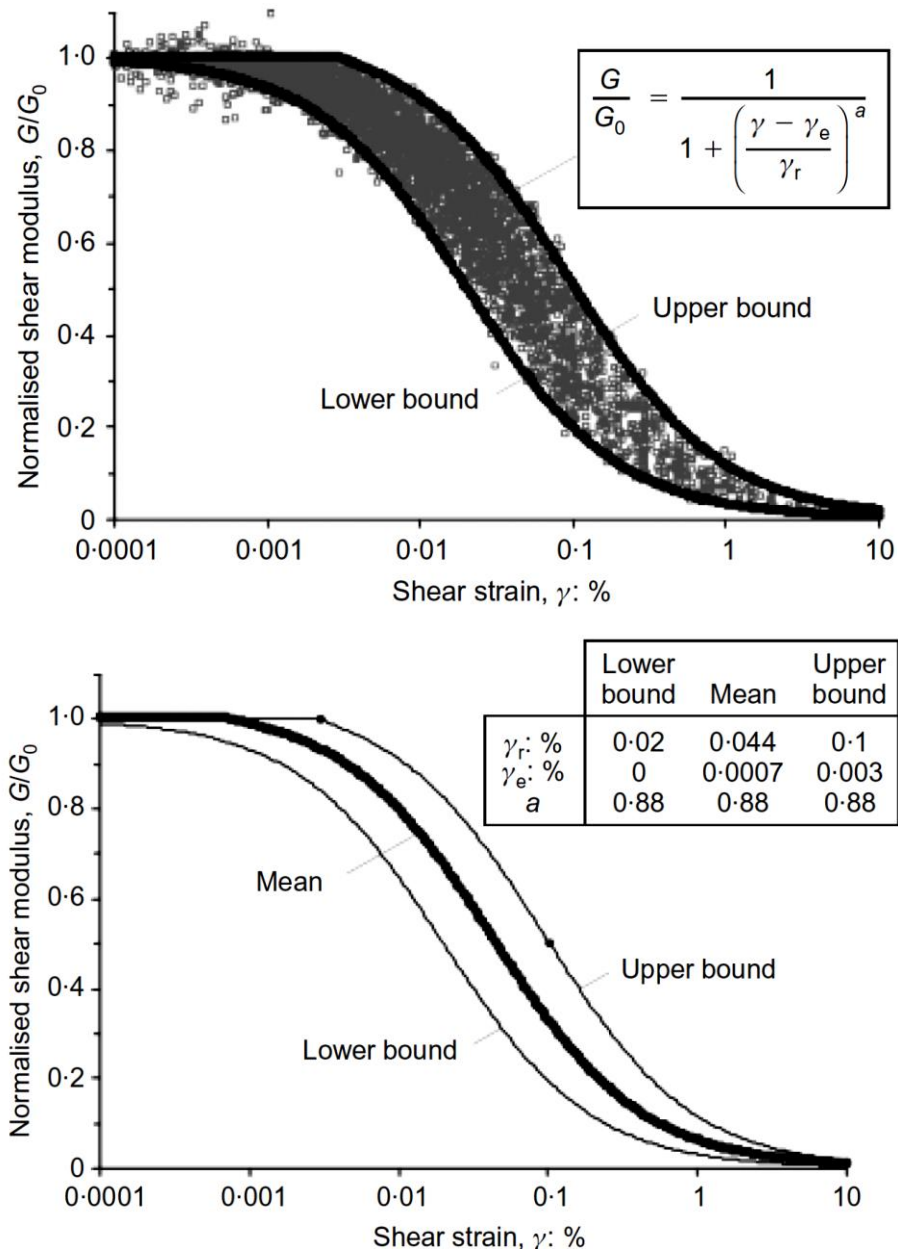


Figure 2-20 Best fit modulus degradation curves for sands by (Oztoprak & Bolton, 2013)

To assess the effects of uniformity coefficient C_U and void ratio e and relative density I_D , the authors performed a multivariable regression analysis and suggested the following, more detailed equations:

$$\gamma_{ref} [\%] = 0.01 C_U^{-0.3} \left(\frac{p'}{p_a} \right) + 0.08 e I_D \tag{Equation 2-42}$$

$$\gamma_e [\%] = 0.0002 + 0.012 \gamma_{ref} \tag{Equation 2-43}$$

$$a = C_U^{-0.075} \tag{Equation 2-44}$$

According to Equation 2-42, an increase in C_U leads to a decrease in γ_{ref} which means a swifter loss of elastic stiffness with strain. (Oztoprak & Bolton, 2013) argued that strain incompatibility between the fine matrix and the larger particles may be behind this effect; because the presence of larger particles causes premature sliding of the smaller ones in contact with them. If their contact is sliding, the small particles no longer contribute to global shear stiffness; hence a greater disparity in grain size reduces γ_{ref} which is also true for γ_e . Another interesting finding is that γ_{ref} correlates to the group e^*I_D rather than e . The authors' discussion stated that e^*I_D may be related to grain shape, since:

- high void ratio for a rounded sand would indicate low relative density, so the product e^*I_D would also be small
- while an angular sand could have a high void ratio at a high relative density and give a large product e^*I_D

The estimates based on Equations 2-37, 2-40 to 2-42 for shear modulus reduction G/G_{max} are accurate within a factor of 1.13 for one standard deviation of random error (from 3860 data points). This suggests that while the estimation of G_{max} with Equation 2-30 is quite unreliable, the degradation curve can be estimated fairly well. As a conclusion, it is suggested to obtain G_{max} either with in-situ or with laboratory measurement methods if possible.

Application of correlations for G_{max} to in-situ soils needs further considerations. It is evident from many laboratory experiments, that it is fairly difficult to reproduce in situ conditions; particularly the effects of aging, moisture conditions and cementation may be the reason behind in-situ small strain stiffness being usually higher than stiffness measured in the laboratory.

Aging causes a continuous increase in G_{max} ; according to observations an approximately linear increase can be observed with the logarithm of time past the end of primary consolidation which cannot be attributed solely to the effects of secondary compression according to (Kramer, 1995). The increase of stiffness with time is usually described by:

$$\Delta G_{max} = N_G (G_{max})_{1000} \quad \text{Equation 2-45}$$

where ΔG_{max} is the increase in G_{max} over one log cycle of time and $(G_{max})_{1000}$ is the stiffness at a time of 1000 minutes after the end of primary consolidation. N_G is a material constant which can be obtained in laboratory measurements. This effect is more pronounced for fine grained soils. According to (Afifi & Richart, 1973) for a soil with d_{50} higher than 0.04 mm, the increase is less than 3% per log cycle of time. (Wichtmann & Triantafyllidis, 2009) reported an N_G value of 0.5% for a quartz sand with $d_{50} = 0.6$ mm.

Moisture conditions can also change soil behavior and the effect of capillary pressure should definitely be considered if the in-situ condition of the layer is unsaturated. Suction will result in an increase in effective stress and this will cause an increase in G_{max} compared to dry and fully saturated soils. An estimated increase in p' can be applied in the correlations to account for this effect. Detailed measurements on capillary effects performed on four sands and a silt are presented in (Wu, Gray, & Richart, 1984), a similar study focused on the small strain stiffness of unsaturated compacted soils presented in (Sawangsuriya, 2006).

Cementation is difficult to account for as undisturbed samples are usually unaffordable and may not be representative for a larger soil mass while cementation is difficult to reproduce on disturbed samples in the laboratory.

2.3.3 Damping

According to theory below the elastic threshold strain γ_e no hysteretic behavior occurs, so soil response is linear and no damping is present. However, experimental evidence shows that some energy is dissipated even at very low strain levels according to (Kramer, 1995). Above the threshold strain, hysteretic behavior and hence damping increases with strain, as shown in Figure 2-7.

Estimating damping with correlations is perhaps a bigger challenge than estimating stiffness, because measurement of damping is more sensitive and difficult. Although the measurement of damping is not as precise as measurement of stiffness, in practical calculations this may not be a big issue, as the effect of damping is minor in most calculations compared to the effect of stiffness. (Hardin & Drnevich, 1972) and (Tatsuoka, Iwasaki, & Takagi, 1978) proposed to express damping ratio as a function of G/G_{max} :

$$D = f\left(\frac{G}{G_{max}}\right) \quad \text{Equation 2-46}$$

Such an approach was suggested by (Ishibashi & Zhang, 1993) who summarized many earlier research and proposed the following equation for sands:

$$D = 0.333 \left\{ 0.586 \left(\frac{G}{G_{max}} \right)^2 - 1.547 \left(\frac{G}{G_{max}} \right) + 1 \right\} \quad \text{Equation 2-47}$$

Later (Zhang, Andrus, & Juang, 2005) published a correlation based on RC and TOSS testing that has also been used by many authors:

$$D = c_1 \left(\frac{G}{G_{max}} \right)^2 + c_2 \left(\frac{G}{G_{max}} \right) - (c_1 + c_2) + D_{min} \quad \text{Equation 2-48}$$

where $c_1 = 0.094$ and $c_2 = -0.265$ for RC; $c_1 = 0.106$ and $c_2 = -0.316$ for TOSS; and D_{min} is the minimum measured damping at very low strains. In their detailed study on the effect of the uniformity coefficient on D , (Wichtmann & Triantafyllidis, 2013) suggested using:

$$c_1 = 0.26 - 0.074 \ln(C_U) \quad \text{and} \quad c_2 = -0.59 + 0.158 \ln(C_U) \quad \text{Equation 2-49}$$

As with G_{max} , the most commonly used correlations for ground response analysis were published by (Seed & Idriss, 1970) and (Vucetic & Dobry, 1991), shown in Figure 2-21.

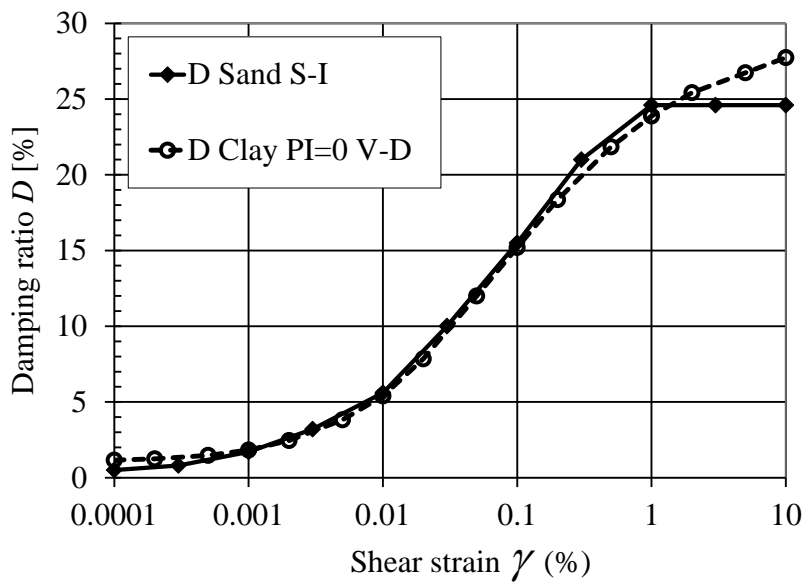


Figure 2-21 Damping curves for sand by (Seed & Idriss, 1970) and (Vucetic & Dobry, 1991)

(Vucetic & Dobry, 1991) provided a set of damping curves in their paper. Here again the effect of OCR and PI was in focus, but the curve obtained for $PI = 0$ is widely used for sands in ground response analysis and one can compare the behavior of sand to fine grained soils easily based on Figure 2-22.

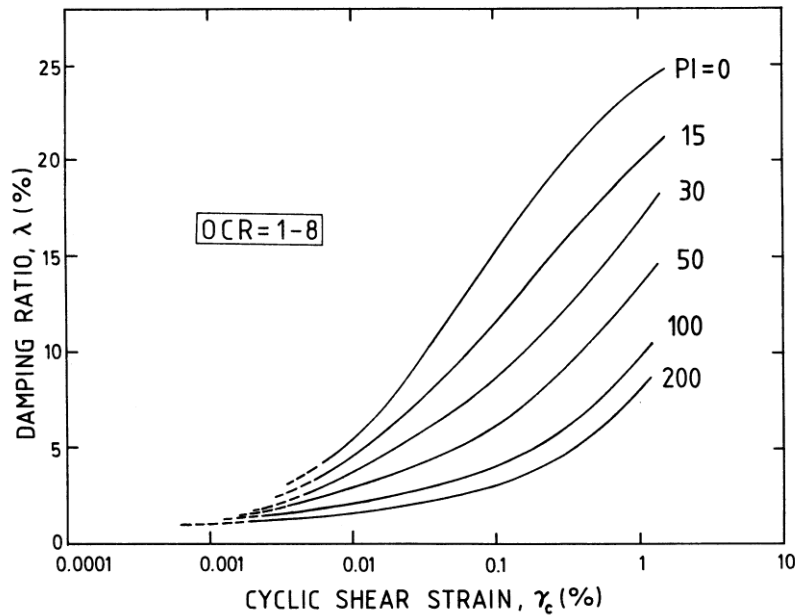


Figure 2-22 Damping curves for clays and sand by (Vucetic & Dobry, 1991)

3 RC-TOSS testing

3.1 Basic testing concepts of RC and TOSS

For the Resonant Column (RC) tests, usually a cylindrical specimen is driven in a harmonic manner back and forth in torsion at very low strain amplitudes with varying frequencies in order to find resonance. Resonance frequency is found when the acceleration response amplitude is reaching a maximum. The governing equation for this problem is based on the theory of wave propagation in rods and can be written as:

$$\frac{I}{I_0} = \frac{\omega_n L}{v_s} \tan \frac{\omega_n L}{v_s} = \beta \tan \beta \quad \text{Equation 3-1}$$

where I is the mass polar moment of inertia of the sample; I_0 is the free end mass polar moment of inertia; ω_n is the resonant frequency in torsion; L is the height of the sample; v_s is the shear wave velocity of the sample and β is the specimen/device constant. All the variables in Equation 3-1 are known, except ω_n and v_s ; so by the measurement of ω_n shear wave velocity can be obtained by:

$$v_s = \frac{\omega_n L}{\beta} \quad \text{Equation 3-2}$$

Small strain shear modulus is then calculated as:

$$G_{max} = \rho v_s^2 \quad \text{Equation 3-3}$$

where ρ is the density of the sample.

The torsional loading is most often achieved with a drive head placed on the top of the sample containing magnets which are surrounded by coils. The coils are driven by a sinewave generator and amplifier while the frequency is varied until resonance is found by observing the peak response from an accelerometer connected to the drive head. Displacement d can be computed by integrating the acceleration twice. For the driving harmonic acceleration, peak displacement d_{peak} is simply related to peak acceleration a_{peak} as:

$$d_{peak} = \frac{a_{peak}}{\omega_n^2} \quad \text{Equation 3-4}$$

Damping can be obtained by the logarithmic decrement method and the half bandwidth method in RC tests. The former one is done by releasing the sample by turning off the excitation at resonant frequency. At higher amplitudes, it is often difficult to get stable readings for the latter method so the log-decrement method generally works better.

The value of damping by the logarithmic decrement method is obtained by:

$$\delta = \frac{1}{N} \ln \left(\frac{z_1}{z_{1+N}} \right) \quad \text{Equation 3-5}$$

$$D = \frac{1}{\sqrt{1 + \left(\frac{2\pi}{\delta} \right)^2}} \approx \frac{\delta}{2\pi} \quad \text{Equation 3-6}$$

where δ is log decrement, N is the number of cycles between two values, z_N is amplitude at cycle N , D is damping ratio. The simplified approximation is accurate to about $D=0.30$.

Torsional Simple Shear Testing (TOSS) involves a similar loading pattern as the RC test, but at much lower frequencies. Rotation is measured using non-contacting proximitors and torque is calibrated from the electrical current level through the coils. Stress and strain can be computed based on sample geometry. Additionally, a vertical LVDT on the center axis of the drive head can be used to measure changes in specimen height during testing. A general loading usually consists of many harmonic loading cycles at certain amplitude to be able to assess the effects of loading cycle numbers and reach a ‘‘steady state’’ hysteresis loop. The test can either be stress controlled or strain controlled. Interpretation of results is based on evaluation of the obtained hysteresis loops in the shear stress-shear strain diagram which is shown in Chapter 3.4.

Comparing RC to TOSS testing the following common features and drawbacks can be highlighted. Benefit of the TOSS testing over RC testing is that non-harmonic, irregular load histories can also be applied to the specimen. Any chosen cyclic loading can be considered irregular history, e.g. an earthquake record or consecutive cyclic loading with gradually changing amplitude. RC testing is usually capable of obtaining shear stiffness and damping at the very small strains ($10^{-4}\%$) and up to intermediate strains ($10^{-2}\%$). Due to measurement precision TOSS testing is not capable to capture the behavior at very small strains but can be used up to larger strains ($10^{-3}\%$ - $10^{-1}\%$) depending on device characteristics. In other words RC is best for the very low strain range and precise measurement of G_{max} , while TOSS can obtain most part of the degradation curve. These two tests are usually performed in separate devices, however in this study a combined device was used which is capable of performing both tests on the same specimen, as shown in Chapter 3.2.

3.2 Device

The combined Resonant Column-Torsional Simple Shear Device (RC-TOSS device) used in this study was originally built by Prof. Richard Ray at Michigan University in the 1980s (Ray R. P., 1983), (Ray & Woods, 1988). For this research, the device has been rebuilt and calibrated in Gyor at the Geotechnical Laboratory of the Department of Structural and Geotechnical Engineering at Szechenyi Istvan University and it is now capable of loading and measuring at higher torques and wider strain ranges. The testing system has been improved with respect to testing range, data storage and manipulation. MS Excel is used for managing testing, VBA macros have been developed for handling TOSS cycle plotting, TOSS and RC data logging as well as comparing and presenting them, see Annex B. Resonant column testing is regulated by the testing standard (ASTM, 2015); however, the scope of the standard does not cover hollow cylindrical testing or combined RC-TOSS testing. Therefore, a detailed testing procedure including device assembly and sample preparation is presented in Chapter 3.3 and in Annex A. Figure 3-1 shows the hollow cylinder sample inside the black membrane with the drive head on top, surrounded by the four drive coils.

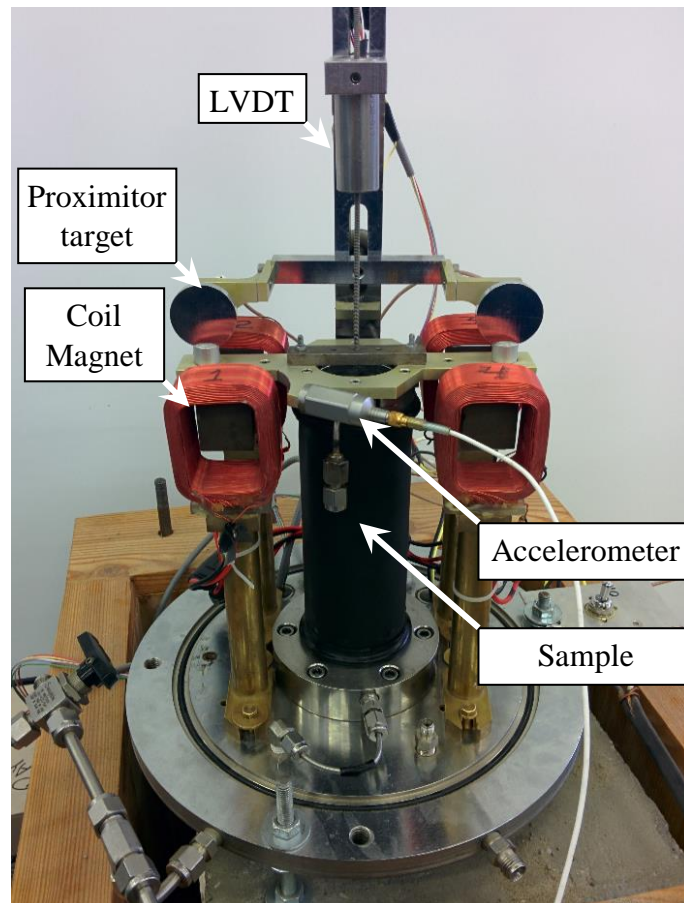


Figure 3-1 Combined Resonant Column – Torsional Shear Device (RC-TOSS) at the Geotechnical Laboratory of Szchenyi Istvn University

The device can drive a cylindrical specimen (inner diameter $D_i = 4.0$ cm, outer diameter $D_o = 6.0$ cm, length $L = 14$ cm) in torsion with the use of permanent magnets and electric coils. The soil specimen is covered by latex membranes inside and out and is fixed at the base and free to rotate at the top, where the drive head is attached, in other words it is a fixed-free configuration. The drive head consists of a coil and magnet system where there is open space between the magnet and coils. The cross-section of the device can be seen in Figure 3-2.

An accelerometer is used for measuring displacement during RC testing; the nature of acceleration measurement allows for very high accuracy at low amplitudes ($\gamma = 10^{-4}$ %). Proximitors measure the gap distance between their targets and are used for measuring rotation (strain) during TOSS tests. Since they are DC output devices, there is no low-frequency roll-off as in accelerometer measurements. A linear variable differential transformer (LVDT) measures vertical displacement of the drive head. Its inner core is connected by a rigid threaded rod to the drive head. The other end of the rod is suspended on a spring, providing a counterforce to the drive head's weight without impeding the RC measurements.

The upper and lower specimen rings have a porous interface and can provide saturation to the specimen. Pore pressures are measured at the confining cell's outer port. Due to the extensive electronics, the confining medium is air.

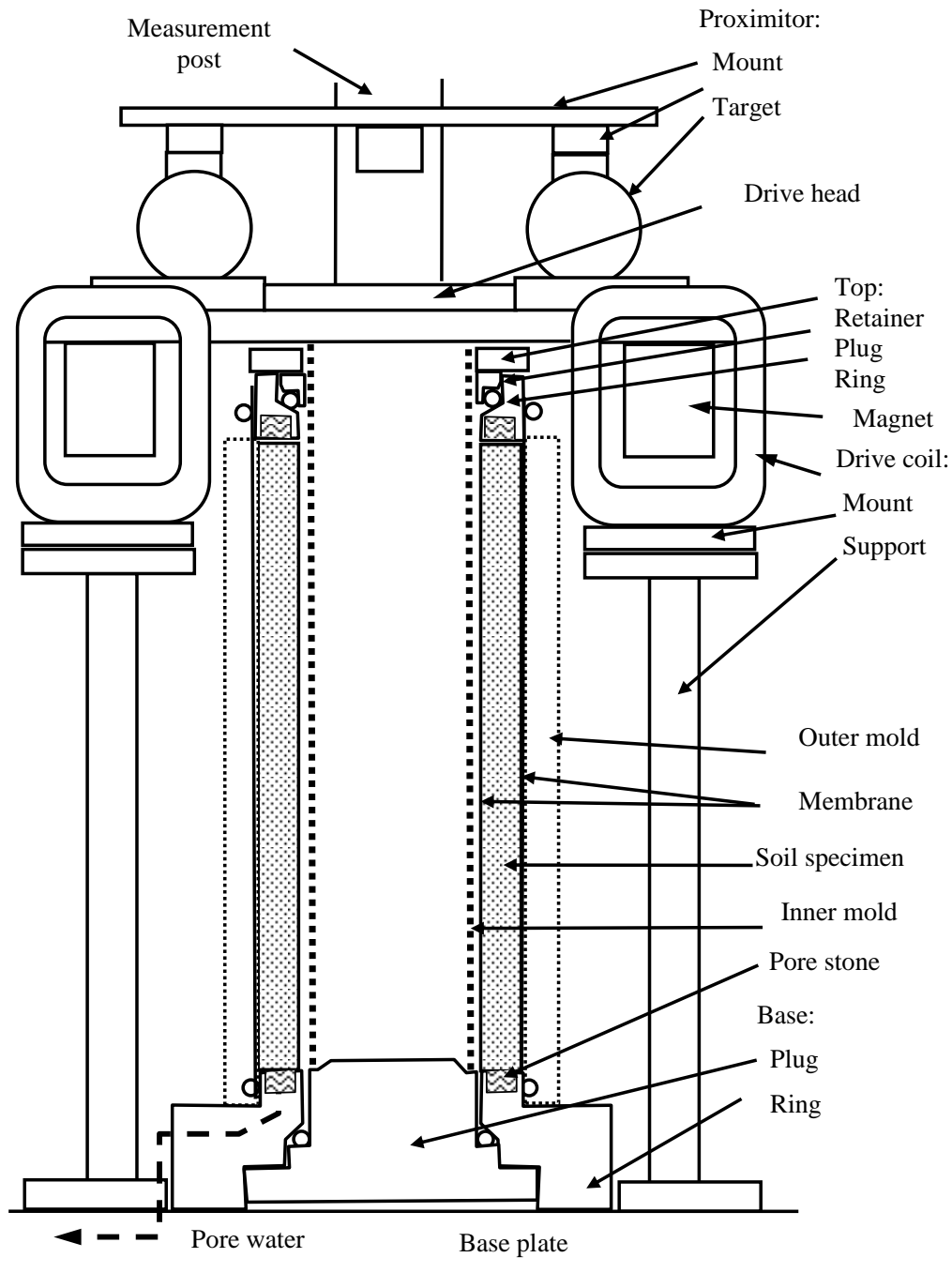


Figure 3-2 Cross section of RC-TOSS testing device

The driving system allows for individual control of the applied shear stresses as well as the cell pressure (with use of a pressure chamber) and the hollow cylindrical specimens have

the great advantage of having nearly-uniform shear stress distribution throughout its cross-section. Calibration methods are described in detail in (Ray R. P., 1983).

For this testing system, typical resonance is around 300 rad/sec which means if the peak acceleration signal is 5mV, acceleration is 0.015 m/sec², displacement is 1.67x10⁻⁷m, and peak strain around 10⁻⁴%.

Obtaining damping with the RC method requires capturing to free decay of the sample after being driven at resonance frequency. By using a cut-off switch that turns the coils into open circuits there is very little coil-generated damping during log decrement measurements. The sample will continue to resonate and response amplitude will be decreasing monotonically due to energy dissipation between particles. The simple open circuit generated no counter-emf damping when tested with a calibration rod, i.e. the rod decayed exactly the same amount, with or without the magnet-coil assembly (with the open switch) in place.

Additionally to the regular RC testing, the drive system can be given an offset DC voltage to apply static stress/strain then resonated with a low-amplitude signal to examine effects of different stress ratios (σ_1/σ_3) and static shear stress/strain ($\tau_{static}, \gamma_{static}$) on shear modulus, however the scope of this study only contained isotropic testing.

For TOSS testing with use of the data acquisition system and computer, various cyclic and arbitrary load histories can be applied. Hysteresis and secant/tangent moduli can then be computed from the acquired data. The unique design of the testing device allows for both RC and TOSS tests to be run on the same specimen any number of times and in any sequence. A particularly useful sequence is to perform low-amplitude RC between different stages of TOSS testing to evaluate the effects of each TOSS stage on the “fundamental” property G_{max} . The baseline value of G_{max} allows data to be normalized by reference strain (γ_{ref}) or other quantities. The drive system uses a 500-watt DC power amplifier that can be current-controlled. Under current (rather than voltage) control, the device can consistently deliver the same stress level during a test, even if the coils heat up. Using neodymium magnets, the device can generate shearing stresses greater than $\tau = 200$ kPa.

3.3 *Sample preparation*

Two sample preparation methods were used in this study for the RC-TOSS test: dry filling with tapping, and pluviation. A loose state was achieved by pouring dry soil into the sample mold with a glass funnel. Since the hollow cylinder specimen had a wall thickness of 1 cm, a funnel with a 14 cm long spout was used. During pouring, the end of the spout was continuously kept

near the surface of the soil and gently moved along, creating a bulking effect. This method is similar to that used to measure the minimum density state. After pouring in the sample, the mold was lightly tapped 10-15 times on its side to achieve a slightly denser state. The dense condition was created by dry pluviation from a height of 50 cm. The soil was carefully poured, so that the thread of soil would be the thinnest achievable. For the tested sands, a separate comparison indicated that dry pluviation and vibration produced nearly identical densities. Table 4-1 shows void ratios achieved by dry filling and dry pluviation methods.

The inner and outer mold held the respective membranes during sample preparation. Once the soil was placed, both membranes were carefully pulled over to the top ring and sealed in position by O-rings. An 80 kPa vacuum confinement was activated inside the sample, the inner and outer molds were removed and the drive system and transducers were assembled. Specimen diameter and height were also measured. A detailed, step-by-step summary about device assembly and sample preparation is given in Annex A.

A typical test started with low amplitude RC measurements after 15 min. confinement. Effect of confinement time was not investigated in detail for this study; only for one sample since granular material under dry conditions do not produce any appreciable duration of confinement effects. For higher confinement stresses a pressure chamber was placed over the testing device and regulated air pressure was applied while keeping the vacuum confinement on. At the next test stage, high amplitude RC and a series of TOSS tests were performed with gradually increasing strain levels. The TOSS tests were stress controlled and each stage consisted of 100 loading cycles. Finally, a low amplitude RC measurement was performed to check if TOSS loading resulted in a change of small strain stiffness.

3.4 Interpretation of measurement results

The measurement with the combined RC-TOSS device is governed with a PC using a data acquisition system and MS Excel with VBA codes. A detailed description of the VBA codes used for running and logging the tests can be found in (Ray R. P., 1983). RC testing is controlled by manipulating the function generator with feedback about acceleration response provided by an oscilloscope. Both tests are logged and recorded into a single macro enabled spreadsheet file (xlsm format) and further data interpretation is used to obtain figures such as shear stress-shear strain curves or modulus reduction curves. Since the combined test could consist of RC and TOSS measurements at several confinement stages with several shear stress amplitudes at each stage with each one containing usually 100 cycles of TOSS loading, the

storage of raw test data usually results in a quite large xlsx file (10-20 MB). This is the reason why data interpretation was chosen to be done in a separate macro enabled spreadsheet file with several macros developed for this study to produce material parameters and graphs.

Data interpretation generally starts with the selection and copying of all performed RC test sequences and the selection and copying of recorded shear stress and shear strain data of TOSS cycles to the prepared spreadsheet used for interpretation. Interpretation of RC measurement data is fairly easy, because measured values of resonance period and acceleration Volts (RMS) are used to calculate shear wave velocity and shear modulus already in the testing spreadsheet; and the logarithmic decrement method is also coded into it, so damping values are readily shown in the testing spreadsheet, see Figure 3-3. TOSS interpretation needs some further considerations. During the TOSS test for each cycle the readings of the DA system are all stored (vertical LVDT reading, pore pressure reading, proximity readings, stress reading and calculated strain). It is important to keep and store these data in case spurious results are found and further analysis is required on the raw data.

After choosing and copying the raw data, several subroutines and functions (HystSegment2, CalcStrainSA, CalcSecantMod, DampSec, see Annex B) developed for this study in VBA are used to obtain measured material parameters. These include the calculation of the area of a hysteresis loop with a numerical integral approach, calculation of single amplitude strain, secant shear modulus and damping based on a set of stress-strain values of a single loop measured during TOSS testing. RC testing data is stored on a separate tab (RCTestSheet); each stress-strain value of a TOSS cycle are placed in the *A* and *B* columns of separate tabs. Then a macro (Grabdamp, see Annex B) is used to gather all calculated material parameters to a summary tab (Results), this is shown in Figure 3-4.

Finally stress-strain curves, modulus reduction curves and damping curves can be generated based on the interpreted data. Typical results of RC testing will be shown in detail in Chapters 4.2 and 4.4.

Typical results of a single TOSS test with 100 cycles are shown in Figure 3-5. Two main effects can be observed. With increasing number of cycles the hysteresis loop gets thinner and the secant of the loop gets steeper. This means that cyclic degradation of damping and cyclic stiffening can be observed for this material. These effects have also been found by (Kramer, 1995) for drained cyclic testing of sands. Note that hysteresis loops of cycles 75 and 100 are exactly on top of each other. This means these two cyclic effects disappear after a number of cycles which was around 75 for this soil.

Date/Datum	Sample/Minta	Inside Dia/ Belso atm. (cm)	Outside Dia/ kulso atm. (cm)	Length/ Magassag (cm)	Sample Volume/ Terfogat (cm ³)	Wet Wt/ Nedves tomeg (g)	Dry Wt./ Szaraz tomeg (g)	Water content/ Vızrtartalom (%)	Wet Unit wt/ Nedves terfogsusı r. (g/cm ³)	Dry Wt/ Szaraz terfogsusır (g/cm ³)	Void ratio/ Hezgateny ezo (-)						
2015.12.02	(34)P2	4.01	5.94	13.82	208.59	394.51	381.58	3.39	1.891	1.829	0.454						
Conf Pres (kPa)	(clock)	hr:min:sec	(msec)	(rad/sec)	(m/sec)	(kPa)	(volts rms)	(cm s-a)	(% s-a)			Z	Z+1	Damping/ Csillap (%)			
84	2015. 11. 30. 17:50	1:35:00	14.76	425.69	243.81	108721	0.00703	1.80E-04	7.04E-04	100%	2.04E-02						
Taumax (kPa)	2015. 11. 30. 17:59	1:44:00	14.77	425.40	243.64	108573	0.00662	1.70E-04	6.64E-04	100%	1.93E-02						
38	2015. 11. 30. 19:20	3:05:00	14.76	425.69	243.81	108721	0.00695	1.78E-04	6.96E-04	100%	2.02E-02						
Gmax (kPa)	2015. 12. 1. 9:05	16:50:00	14.74	426.27	244.14	109016	0.00733	1.87E-04	7.32E-04	100%	2.12E-02						
109016	2015. 12. 1. 9:10	16:55:00	14.96	420.00	240.55	105833	0.02133	5.61E-04	2.19E-03	97%	6.36E-02	30	24	0.71			
Gam Ref (%)	2015. 12. 1. 9:15	17:00:00	15.10	416.10	238.32	103880	0.03690	9.88E-04	3.87E-03	95%	1.12E-01	22	17	0.82			
3.45E-04	2015. 12. 1. 9:20	17:05:00	15.29	410.85	235.31	101274	0.05530	1.52E-03	5.94E-03	93%	1.72E-01	29	18	1.52			
	2015. 12. 1. 9:25	17:10:00	15.38	408.53	233.98	100132	0.06860	1.91E-03	7.46E-03	92%	2.16E-01						
	2015. 12. 1. 9:30	17:15:00	15.85	396.42	227.04	94281	0.08800	2.60E-03	1.02E-02	86%	2.95E-01	22	14	1.55			
	2015. 12. 1. 9:35	17:20:00	15.91	394.92	226.19	93572	0.11570	3.44E-03	1.35E-02	86%	3.90E-01	29	16	1.99			
	2015. 12. 1. 10:42	18:27:00	16.16	388.81	222.69	90699	0.14300	4.39E-03	1.72E-02	83%	4.98E-01	30	15	2.21			
	2015. 12. 1. 10:42	18:27:00	16.71	376.01	215.36	84827	0.17660	5.79E-03	2.27E-02	78%	6.57E-01						
Conf Pres (kPa)	2015. 12. 1. 17:26	25:11:55	12.58	499.46	286.06	149666	0.00510	9.48E-05	3.71E-04	99%	7.82E-03						
160	2015. 12. 1. 17:31	25:16:20	12.53	501.45	287.20	150863	0.00508	9.37E-05	3.67E-04	100%	7.73E-03						
Taumax (kPa)	2015. 12. 1. 18:29	26:14:23	12.54	501.05	286.97	150622	0.00500	9.24E-05	3.61E-04	100%	7.62E-03						
72	2015. 12. 1. 18:31	26:16:23	12.54	501.05	286.97	150622	0.00440	8.13E-05	3.18E-04	100%	6.70E-03						
Gmax (kPa)	2015. 12. 1. 18:29	26:14:23	12.53	501.45	287.20	150863	0.00893	1.65E-04	6.44E-04	100%	1.36E-02						
150863	2015. 12. 1. 18:29	26:14:23	12.55	500.65	286.74	150382	0.01295	2.40E-04	9.37E-04	100%	1.98E-02	35	29	0.60			
Gam Ref (%)	2015. 12. 1. 18:29	26:14:23	12.55	500.57	286.70	150335	0.02390	4.42E-04	1.73E-03	100%	3.65E-02	29	22	0.95			
4.74E-04	2015. 12. 1. 18:29	26:14:23	12.55	500.65	286.74	150382	0.02780	5.14E-04	2.01E-03	100%	4.24E-02						
	2015. 12. 1. 18:29	26:14:23	12.69	495.13	283.58	147083	0.04520	8.55E-04	3.35E-03	97%	7.05E-02	30	23	0.92			
	2015. 12. 1. 18:29	26:14:23	12.80	490.87	281.14	144565	0.06940	1.34E-03	5.23E-03	96%	1.10E-01	16	8	1.10			
	2015. 12. 1. 18:29	26:14:23	12.88	487.82	279.40	142775	0.09760	1.90E-03	7.44E-03	95%	1.57E-01	24	11	1.21			
	2015. 12. 1. 18:29	26:14:23	12.90	487.07	278.96	142333	0.12500	2.44E-03	9.56E-03	94%	2.01E-01	28	14	1.16			
	2015. 12. 1. 18:29	26:14:23	13.12	478.83	274.24	137558	0.17940	3.63E-03	1.42E-02	91%	2.99E-01	22	9	1.42			
	2015. 12. 1. 18:29	26:14:23	13.25	474.20	271.59	134913	0.20440	4.22E-03	1.65E-02	89%	3.48E-01	26	10	1.54			

Figure 3-3 Raw RC testing data in the measurement controlling spreadsheet

TOSS test/TOSS vizsgalat	Strain/Fajlagos alakvaltozas fel amplitudoja (s-a %)	G _{sec} (kPa)	Damping/ Csillapitas (-)	Csillapitas/ Damping (%)	G _{sec} /G _{max} (-)	γ/γ _{ref} (-)	Damping RO (%)	Damping Ishibashi 1993 (%)	Damping Zhang 2005 (%)
(34)P2 @84kPa									
cy1_CyTest 14_5kPa	0.00667	75018	0.04	4.10					
cy100_CyTest 14_5kPa	0.00662	75504	0.01	1.34	0.69	0.19	2.59	6.98	4.91
cy1_CyTest 17_10kPa	0.01296	77194	0.02	1.93					
cy100_CyTest 17_10kPa	0.01288	78157	0.02	1.57	0.72	0.37	4.43	6.40	4.50
cy1_CyTest 19_20kPa	0.02690	74323	0.04	4.15					
cy100_CyTest 19_20kPa	0.02680	74583	0.03	3.25	0.68	0.78	7.14	7.19	5.05
cy1_CyTest 20_30kPa	0.05024	59688	0.11	10.93					
cy100_CyTest 20_30kPa	0.04560	65768	0.06	5.61	0.60	1.32	9.35	9.32	6.50
cy1_CyTest 22_40kPa	0.08495	47142	0.16	15.63					
cy100_CyTest 22_40kPa	0.06981	57226	0.08	8.43	0.52	2.03	11.12	11.64	8.04
cy1_CyTest 23_50kPa	0.14750	33874	0.21	20.92					
cy100_CyTest 23_50kPa	0.10393	48049	0.12	11.68	0.44	3.01	12.71	14.39	9.84
(34)P2 @160kPa									
cy1_CyTest 25_5kPa	0.00366	136598							
cy100_CyTest 25_5kPa	0.00370	134856							
cy1_CyTest 26_10kPa	0.00755	132488	0.01	0.83					
cy100_CyTest 26_10kPa	0.00748	133558	0.01	0.72	0.89	0.16	2.17	2.99	1.93
cy1_CyTest 28_20kPa	0.01536	130108	0.01	1.32					
cy100_CyTest 28_20kPa	0.01542	129483	0.01	1.19	0.86	0.33	3.99	3.46	2.29
cy1_CyTest 30_30kPa	0.02494	120171	0.04	3.75					
cy100_CyTest 30_30kPa	0.02431	123226	0.02	2.25	0.82	0.51	5.53	4.24	2.86
cy1_CyTest 31_40kPa	0.03513	113801	0.05	4.90					
cy100_CyTest 31_40kPa	0.03425	116608	0.03	3.09	0.77	0.72	6.84	5.14	3.51
cy1_CyTest 33_50kPa	0.04624	108045	0.06	5.72					
cy100_CyTest 33_50kPa	0.04535	110089	0.04	3.96	0.73	0.96	7.99	6.10	4.18
cy1_CyTest 35_60kPa	0.05897	101655	0.07	6.62					
cy100_CyTest 35_60kPa	0.05808	103134	0.05	4.95	0.68	1.22	9.02	7.20	4.95
cy1_CyTest 36_70kPa	0.09049	77296	0.11	11.46					
cy100_CyTest 36_70kPa	0.08095	86328	0.07	7.03	0.57	1.71	10.42	10.21	6.99
cy1_CyTest 38_80kPa	0.10410	76776	0.10	10.33					
cy100_CyTest 38_80kPa	0.09938	80358	0.08	8.36	0.53	2.09	11.26	11.40	7.77
cy1_CyTest 40_90kPa	0.13083	68720	0.13	13.02					
cy100_CyTest 40_90kPa	0.12098	74263	0.10	9.97	0.49	2.55	12.05	12.67	8.61
cy1_CyTest 41_100kPa	0.16597	60183	0.16	16.05					
cy100_CyTest 41_100kPa	0.14610	68322	0.12	11.83	0.45	3.08	12.79	13.97	9.46

Figure 3-4 Interpreted TOSS measurement data. Two confinement stages and several shear stress amplitudes are shown with cycle 1 and cycle 100

In all further graphs, stiffness and damping values of cycle 100 was plotted for each TOSS test unless noted otherwise. The magnitude of the effect can be assessed for each TOSS test, because in the measurement results both cycles 1 and 100 are shown; see Annex C.

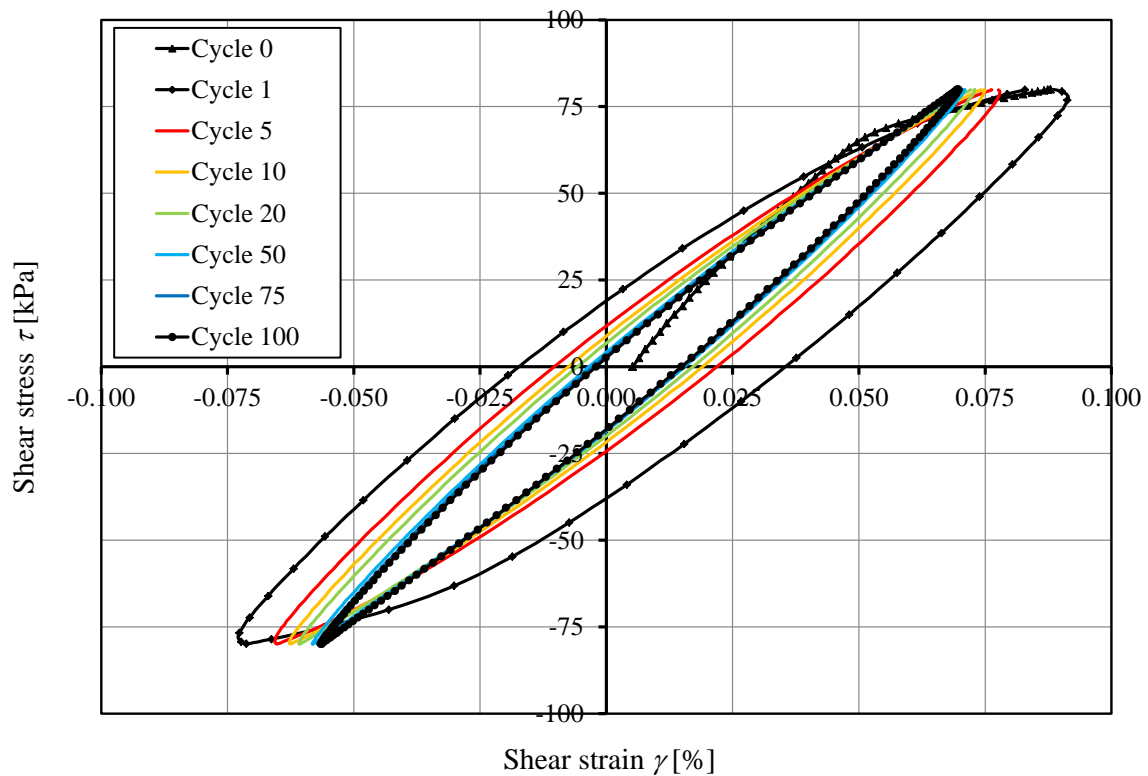


Figure 3-5 Effect of number of cycles in TOSS test

Stress-strain response to an irregular load history is shown in Figure 3-6. Note the intermediate turnaround points resulting in smaller unload-reload loops with steeper secant value showing small strain stiffness. Such load histories can be used to study whether the extended Masing rules apply for the tested material, however the scope of this thesis did not comprise of the detailed investigation of irregular load histories.

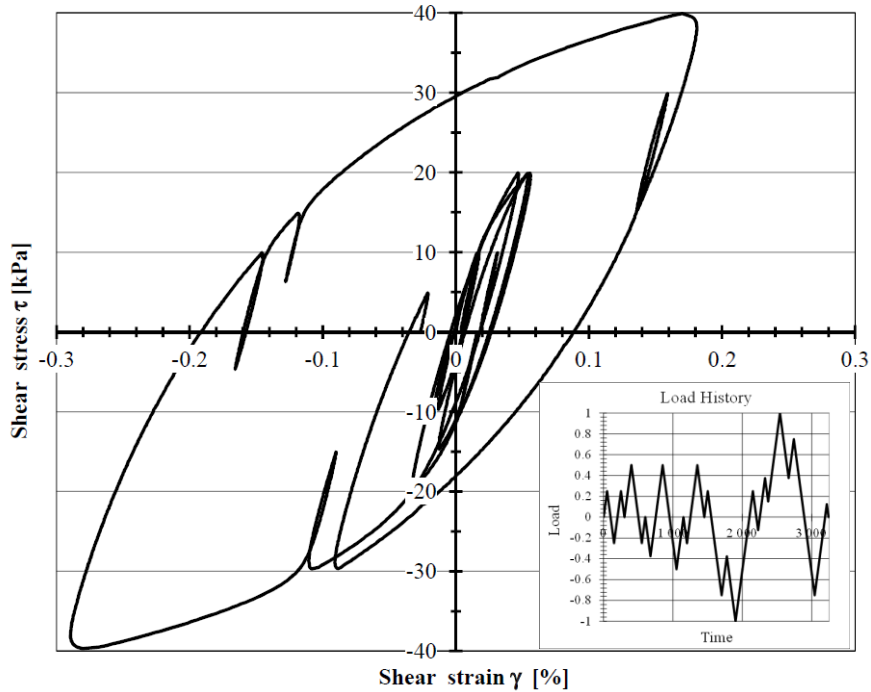


Figure 3-6 Stress-strain response to an irregular load history in TOSS test

Another topic of result interpretation has to be addressed concerning damping in the Ramberg-Osgood material model presented earlier. The formulation presented in Chapter 2.1.4 does not give an equation for calculating damping directly. Therefore, a numerical integration procedure has been developed to calculate damping based on the hysteresis loop using Equation 2-8. The integration of half of the loop can be performed along the stress axis with use of the differential element shown in Figure 3-7.

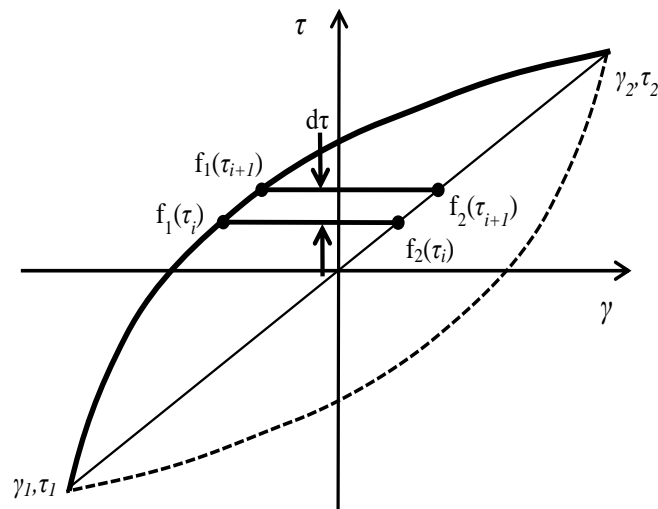


Figure 3-7 Numerical integration for obtaining hysteretic damping with the Ramberg-Osgood material model

The formulation for f_1 and f_2 is the following:

$$f_1(\tau) = \gamma = \frac{\tau - \tau_1}{G_{max}} \left(1 + \alpha \left| \frac{\tau - \tau_1}{2 C \tau_{max}} \right|^{R-1} \right) + \gamma_1 \quad \text{Equation 3-7}$$

$$f_2(\tau) = \frac{(\tau - \tau_1)(\gamma_2 - \gamma_1)}{\tau_2 - \tau_1} + \gamma_1 \quad \text{Equation 3-8}$$

Let us introduce the variables a , b , c as:

$$a = \frac{1}{G_{max}}, \quad b = \frac{\alpha}{(2 C \tau_{max})^{R-1}}, \quad c = \frac{\gamma_2 - \gamma_1}{\tau_2 - \tau_1} \quad \text{Equation 3-9}$$

This way f_1 and f_2 can be calculated as:

$$f_1(\tau) = a (\tau - \tau_1) + ab (\tau - \tau_1)^R + \gamma_1 \quad \text{Equation 3-10}$$

$$f_2(\tau) = c (\tau - \tau_1) + \gamma_1 \quad \text{Equation 3-11}$$

Then the integration can be written as:

$$\int_{\tau_1}^{\tau_2} f_2(\tau) - f_1(\tau) d\tau = \int (c - a)(\tau - \tau_1) d\tau - \int ab (\tau - \tau_1)^R d\tau \quad \text{Equation 3-12}$$

The integration of the total loop, which is the dissipated energy W_D then calculates as:

$$W_D = 2 \left(\frac{(c - a)(\tau_2 - \tau_1)^2}{2} - \frac{ab(\tau_2 - \tau_1)^{R+1}}{R+1} \right) \quad \text{Equation 3-13}$$

Damping then can be calculated using Equation 2-8. If the loading results in a symmetric loop, $\tau_1 = -\tau_2$, the calculation is even easier. Note, that to calculate damping with a given γ value, τ_1 has to be first calculated with the Newton Raphson method, because Equation 2-11 cannot be inverted. This calculation was programmed into a VBA function (ROHystDampingNew) to obtain damping with the Ramberg-Osgood model to be able to compare it with measured values. The code is presented in Annex B.

3.5 Application of measurement results in numerical modeling

This chapter focuses on the interpretation of measurement results needed to obtain material parameters to be applied in numerical modeling. For this the Ramberg-Osgood material model was chosen, which has been used by several authors recently for performing nonlinear ground response analysis. The model has been implemented by Midas into their finite element code (MIDAS Information Technology Co., 2014). To assess the modeling capabilities of the program and to present how small strain stiffness can be accounted for in numerical modeling, a

Torsional Shear test was modeled in 3D in Midas GTS NX. This modeling task has never been performed with a nonlinear material model capable of modeling modulus degradation.

Midas GTS NX is a comprehensive 3D geotechnical finite element software package. It is used for modeling deep foundations, excavations, tunnels, embankments etc. Static as well as dynamic calculations can be performed; consolidation, seepage and slope stability by the strength reduction method can also be modeled. It is a well-known program used worldwide with capabilities of modeling a wide range of geotechnical structures and problems.

When using geotechnical finite element programs, the processes of verification and validation are crucial, as discussed by (Brinkgreve & Engin, 2013). As they describe it, verification is the process of showing that a model or method has been properly implemented in a computer program; while validation is the process to make plausible that a computer model possesses the essential features to analyze a real problem and that the results obtained with it are representative for the situation. The former is usually done by the software developer and the latter should be done by the user when creating a model.

The test chosen for modeling provided the results shown in Figure 3-8 and Figure 3-9.

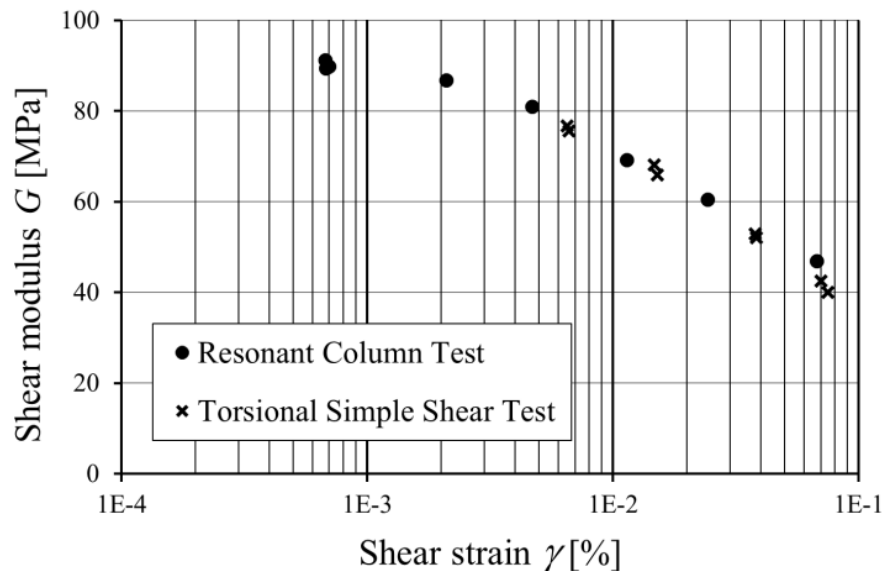


Figure 3-8 Modulus reduction curve obtained with Resonant Column-Torsional Simple Shear device

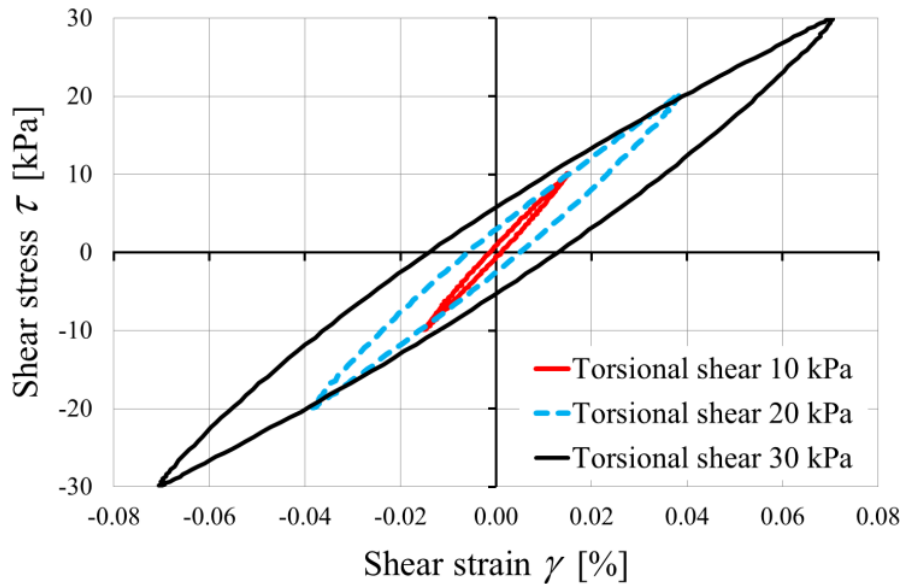


Figure 3-9 Hysteresis loops of Torsional Shear tests at different stress (strain) levels

Finite element modeling of such tests is a challenge. The geometry of the test is fundamentally axisymmetric; however, since the load is torsional, it is out-of-plane and requires a true 3D model using cylindrical coordinate system. A so-called 2.5D model or extended 2D axisymmetric model cannot reproduce a torsional load perpendicular to the model plane.

In Midas GTS NX, axisymmetric 3D modeling can be performed by defining a global cylindrical coordinate system or using the cylindrical element coordinate system. For this study the latter was used. Figure 3-10 shows a part of the model with the finite element mesh. Hexahedral high order elements with 20 nodes were used with an average size of 4x4x3 mm. Nodes on the grey soil elements can be seen in blue in Figure 3-10. This mesh was chosen so that three layers of elements would build up the cross section and so strain distribution could easily be assessed within the 1 cm thick hollow cylinder.

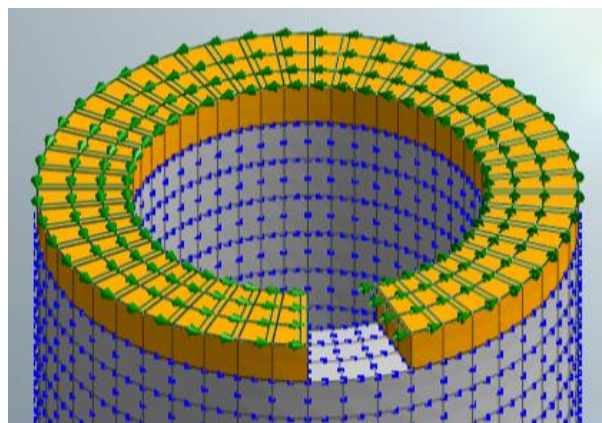


Figure 3-10 Detail of finite element mesh of soil sample and steel ring (partially invisible)

Figure 3-10 also shows yellow elements on top of the hollow cylinder soil sample, representing the steel ring, which transfers the load to the soil sample. A part of this ring is switched off to better show soil elements. The imposed torsional load is modeled as surface stress acting in the rotational (θ) direction of the cylindrical element coordinate system. Without this option, an imposed node load would act in a tangential direction, which does not reflect true behavior in this case.

The mesh consisted of 4032 elements. Mesh size dependency was checked and even a coarser mesh with one layer of high order elements and a total number of 162 elements showed identical results.

Pinned boundary conditions were used on the bottom surface of the soil sample since in the test the soil directly connects to the rough surface of the porous stone. It should be noted that some stress irregularities were observed even in the fine mesh close to the base fixity when using fully fixed boundary conditions (fixed against translation and rotation in each direction). The irregularities with pinned fixities were minor, see Figure 3-11. Since the testing device is free on top and the self-weight of the drive head is counterbalanced by a calibrated vertical spring, no other fixities have to be introduced in the model.

Calculation stages consisted of initial stress generation, confinement activation (with free face surface pressure acting in normal direction of the element faces) and torsional loading stages. This can be done in the software by defining construction stage sets and setting up construction stage analysis cases. An important modeling step is to set up the output control before starting the calculation. Here parts of the mesh can be chosen which will be used for documentation. While the calculation will be performed for the whole mesh, results will only be saved for these selected elements, therefore result size can be reduced. This still might be crucial for 3D FEM calculations, e.g. one stage with the fine mesh produces around 800 MB results. Result types can also be adjusted here and it should be remarked that strains in solid elements are turned off by default which can cause some initial confusion for some users.

Formulation of the material model has been presented in Chapter 2.1.4. An additional modeling detail is that an option of using the model in “shear only” mode is available in the program, which was used in this study. Unfortunately, the effects of this option are not detailed in the manual, however the online release notes explain that if this mode is used, shear modulus will be different in each direction separately (G_{xy} , G_{yz} , G_{zx}), otherwise an equivalent shear modulus will be used (G_{eq}). While this information is somewhat helpful, there seems to be no way of inputting separate shear moduli and the formulation of G_{eq} is also not part of the manual as of the time of modeling.

Obtaining parameters for FEM models from various laboratory and field tests is also a challenging task because it involves the solution of an inverse problem. Some geotechnical FEM software offer built-in program modules for fitting curves of commonly used laboratory tests, e.g. Soil Test module in Plaxis, so that the user can assess the effects of changing a single parameter and chose the most appropriate set of parameters for the specific project. However, laboratory tests such as the Resonant Column or Torsional Shear Test are not yet implemented in any of the mentioned modules.

For this study, in order to obtain model parameters, the G_{max} value measured in a low strain Resonant Column test and the stress-strain values of a higher strain single hysteresis loop obtained from the Torsional Shear test were used. The measurement results were imported into MS Excel and the formulation of the material model was implemented into a Visual Basic code. Then, with a set of initial values for γ_{ref} and h_{max} the response of the model was calculated. Due to the properties of the formulation, if a full hysteresis loop is used, the turnaround point has to be specified in advance as well. Then, at each data point, the square of the error could be obtained and sum of the squared errors could be calculated. In MS Excel, the Solver module was then used to choose model parameters with the best fit, namely the nonlinear GRG method (Generalized Reduced Gradient) was applied to minimize the sum of square of the errors by allowing Solver to change the two model parameters and solve the inverse problem. The obtained model parameters are summarized in Table 3-1.

Table 3-1 Ramberg-Osgood material model parameters obtained from back analysis

<i>Parameter</i>		<i>Value</i>	<i>Dimension</i>
<i>Small strain stiffness from RC test</i>	G_{max}	91 161	[kPa]
<i>Reference shear strain</i>	γ_r	8.1372×10^{-4}	[-]
<i>Max. damping constant</i>	h_{max}	0.19043	[-]
<i>Dry density</i>	γ_d	16.15	[kN/m ³]
<i>Poisson's ratio</i>	ν	0.3	[-]

A practical remark has to be mentioned here; the GRG method works dependably if the values of the model parameters are fitted are of a similar order of magnitude. This can be achieved by simply scaling the parameters in the formulation (e.g. using a parameter value 100x larger, and then dividing it by 100 in the formula).

Horizontal stresses after the 84kPa confinement step are shown in Figure 3-11. Some minor irregularities can be observed near the base fixities.

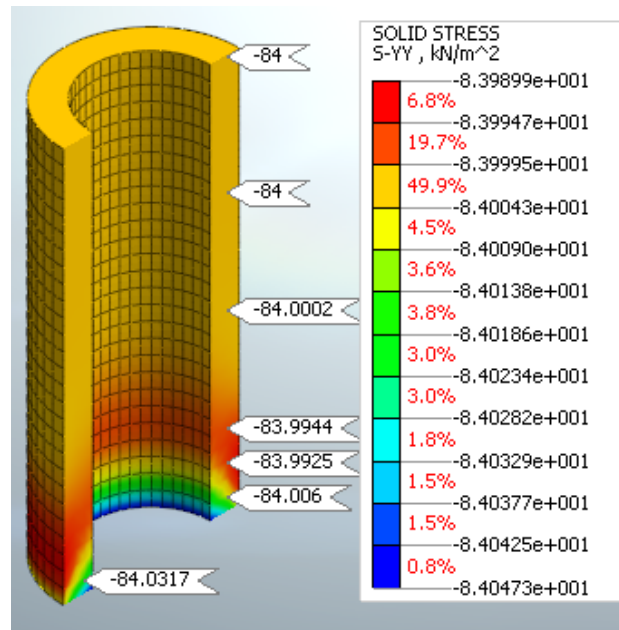


Figure 3-11 Distribution of horizontal stresses after confinement activation

A one-way loading stress-strain curve is shown in Figure 3-13. Stress and strain values were taken as the average of the values from the three layers of elements in the cross section. This average was found to be almost identical to the value in the middle element, see Figure 3-12. Response of the inside element and outside element follow the same stress strain curve.

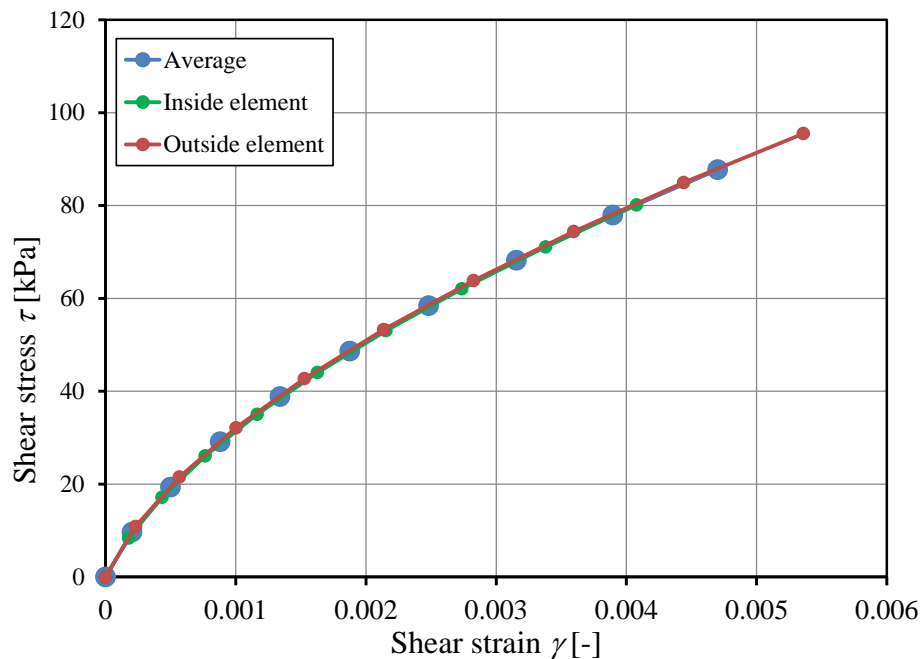


Figure 3-12 Comparison of shear stresses in cross section

Agreement between the test, the formulation and the FEM calculation is excellent as shown in Figure 3-13.

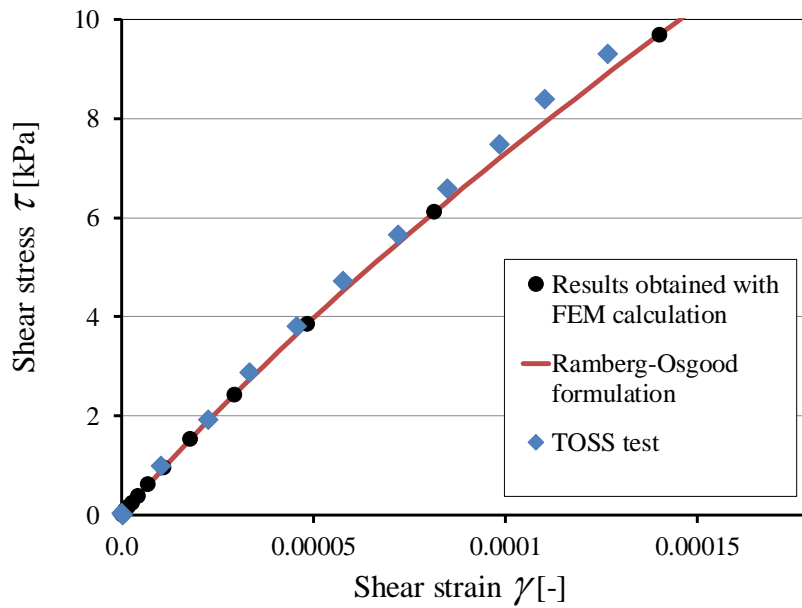


Figure 3-13 Stress-strain curve by FEM calculation and MIDAS Ramberg-Osgood formulation

Figure 3-14 and Figure 3-15 show the deformed mesh and the distribution of total deformations in the mesh. The horizontal shear of the elements is clearly observable.

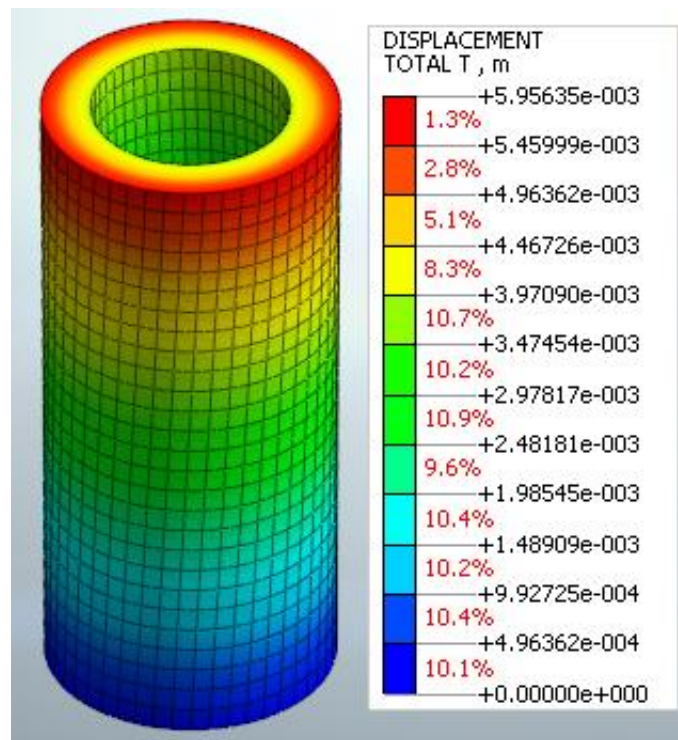


Figure 3-14 Deformed mesh at turnaround point of loading

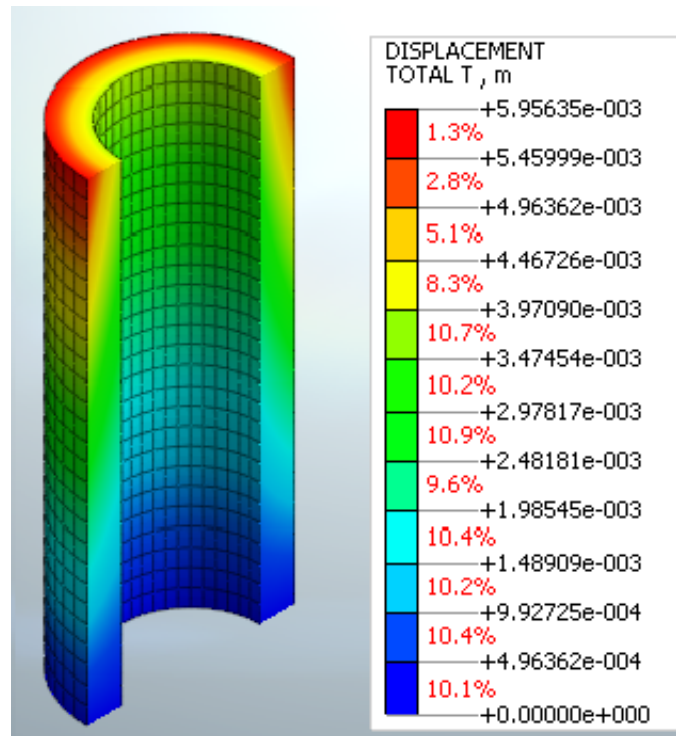


Figure 3-15 Distribution of total displacements at turnaround point of loading

Figure 3-16 shows shear strain distribution in the sample, which is even throughout the height of the sample. Also, the benefit of using a hollow cylinder for testing is demonstrated here; strain difference within the sample would be considerably higher in a full cylinder.

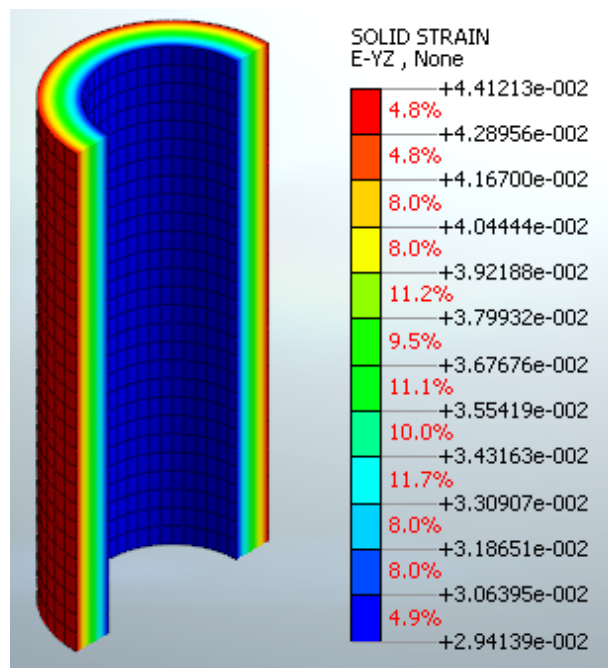


Figure 3-16 Shear strains at turnaround point of loading

The calculations were performed at several shear strain levels and based on the obtained shear stress and strain values; the secant shear modulus was calculated. Two-way loading was also applied. For this, manual load stepping was found to be beneficial. Load step size around turnaround points of the hysteresis loops should be gradually smaller to achieve a stable calculation. The developed manual load stepping method is shown in Figure 3-17.

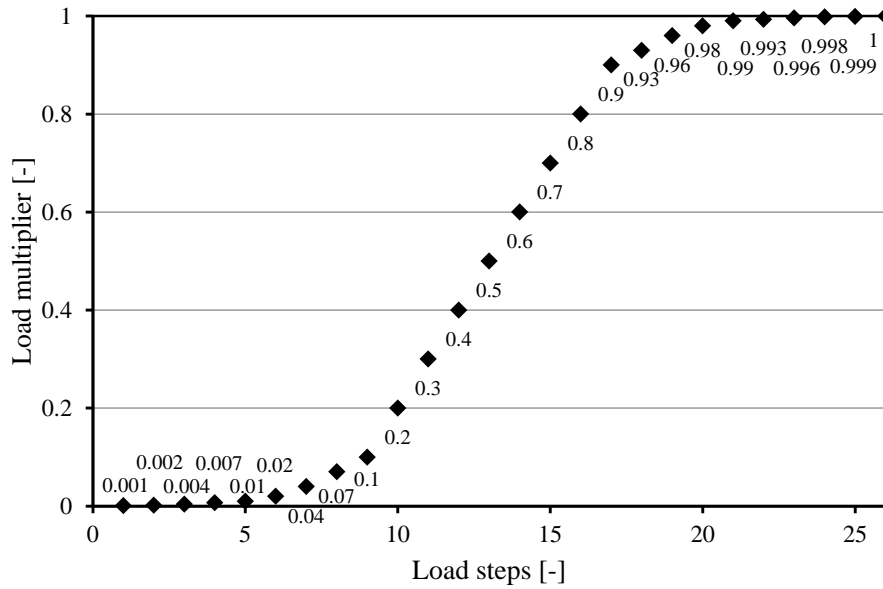


Figure 3-17 Manual load stepping used for stable calculation of hysteresis loop

Obtained hysteresis loop overlaps with the test results perfectly. Result of a single loop is shown in Figure 3-18.

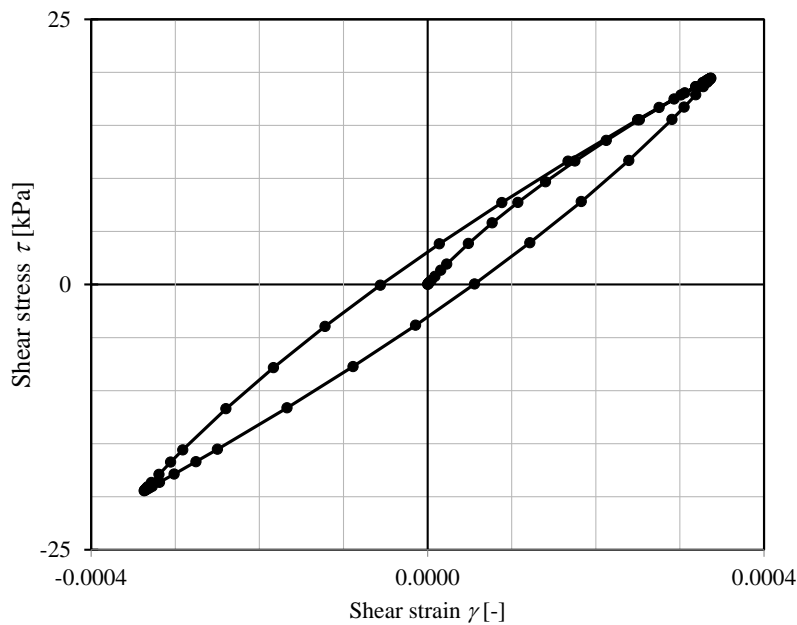


Figure 3-18 Hysteresis loop obtained with FEM calculation

Hysteresis loops for several stress levels are shown in Figure 3-19.

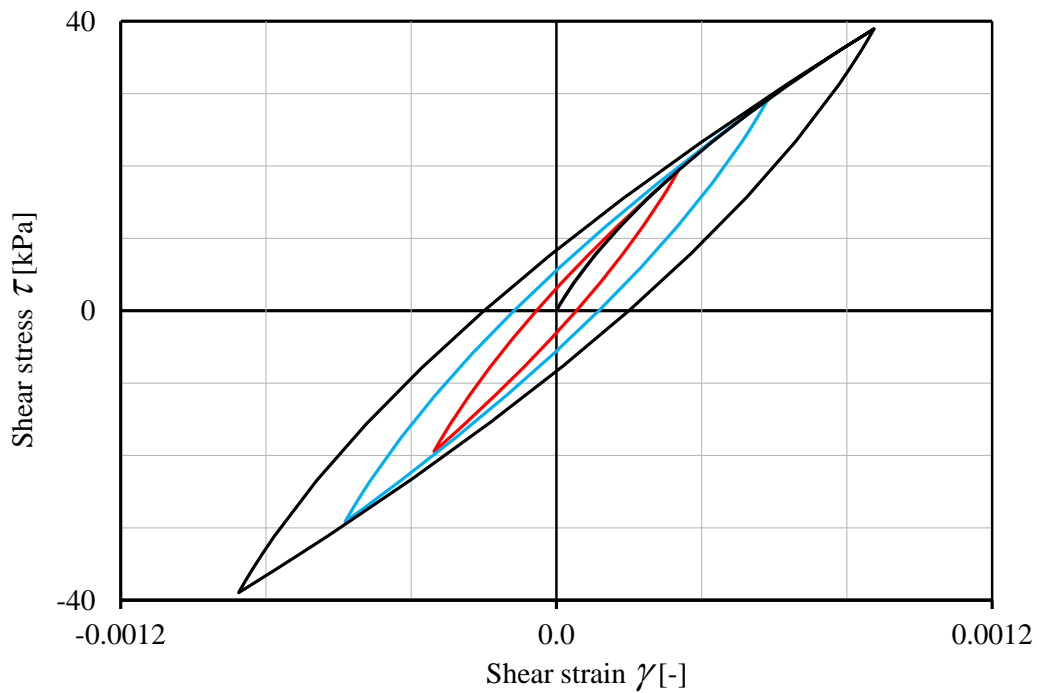


Figure 3-19 Hysteresis loops obtained from two-way sequential loading in Midas

Figure 3-20 shows the normalized modulus degradation curve compared to the test data.

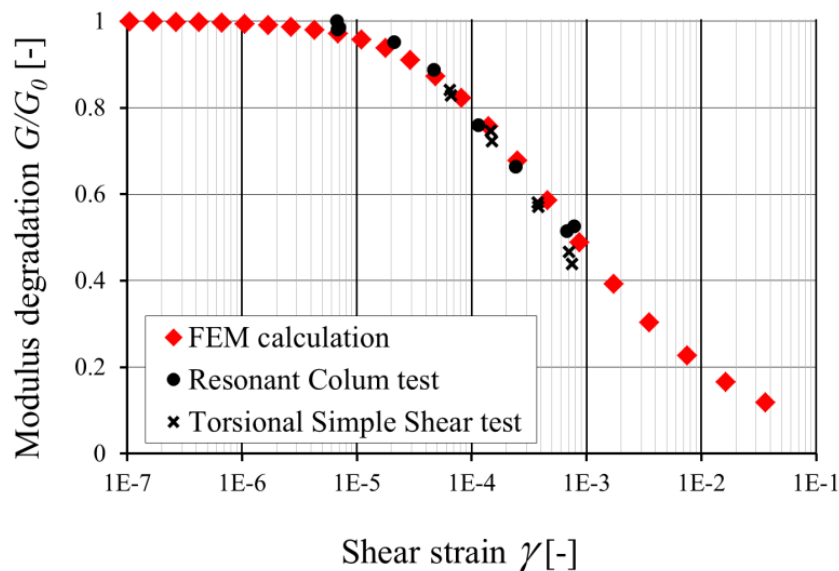


Figure 3-20 Modulus reduction curve by FEM calculation and RC-TOSS tests

This study verified that the Ramberg-Osgood material model implemented in MIDAS GTS NX v2014 is capable of modeling this static 3D cylindrical laboratory test with represen-

tation of nonlinear material behavior. The model also captured modulus degradation and hysteretic behavior. Sequential two-way loading modeling showed very good agreement with test results.

Some minor modeling difficulties have been pointed out. The use of manual load stepping and smaller load step size before and after the turnaround point was found to be beneficial to achieve a stable calculation. This confirms the general expectation, that to calculate more complicated load histories, such as recorded earthquake load histories, a smaller load step size may be required when using automated load stepping.

4 Testing program and results

4.1 *Materials investigated and test matrix*

Nine samples of granular soils were selected for testing in the laboratory program. They are all fluvial sediments of the Danube River. Danube sands are present throughout Hungary and are often encountered in large construction projects near the river as well as former river meanders. They often have a wide variation of in-situ density and may contain a significant percentage of fines; generally, with low plasticity. Other zones contain a significant percentage of gravel which is very difficult to evaluate in laboratory tests. The samples were retrieved from depths of 5-15 m from a hollow-stem auger sampler and weighed 2-3 kg. Main parameters of the tested samples are summarized in Table 4-1. These samples are considered to be typical Danube sands.

Samples P1-P7 originate from the direct vicinity of the present channel of the River Danube around Paks. The stratigraphy of the coastline consists of Holocene age fluvial sediments; however, this fine sand terrace material is often mixed with aeolian particles. Original surfaces were probably deflated and accumulated in an alternating fashion. This diverse formation shaped the grain structure to its current state. Note that Sample P1 and P2 are a mixture of several natural sands. They were mixed in order to represent a “general” or “average” behavior of several sand strata at a specific site. Samples B1 and B2 originate from a site located in the Danube Terrace in Budapest. This location has a Miocene age base layer on which Holocene terrace sediments were deposited in many stages. During the Holocene age, the area became a basin shore with a flat surface full of alluvial terraces. The fluvial, coarser grained granular materials deposited by the river were deflated and blown by the wind in short distances. However, during flood periods fluvial effects also formed the surface. Generally, samples from both

locations show a quite complex grain structure with heterogeneous grain shapes, see Table 4-2. Typical grain shapes vary between sub-angular and rounded shapes.

In Table 4-1, the maximum void ratio (loosest state) was measured by pouring material through a funnel into a mold with a diameter of 50 mm and height of 100 mm and gently lifting the funnel to “bulk up” the soil. The minimum void ratio (densest state) was measured by filling the mold in three stages. After each stage, the vibration platform normally used for sieving was used to vibrate and compact the specimen while a small force was applied to the top of the specimen with a tamping rod. At least 5 tests were done for both loose and dense states. The maximum difference in weight was ± 5 g which would change void ratio by about 0.04. Usually the measured values varied about ± 3 g from the average value ($e \pm 0.03$).

Table 4-1 Soil properties of tested samples

Sam- ple ID	Mean part. di- ameter	Effective part. di- ameter	Uni- form. coeff.	Fines content	Max void ratio	Min void ra- tio	Spe- cific density	Liq. limit for fines	Plastic limit for fines	Plast. index for fines
	d_{50} [mm]	d_{10} [mm]	C_U [-]	FC [%]	e_{max} [-]	e_{min} [-]	ρ_s [g/cm ³]	w_l [%]	w_p [%]	I_p [%]
P1	0.243	0.130	2.18	5.69	0.788	0.516	2.680	-	-	-
P2	0.424	0.193	2.38	1.32	0.699	0.474	2.659	-	-	-
P3	0.365	0.160	2.74	0.25	0.677	0.453	2.660	-	-	-
P4	0.179	0.010	20.7	16.75	0.849	0.476	2.670	33.0	17.3	15.7
P5	0.322	0.151	2.50	3.26	0.762	0.488	2.664	-	-	-
P6	0.211	0.109	2.06	7.56	0.790	0.494	2.674	36.6	18.2	18.4
P7	0.107	0.013	9.85	21.11	0.949	0.524	2.708	30.4	19.7	10.7
B1	0.191	0.007	30.9	18.84	0.876	0.418	2.678	32.3	21.0	11.3
B2	0.218	0.109	2.17	3.05	0.761	0.496	2.654	-	-	-

Grain size distribution curves are shown in Figure 4-1. Most samples exhibit uniform grain size as medium to fine sand, containing fines up to 21%. Atterberg limits of fines extracted from five samples were measured (Table 4-1). Plasticity index ranges from 10 -18 % and samples of fines were classified as clay with low to intermediate plasticity. It is believed that similar plasticity index is applicable for other samples where fines were not tested separately. Sample B1 and P3 contained a significant percentage of gravel. The gravel was removed for RC testing, but in a separate comparative study Bender Element tests were performed on both conditions for B1: with and without the gravel (Szilvagyi, Panuska, & Ray, 2018). The typical shape of the grains can be observed in Table 4-2.

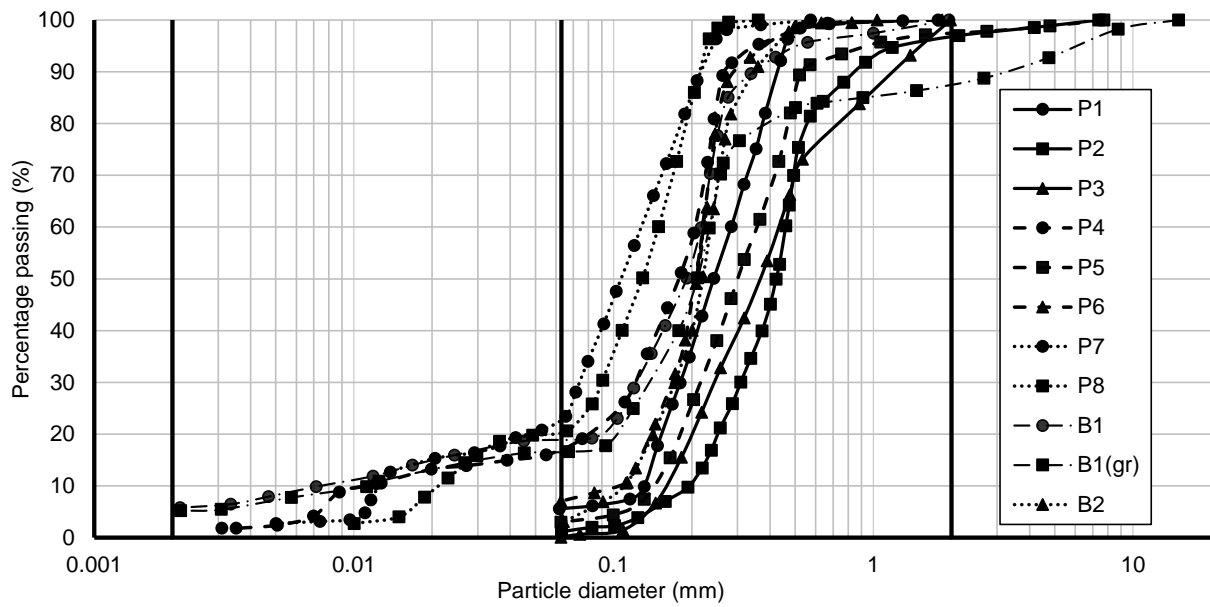
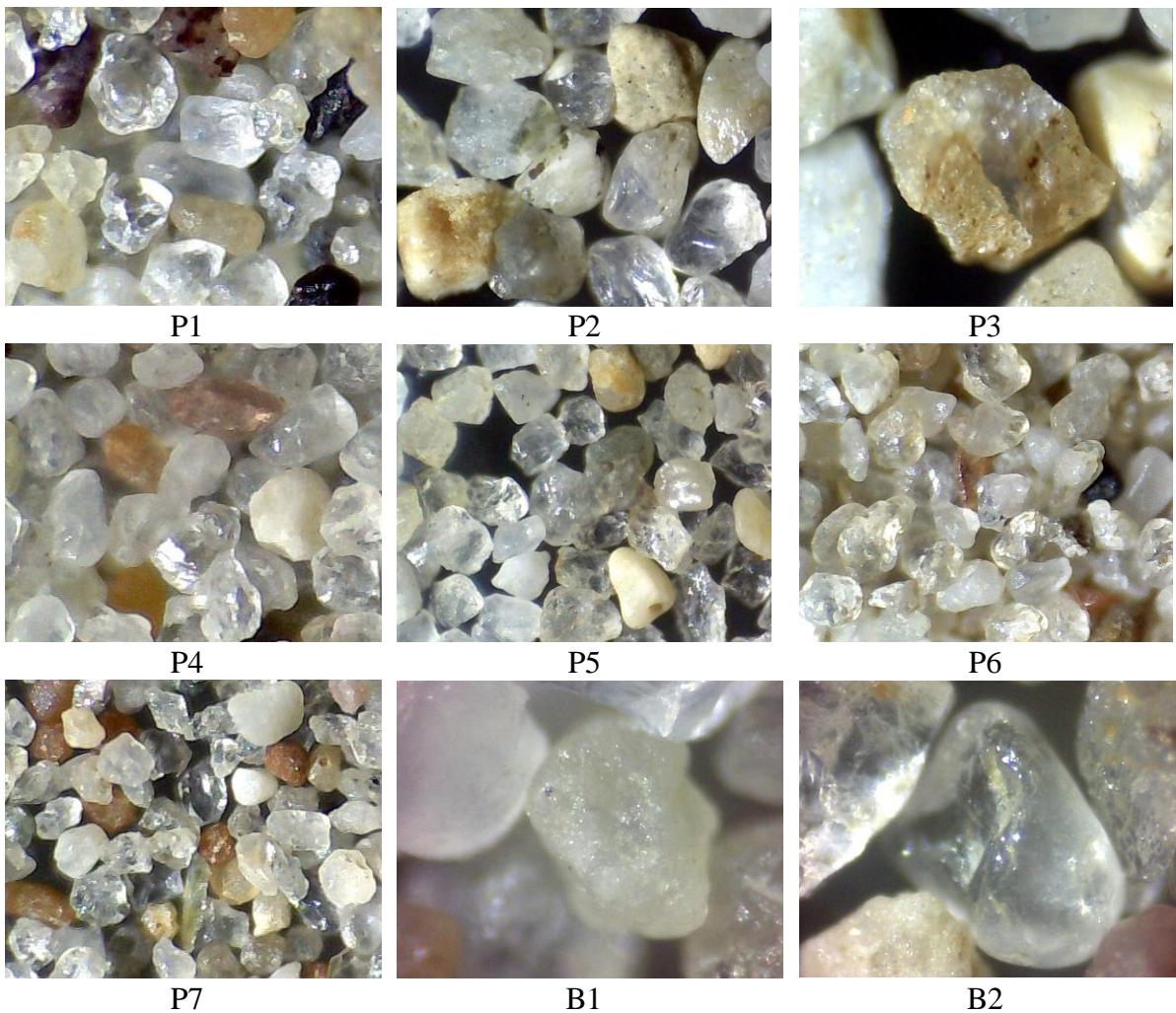


Figure 4-1 Grain size curves for soils tested. (Note that P8 and B1(gr) were only tested by bender elements in the comparative study)

Table 4-2 Photos of typical grain shapes – not to scale



Note that the photos were taken after washing the soil, with a regular digital handheld camera and they are not to scale; the purpose of showing them is solely to preview particle shape of the main grains.

The testing program consisted of measurements at a wide range of void ratios and all relevant confinements. All RC-TOSS tests were performed on dry samples under isotropic confinement. The testing conditions for all confinement and density states are summarized in Table 4-3.

Table 4-3 Test matrix

Sample ID	Test type	Confinement p' [kPa]	Void ratio e [-]	Relative density D_r [-]
P1	RC-TOSS	77; 160	0.572	0.79
		85	0.659	0.47
		74; 160; 240	0.757	0.11
P2	RC-TOSS	84; 160; 220	0.454	1.09
		79; 160; 240	0.663	0.16
P3	RC-TOSS	80; 160	0.637	0.14
		57; 120; 180	0.596	0.34
P4	RC-TOSS	65; 73	0.617	0.62
		100; 150; 200; 250; 300	0.650	0.53
P5	RC-TOSS	75; 100; 150; 200; 250; 300	0.512	0.91
		78; 180	0.634	0.47
P6	RC-TOSS	75; 100; 150; 200; 250; 300	0.569	0.75
		75	0.644	0.49
P7	RC-TOSS	75; 100; 150; 160; 200; 250; 300	0.571	0.89
		160	0.677	0.64
B1	RC-TOSS	77; 115; 150; 180; 200; 240; 300	0.621	0.56
		62; 115; 180; 240	0.761	0.25
B2	RC-TOSS	77; 100; 150; 200; 250; 300	0.512	0.94
		60; 100; 150; 200; 250; 300	0.570	0.72

Void ratios listed in the table represent conditions at the beginning of a test, usually obtained under 80 kPa confinement for RC. The listed confining stresses were applied as an increasing sequence. One value of $D_r=1.09$ for Sample P2 deviates from maximum density which could be related to slightly inaccurate volume measurements on the hollow cylinder.

RC-TOSS results were also compared to a set of independent measurements with the bender element (BE) method performed on the same soil samples by Jakub Panuska at the Department of Geotechnics at the Slovak University of Technology in Bratislava. A comprehensive study was performed to compare results from the two laboratory testing methods, see (Szilvagyi, Panuska, & Ray, 2018). Bender Element tests were performed in a triaxial cell under comparable confinement and density conditions.

In the comparative study, piezoelectric bender elements were installed in the top cap and bottom pedestal of a Bishop and Wesley triaxial cell. The BE could produce both shear and compression waves, but for this study only shear waves were evaluated in detail. Three types of excitation signals were used with peak to peak driving amplitudes of 28 V and different frequencies. The signals were: single sine wave (3-20 kHz), four sine wave group (10-17 kHz), and linear sine sweep burst (5-50 kHz). The different signals and frequencies were chosen to better reveal the behavior of the entire system (triaxial device assembly, bender elements, soil sample) (Camacho-Tauta, Cascante, Viana Da Fonseca, & Santos, 2015) and secondary effects such as dispersion (Greening & Nash, 2004), near-field effects and overshooting (Jovicic, Coop, & Simic, 1996). A signal stacking procedure was used for some samples with ten stacks per one measurement to reduce noise in the signal. In BE testing data analysis is also an important part of evaluation of results. Several methods can be employed to evaluate travel time. "Observational" methods or characteristic point methods in the time domain such as Peak-to-Peak (*PtP*) and Start-to-Start (*StS*) are two often used approaches. Others are time domain methods such as Cross-Correlation (*CC*) or frequency domain methods (*FD*) which use phase delay to obtain travel time. These methods were used and compared in the evaluation process; finally travel time values obtained by the different methods fell generally into the range of $\pm 15\%$. Further details and discussion about the comparative study can be found in (Szilvagyi, Panuska, & Ray, 2018).

4.2 Measured G_{max} compared to correlations from literature and BE

Results from all tests were examined for measurement or procedural errors before including them in the dataset. Many preliminary tests were performed on these and other materials to validate procedure and data analysis. These included the topics of confinement time and dry vs. saturated testing. Figure 4-2 shows the results of an RC test lasting 20 days. The increase in G_{max} after 1000 minutes is less than 2.3% per log cycle of time which is in agreement with the findings of (Afifi & Richart, 1973) and can be considered negligible. In all further tests a 15-minute confinement period was applied after reaching a given confinement level, before starting measurements.

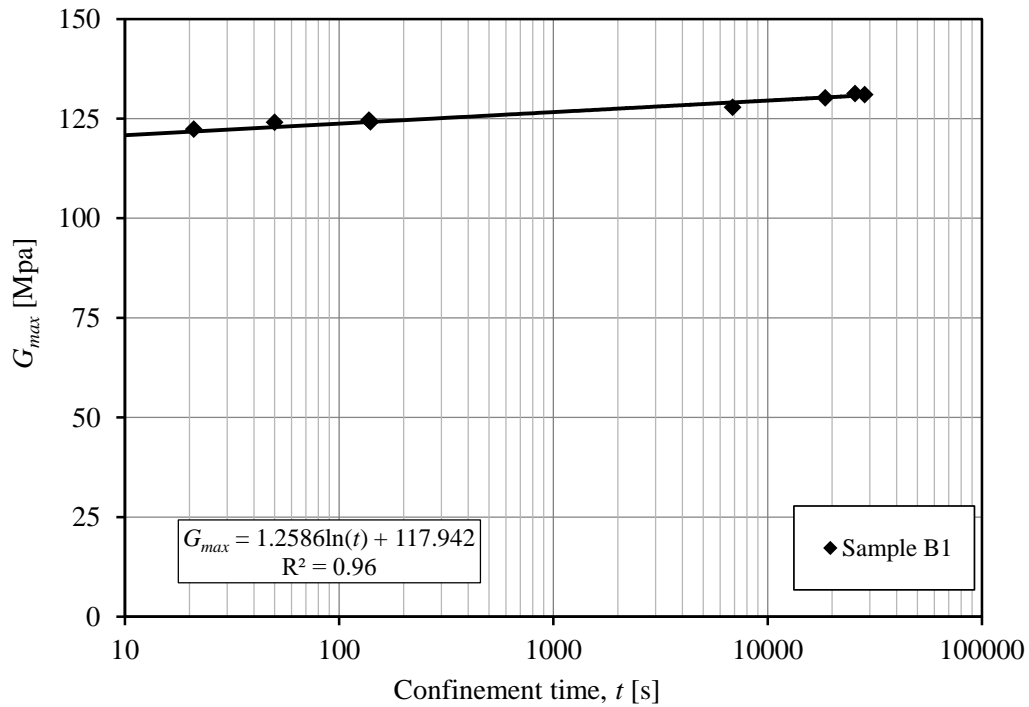


Figure 4-2 Effect of confinement time on G_{max}

Comparison of dry and fully saturated testing is shown in Figure 4-3. An excellent agreement between obtained G_{max} values and stiffness degradation can be observed.

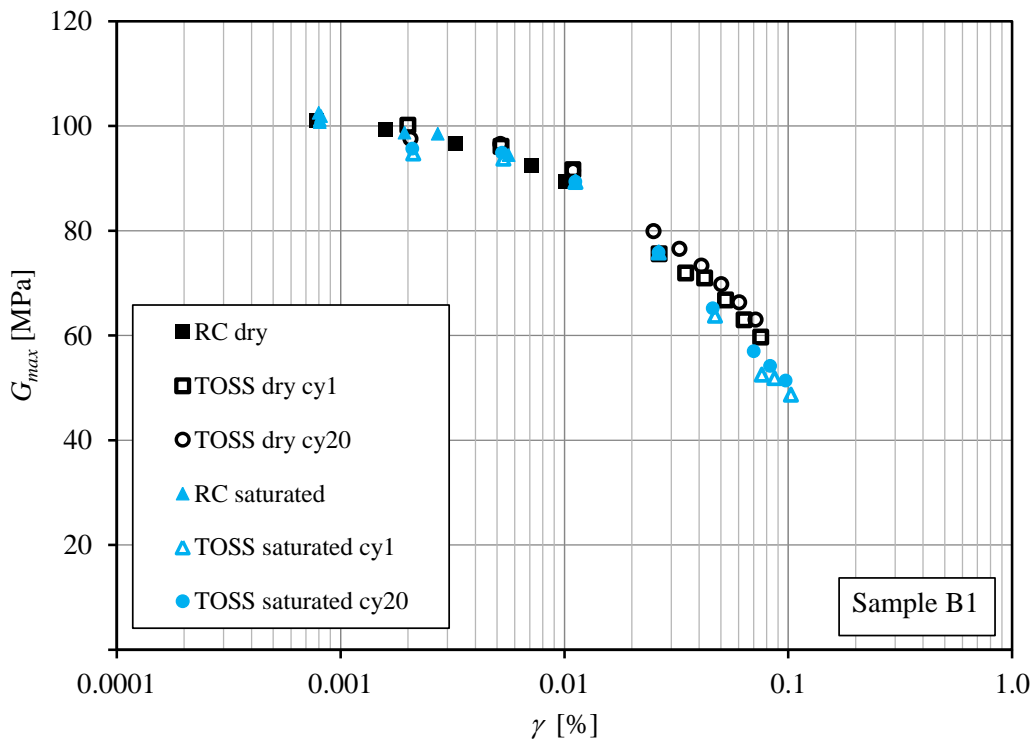


Figure 4-3 Comparison of dry and fully saturated test

Small strain stiffness for all samples measured by RC is shown in Figure 4-4. Note that Samples P4, P6, P7 and B1 (shown with circles) contained a considerable amount of fines (above 7%),

while all others only a slight amount, see Table 4-1. While the soils with fines seem to show a slightly lower G_{max} value at a given confinement, this plot cannot be used to assess any trends about fines, since the void ratios are different for almost every test. The influence of void ratio on G_{max} can be reduced by examining G_{max} normalized by a void ratio function and plotting the results versus confinement, as shown in Figure 4-5.

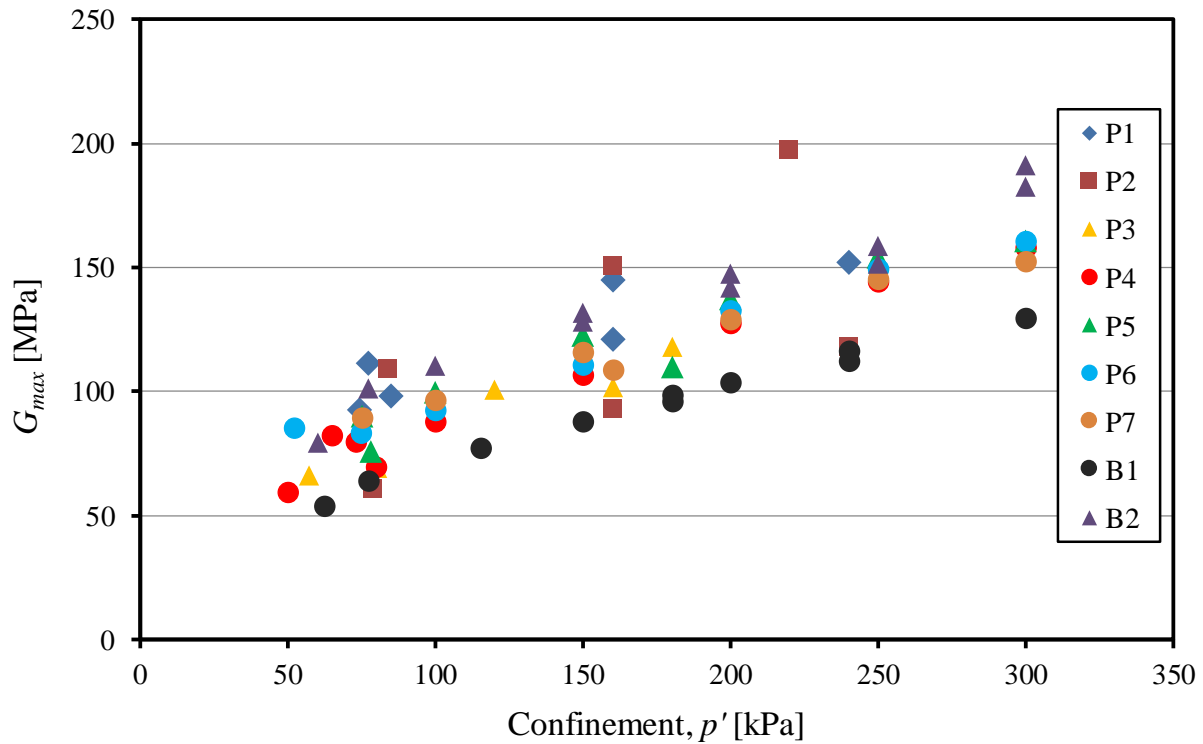


Table 4-4 Obtained intrinsic parameters for all tested soils (to be used with Equation 2-25)

Sample ID	Mean part. diam.	Uni-form. coeff.	Fines content	Intrinsic parameters for $G_{max}=A F(e) \left(\frac{p'}{p_{atm}}\right)^n$		Average of relative errors	Average of absolute values of relative errors	Coefficient of determination
	d_{50} [mm]	C_U [-]	FC [%]	A [-]	n [-]	$e_{rel,avg}$ [%]	$ e_{rel} _{avg}$ [%]	R^2 [-]
P1	0.243	2.18	5.69	80	0.51	2.1	7.7	0.73
P2	0.424	2.38	1.32	56	0.60	-3.1	7.3	0.96
P3	0.365	2.74	0.25	56	0.51	-0.3	2.2	0.99
P4	0.179	20.7	16.75	65	0.50	0.3	4.3	0.98
P5	0.322	2.50	3.26	57	0.42	0.3	2.2	0.99
P6	0.211	2.06	7.56	61	0.41	0.5	7.1	0.91
P7	0.107	9.85	21.11	62	0.39	0.3	2.7	0.96
B1	0.191	30.86	18.84	52	0.52	1.5	8.8	0.81
B2	0.218	2.17	3.05	64	0.50	1.8	10.2	0.73
Samples with fines*	-	-	-	60	0.44	-0.2	8.8	0.83
Samples without fines**	-	-	-	62	0.47	0.8	12.6	0.78
All samples	-	-	-	62	0.45	-1.1	11.2	0.71

*FC>7% **FC<7%

The fitted equations and normalized plots of G_{max} can be seen in Figure 4-5 and Figure 4-6. Note that the confinement exponent n was slightly different for the fits obtained for samples with fines, without fines and for all samples, so only one correlation can be visualized in Figure 4-6.

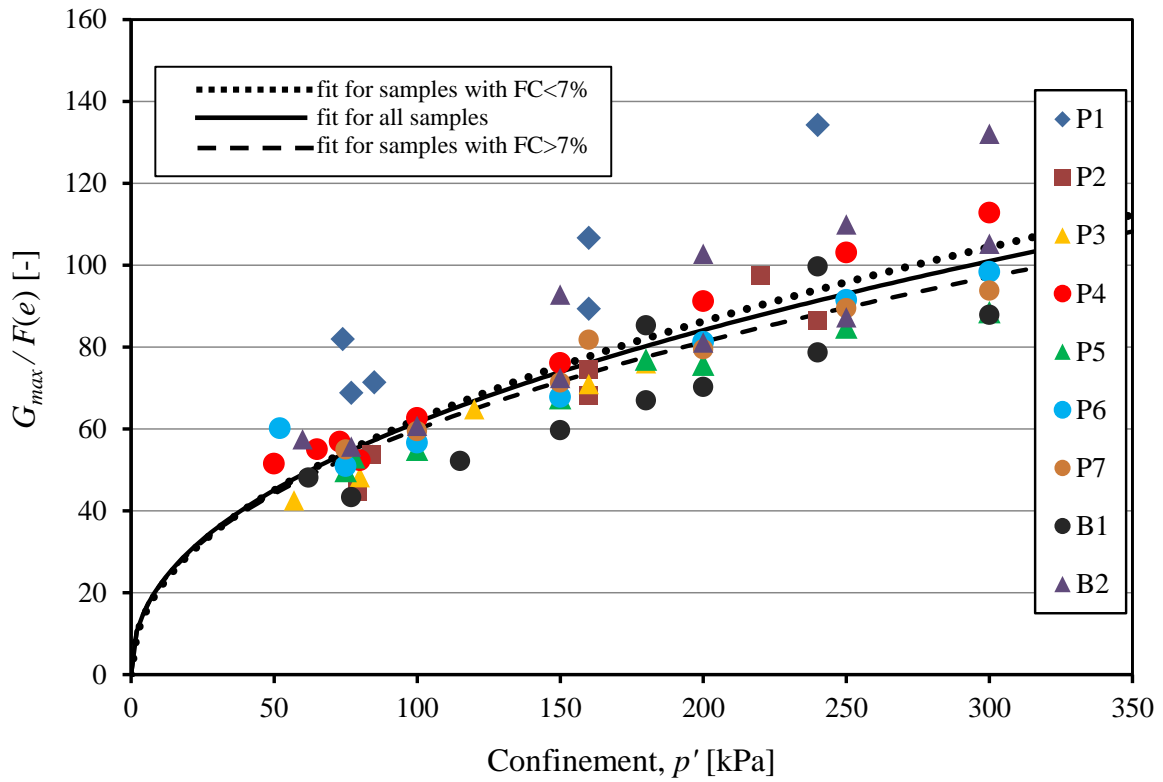


Figure 4-5 G_{max} normalized by void ratio function vs. confinement for all samples. (Soils with $FC > 7\%$ are shown with circles)

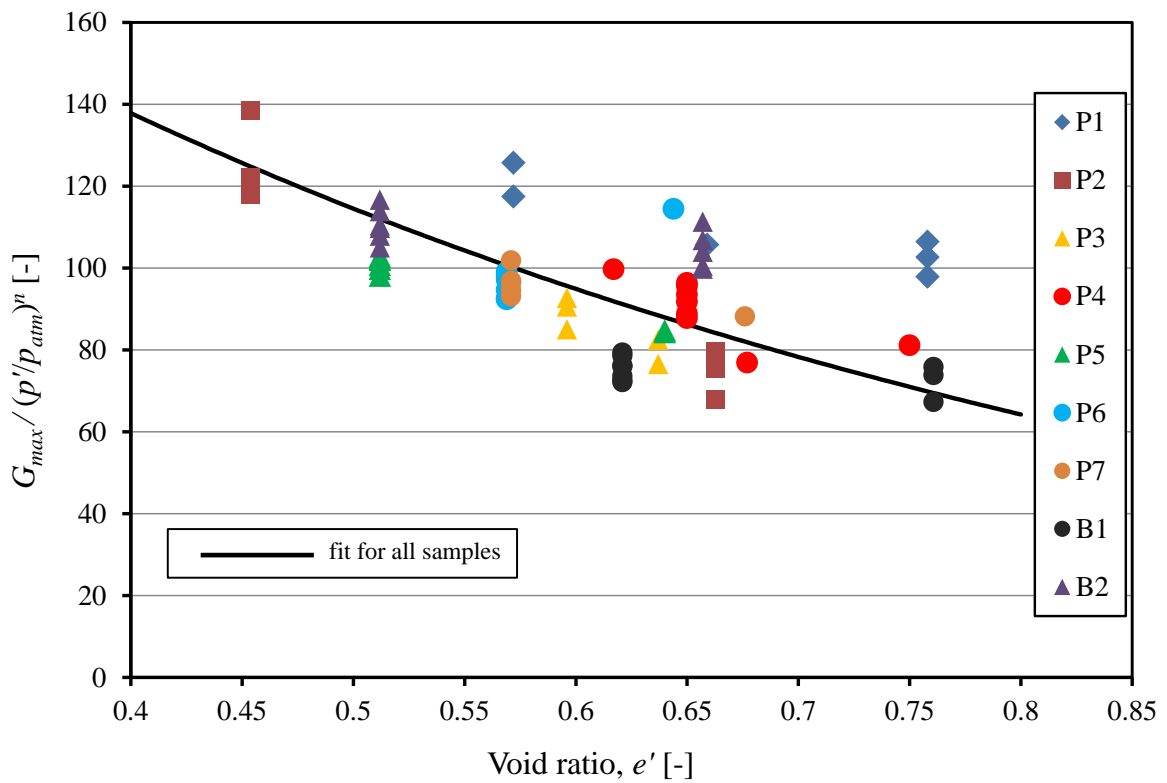


Figure 4-6 G_{max} normalized by confinement function vs. void ratio for all samples. (Soils with $FC > 7\%$ are shown with circles)

Some observations can be made based on Table 2-2, Figure 4-5 and Figure 4-6:

- The obtained intrinsic parameters A and n are in the range of values found in literature for similar soils, see Table 2-1 and Table 2-2.
- The high A value for sample P1 seems out of trend. This may be because it is a mixed soil with several grain shapes, although so is P2, for which a smaller A was obtained which is not out of trend.
- The fit for the soils with higher fines content ($FC > 7\%$, so P4, P6, P7 and B1) is not significantly different from the fit for the soils with lower fines content or the fit for all samples, only a slight reduction can be observed in G_{max} as FC is increasing. This is due to the fact, that fines in these soils are plastic ($IP = 10-18\%$), so the increase of FC does not result in a decrease in G_{max} as proposed by (Iwasaki & Tatsuoka, 1977) or (Wichtmann, Navarrete Hernandez, & Triantafyllidis, 2015). This tendency was also found by (Carraro, Prezzi, & Salgado, 2009).
- The fit for all samples given in Table 4-4 can be used to estimate G_{max} . This is shown in Figure 4-7, with lines of $\pm 15\%$. Out of the 69 measured G_{max} values 78 % lay within the $\pm 15\%$ margin with this correlation. 90% of the data points lay within the $\pm 20\%$ margin, so the obtained correlation gives a good estimation of the measured data.

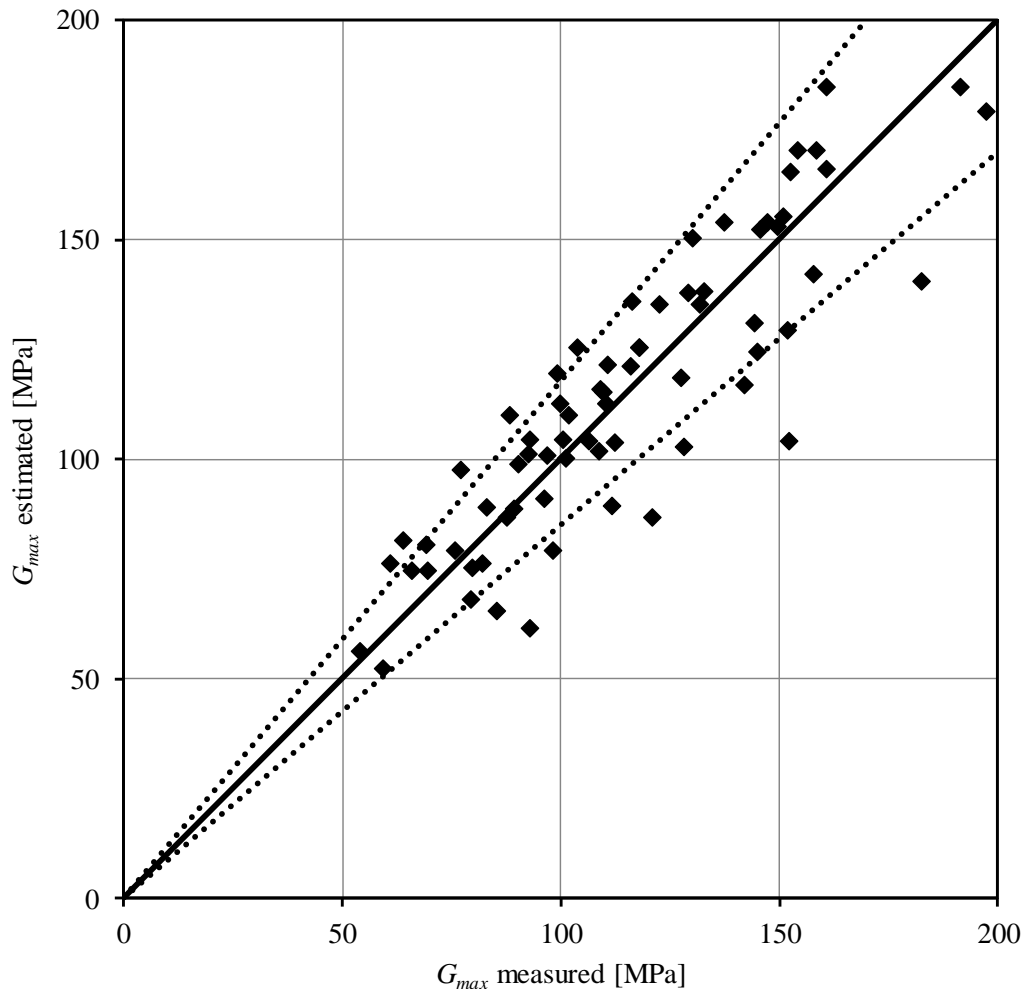


Figure 4-7 Measured vs. estimated G_{max} using the correlation obtained in this study for all samples in Table 4-4. Ranges of $\pm 15\%$ are given with dotted lines

In order to compare results to correlations for G_{max} given in literature, several authors' equations were investigated. A brief discussion follows about the most relevant ones.

The correlations obtained by (Carraro, Prezzi, & Salgado, 2009) for their sands containing plastic fines (kaolin clay with $IP=26\%$ up to $FC=10\%$) gave very good estimations for the soils investigated in this study, although plasticity of fines was lower ($IP=10-18\%$) and in three cases FC was higher (17%, 21% and 19% for P4, P7 and B1 respectively). Results are shown in Figure 4-8. For the samples with $FC < 10\%$ the correlation coefficients for the closest FC values in Table 2-2 were used. The fit is considered excellent, as 75 % of measured G_{max} values lie within the $\pm 15\%$ margin with this correlation. 87% of the data points lay within the $\pm 20\%$ margin.

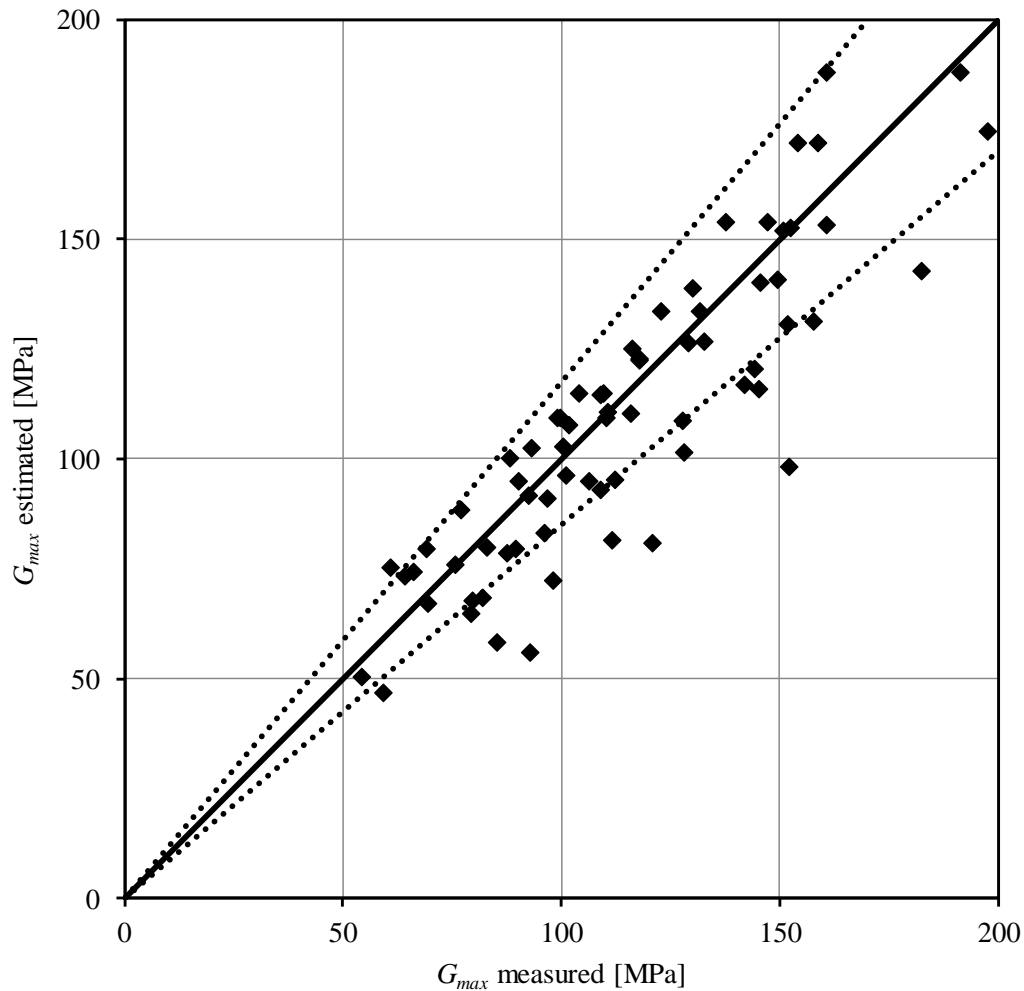


Figure 4-8 Measured vs. estimated G_{max} using the correlations given by (Carraro, Prezzi, & Salgado, 2009) in Table 2-2. Ranges of $\pm 15\%$ are given with dotted lines

A different void ratio function was suggested by (Biarez & Hicher, 1994) and while their correlation was given for an entire soil group with $w_l < 50\%$, which suggests it was originally obtained for fine grained soils, their correlation yields satisfactory results for the tested soils, see Figure 4-9. Out of the 69 measured G_{max} values 72 % lay within the $\pm 15\%$ margin with this correlation. 84% of the data points lie within the $\pm 20\%$ margin. This corresponds to $R^2=0.65$ for all tested soils.

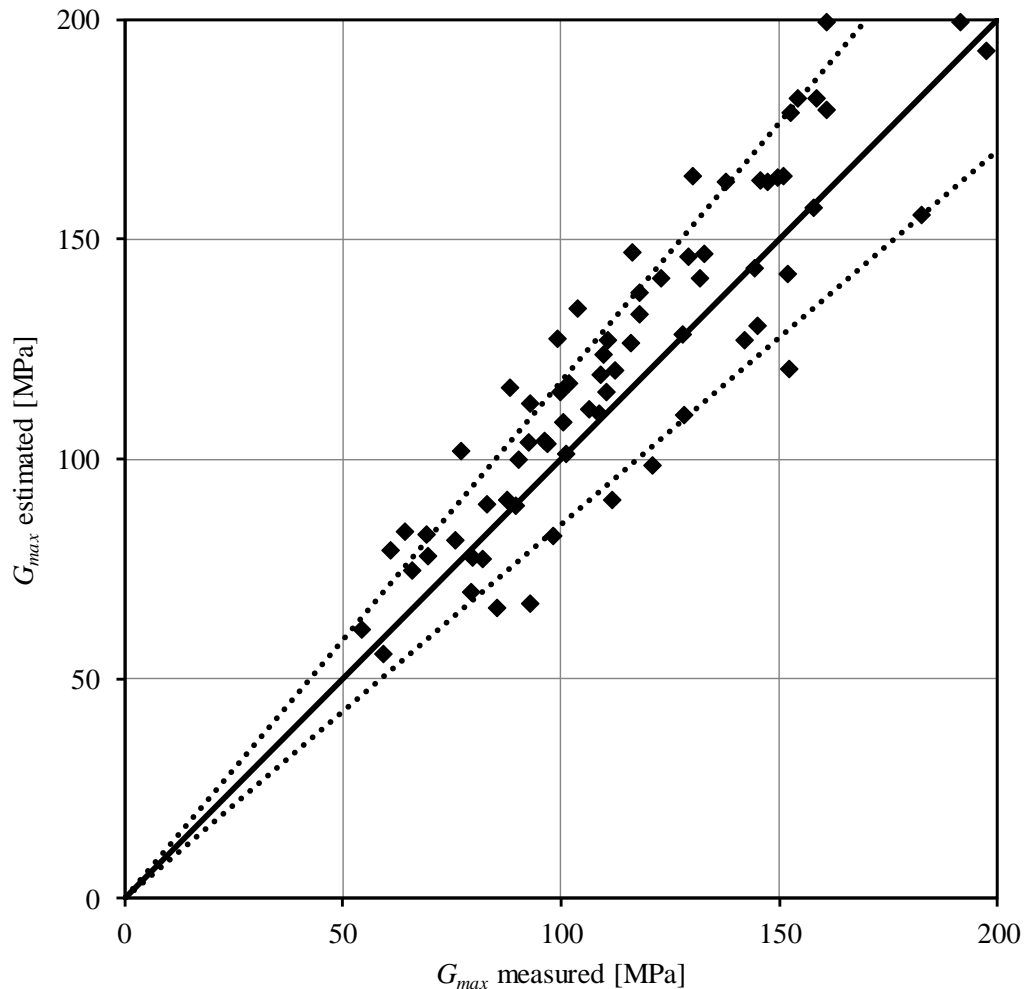


Figure 4-9 Measured vs. estimated G_{max} using the correlation given by (Biarez & Hicher, 1994) in Table 2-3. Ranges of $\pm 15\%$ are given with dotted lines

The correlations given by (Wichtmann & Triantafyllidis, 2009) and (Wichtmann, Navarrete Hernandez, & Triantafyllidis, 2015) were studied in detail, since they focused on the effects of grain size characteristics and fines content on G_{max} , although the fines in their study were nonplastic whereas the tested samples in this study have plastic fines. The authors argued that G_{max} of sands with nonplastic fines is decreasing with increasing fines content compared to clean sands; the reduction is given by Equations 2-26 to 2-29. Otherwise their tested soils had similar grain size properties as some samples in this study (P1, P2, P3, P5, P6, B2), so their correlations are applicable. All other samples (P4, P7, B1) had much higher C_U (from 10 to 31) and higher FC (17; 21; 19% respectively), so they were not considered in the comparison shown in Figure 4-10. The correlation for clean sands (Wichtmann & Triantafyllidis, 2009) tends to over-predict many measured results. 47% of data points lie within the range of $\pm 15\%$ and 60% of data points lie within the range of $\pm 20\%$. The correlation given for sands with nonplastic fines on the other hand introduces a too large reduction for these soils with a small content of

plastic fines (up to 7.6%). Goodness of fit is similar to previous equations: 51% of data points lay within the range of $\pm 15\%$ and 63% of data points lay within the range of $\pm 20\%$. Equations 2-26 to 2-29 underestimate G_{max} in some cases by more than 35%.

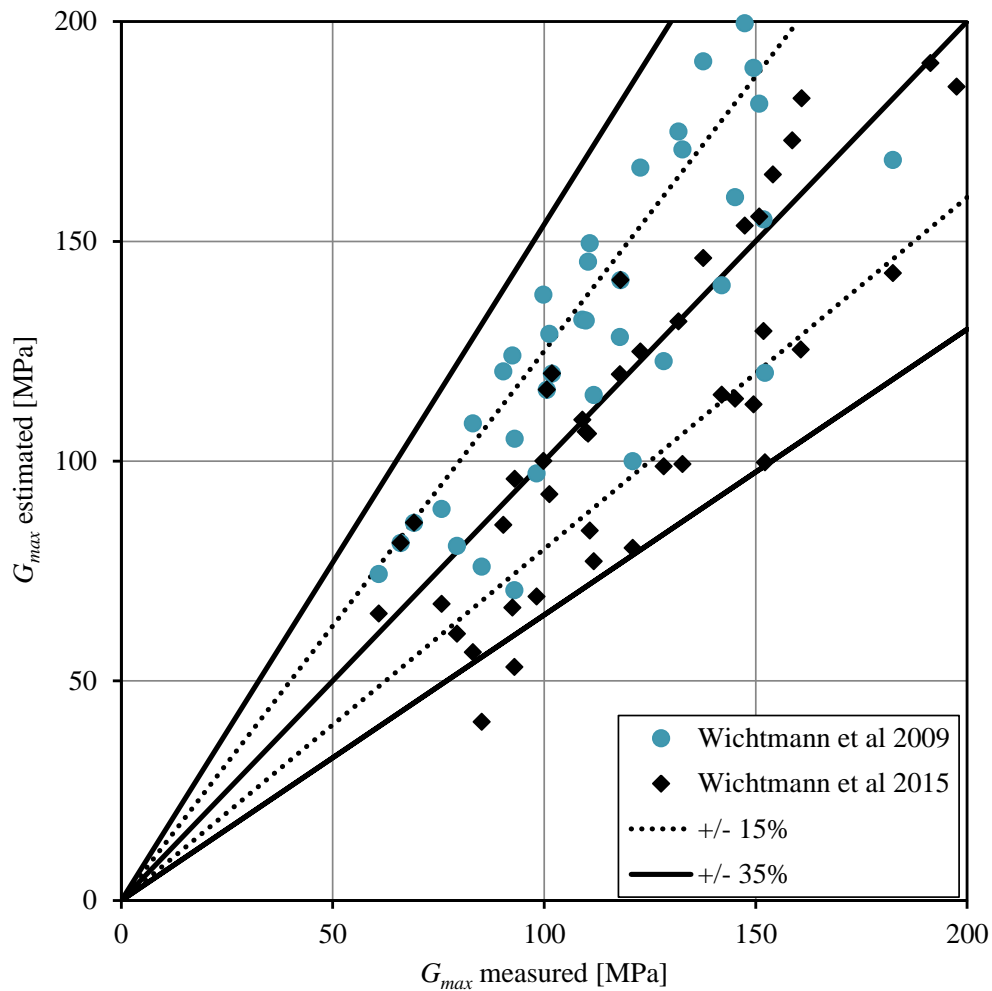


Figure 4-10 Measured vs. estimated G_{max} using the correlations given by (Wichtmann & Triantafyllidis, 2009) and (Wichtmann, Navarrete Hernandez, & Triantafyllidis, 2015) in Equations 2-26 to 2-29. Ranges of $\pm 15\%$ are given with dotted lines

Measured results were also compared to the correlation suggested by (Oztoprak & Bolton, 2013), see Figure 4-11. Their correlation shown in Equation 2-33 with the coefficients given in Table 2-5 overestimated most measured results, however estimated values are within the range of $\pm 100\%$, which was also found by them for most of the gathered data.

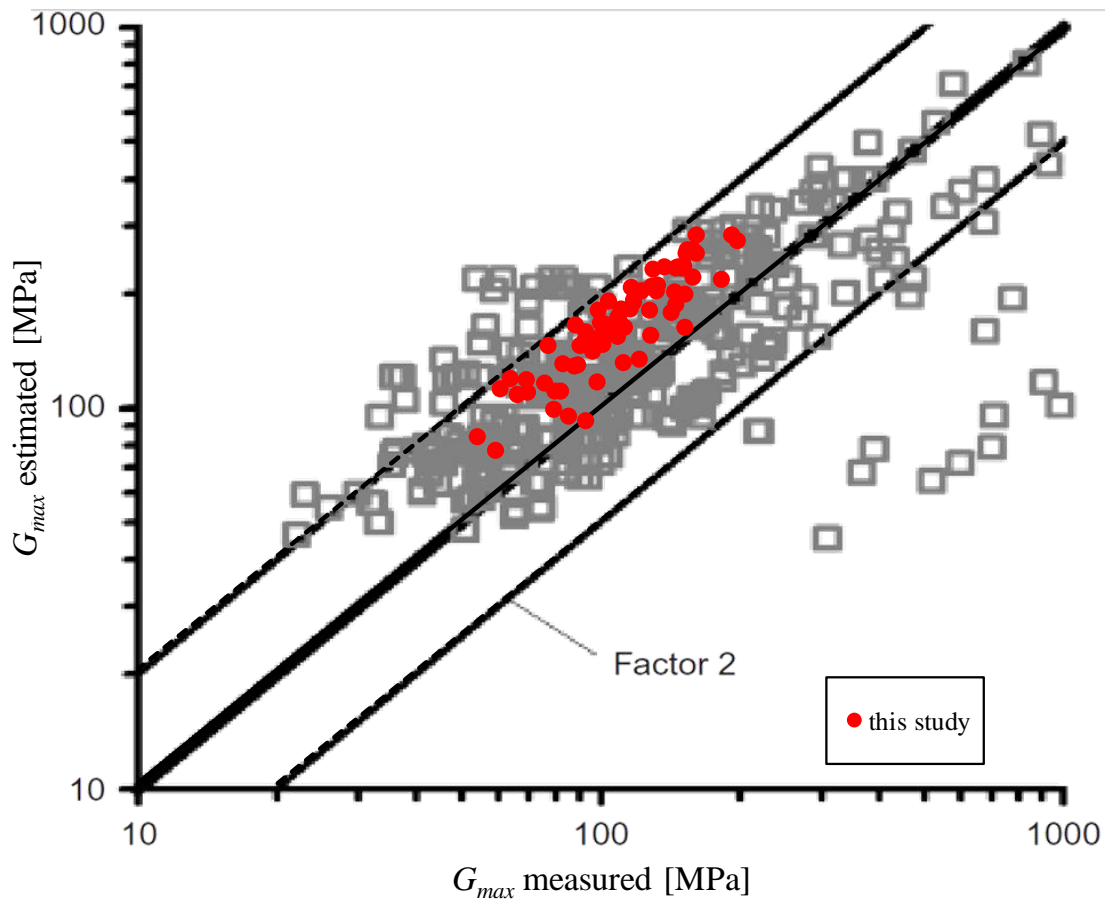


Figure 4-11 Measured vs. estimated G_{max} using the correlation given by (Oztoprak & Bolton, 2013). The range of 200% and 50% is given with solid lines

Measurements have been compared to an independent set of tests performed with BE at the Geotechnical Laboratory of the Slovak University of Technology in Bratislava by Jakub Panuska. Since a wide variety of void ratios and confining stresses were tested, comparison and interpretation of data were done by fitting one data set with factors accounting for void ratio and confining stress then comparing them to the direct results of the other test. So, RC tests were fit with parameters to allow shifts in void ratio and confining stress then compared to BE measured results. Likewise, BE tests were fit with similar equations and compared to RC measured results. Figure 4-12 shows the confinement levels and void ratios in the comparative study.

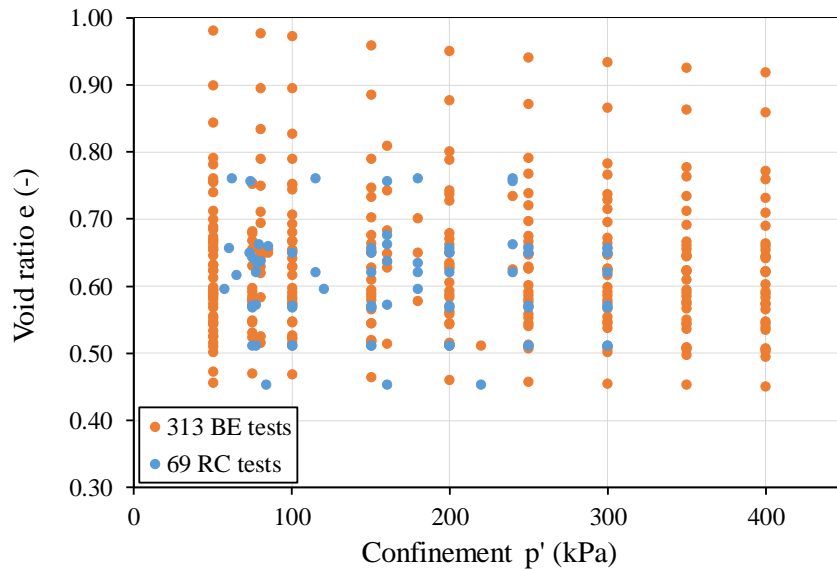


Figure 4-12 Confinement and void ratio conditions in the comparative study

Equations 2-22 and 2-23 were used for regression, and obtained fitted parameters A and n are listed in Table 4-5. Note, that in this comparison p' is not divided by the atmospheric pressure p_{atm} , hence the range of values of A and n are different than in the earlier correlations shown in Table 4-4. Results obtained with the two methods are shown in Figure 4-13. All of the measurement points for RC at different e and p' from the testing matrix were used.

Table 4-5 Obtained intrinsic parameters by RC and BE testing for all samples using Equation 2-22.

Sample	RC			BE		
	A	n	R^2	A	n	R^2
	[-]	[-]	[-]	[-]	[-]	[-]
P1	7.67	0.51	0.74	5.85	0.54	0.97
P2	3.51	0.60	0.96	3.81	0.55	0.99
P3	5.29	0.51	0.98	4.07	0.56	0.99
P4	6.49	0.50	0.99	3.18	0.63	0.99
P5	8.14	0.42	0.99	3.82	0.56	0.99
P6	7.36	0.45	0.97	4.34	0.58	0.98
P7	9.92	0.40	0.97	4.00	0.57	0.98
P8	-	-	-	5.15	0.58	0.99
B1	5.49	0.49	0.80	4.39	0.53	0.98
B1(gr)	-	-	-	3.77	0.57	0.96
B2	6.55	0.50	0.73	5.50	0.53	0.99

The agreement between measured results is generally very good. In the case of samples with high void ratios (loose samples) RC measured higher G_{max} than BE as a tendency. This may be due to the slight inaccuracy of the measurement of void ratio in the hollow cylinder RC samples or less complete coupling of the BE system in looser soils.

Similar comparisons between RC and BE has been made in many researches, results gathered from the literature are plotted in Figure 4-14. Results from different authors fit into a close range of $\pm 15\%$ from exact agreement similarly to this study. Coordinated BE testing and comparison with equations proposed in (Iwasaki & Tatsuoka, 1977) based on RC testing for Toyoura sand also showed a $\pm 15\%$ difference between BE and RC tests even though there were different evaluation procedures for BE tests.

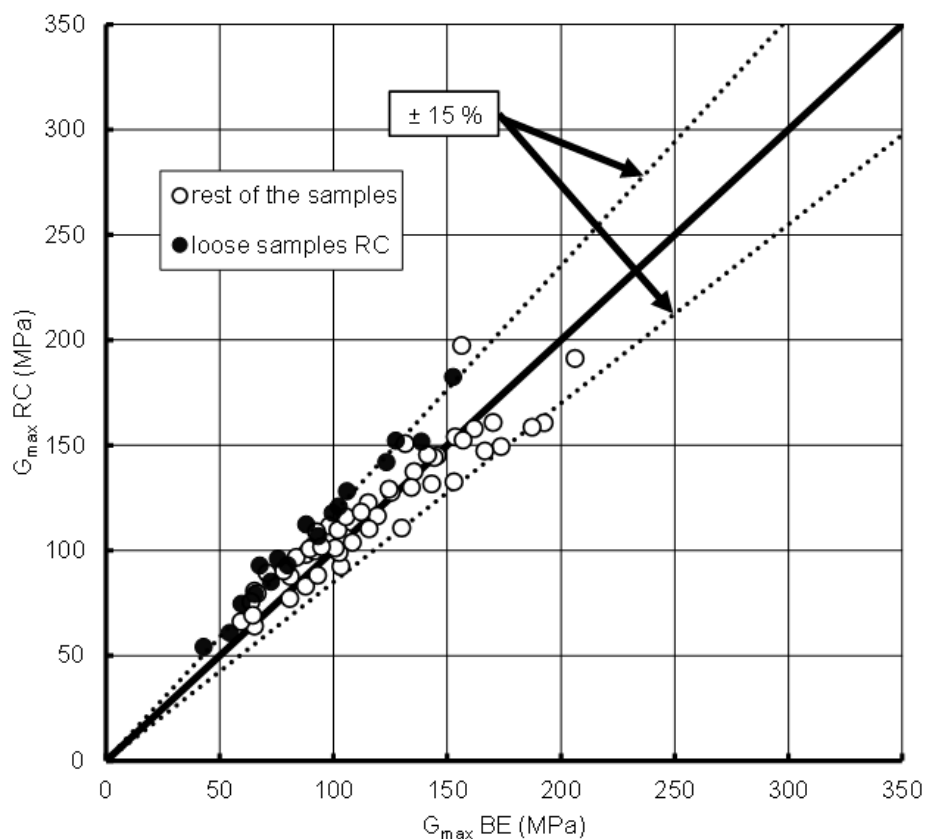


Figure 4-13 Comparison of G_{max} measured with BE and RC in this study

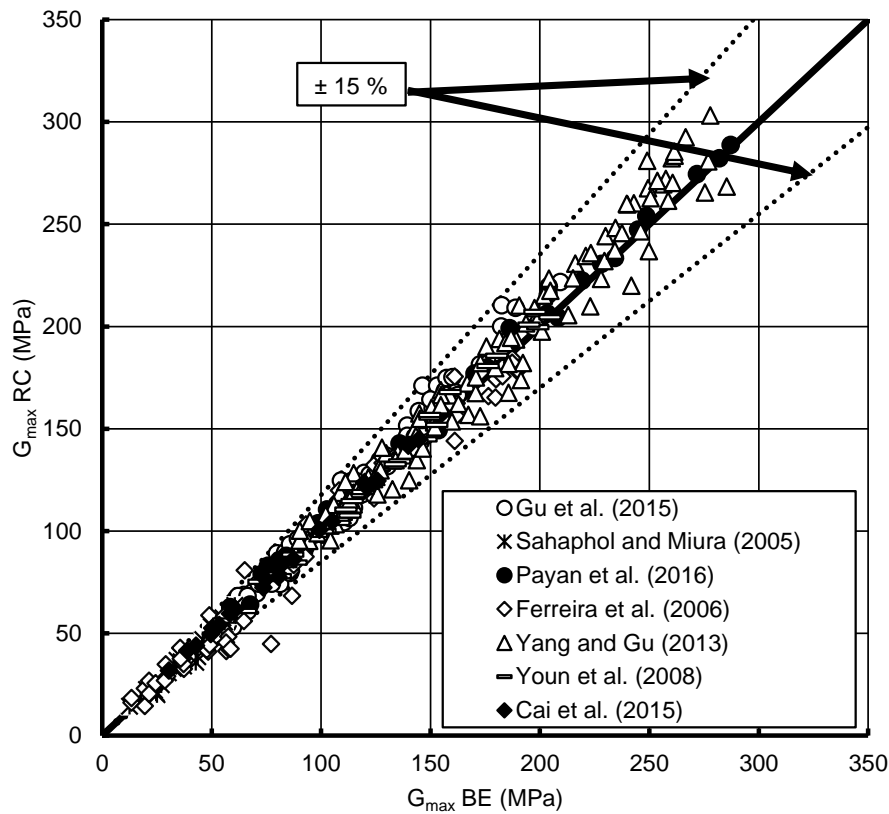


Figure 4-14 Comparison of G_{max} measured with BE and RC in literature

4.3 Modulus reduction curves

Modulus reduction curves for each sample are shown in the following figures continuously. For TOSS tests, cycle 100 is shown, except for some cases, where stated otherwise (cy10 in the legend means cycle 10 is shown). For each soil the first figure shows the reduction curve in a G/G_{max} vs. γ/γ_{ref} plot. Equations 2-15 – 2-17 were used and a fit has been obtained by regression with minimizing the sum of residual squares using MS Excel’s Solver with the GRG method (Generalized Reduced Gradient). The fitted Ramberg-Osgood (RO) model parameters, α , C , R are shown in the legend in the top right corner together with the coefficient of determination R^2 which provides a measure of how well the observed outcomes are replicated by the model. The legend in the bottom right corner shows the identification number of each Resonant Column (RC) and Torsional Shear (TOSS) test in brackets. The second figure shows the measurement results in a G/G_{max} vs. γ plot which allows for comparison with the most commonly used references in the literature, given by (Oztoprak & Bolton, 2013), (Vucetic & Dobry, 1991) and (Wichtmann & Triantafyllidis, 2013). Equations 2-37 and 2-40 – 2-42 were used from the former paper to calculate a degradation curve for each soil based on grain size characteristics; this is given with a dashed line named “Oztoprak&Bolton fit” (OB fit). It has to be noted, that this

fit and the curve given by (Wichtmann & Triantafyllidis, 2013) (denoted as W curve) are usually only valid for one set of measurements in the graph, since p' is used in them and confinement was not the same for all tests. Beside this the “mean” curve given in Equation 2-37 is also shown as “Oztoprak&Bolton mean” (denoted OB mean). This curve was obtained as the best fit for a large number of test results by the authors. The curves for soils with a $PI=0\%$, 15% and 30% (denoted VD0, VD15, VD30) are also presented from (Vucetic & Dobry, 1991), since the $PI=0\%$ curve suggested for sands did not fit the data well.

It should be noted, that the RO fit curve, which is obtained in the G/G_{max} vs. γ/γ_{ref} plot, cannot be plotted as a single curve in G/G_{max} vs. γ plot, because γ_{ref} is different for each confinement and void ratio. Similarly, the curves from literature cannot be compared to the RO fit directly, because the VD curves are only given as single data points in the G/G_{max} vs. γ plot and γ_{ref} is unknown for them, which is also the case for the OB curves. Therefore, separate comparisons are made to show the best fit, which is usually obtained by the RO fit and the applicability of the curves from literature.

For Sample P1 RC and TOSS measurements gave very similar results in the range of strains where both were applicable. Results from the separate tests also fall on a close range of a single degradation curve in Figure 4-15. The RO fit shows a good estimation of measured values with $R^2=0.94$. The OB fit curve over-predicts the effect of degradation and shows approx. 20% lower values of G/G_{max} than the measured ones. The OB mean curve is in quite good agreement with measured data; estimated values are only 5-10% lower than measured ones. The W curve is probably the best fit out of these correlations from literature, while VD15 is also an acceptable fit.

The measured points of the degradation curve showed a larger scatter for Sample P2, see Figure 4-17. Very low strain ($\gamma/\gamma_{ref}<0.1$) TOSS measurement results show 10-20% lower values of G_{max} than RC. This strain level is probably the limit of accuracy for the TOSS tests due to the precision of the proximitors used. These measurement points were excluded for the RO fit procedure and a good fit was achieved with $R^2=0.91$. This problem does not appear with the RC tests, since strain is measured with the accelerometer in RC tests. However, overall agreement between RC and TOSS for higher strains ($\gamma/\gamma_{ref}>0.1$) is satisfactory. The OB fit curve does not follow measured data; 35-40% lower values of G/G_{max} are predicted by it than the measured ones. Generally, the reduction of G_{max} is not as pronounced as for Sample P1; while the OB mean curve and W curve are closer to measurement trend, VD30 is the best fit for Sample P2.

A similar trend can be observed for Sample P3 as described for P2. Three very low strain measurement points were excluded here as well, but otherwise the RO fit is excellent, with an $R^2=0.97$, see Figure 4-19. Once again, the scatter in the G/G_{max} vs. γ plot in Figure 4-20 is slightly higher. The OB fit curve shows a too strong reduction, OB mean and W curves are closer to the measured data, while the bigger scatter means that measured points lay between the VD0 and VD30 curves, with the VD15 being a good fit for them.

Measured points for Sample P4 show the largest scatter, with an $R^2=0.89$ fit of the RO model. Agreement between RC and TOSS is acceptable; see Figure 4-21, although not as good as for the other samples. The OB fit coincides with VD0 curve which are both a lower bound of measured data, while upper bound would be the VD30 curve, with VD15 being a quite good fit and the OB mean the best fit for Sample P4 out of these curves from literature. The W curve shows a very significant reduction, which is not following measured trends. This correlation takes the effect of uniformity coefficient on G/G_{max} into account, but for samples with a $C_U > 3$ (P4, P7 and B1) the effect is significantly over predicted.

For Samples P5 and P6 a lower number of measured data points were available, because the testing equipment malfunctioned during TOSS tests No. (24) and (25). Unfortunately, this became only clear after performing the test, during post-processing of data. Meanwhile RC measurements are shown from these tests, since they were expected not to be affected by the error. Degradation curve obtained for P5 is fitted with a RO curve with $R^2=0.93$, see Figure 4-23. Due to the lower number of data points at higher strains, correlations from the literature are difficult to assess; but once again a curve between VD15 and VD30 would be a fair estimate and W curve is also acceptable. For P6 the RO fit is very good, with $R^2=0.97$, see Figure 4-25. From the literature here again, OB mean and W curve could be considered to be the best fits for P6.

The degradation curve for Sample P7 is shown in Figure 4-27 and Figure 4-28. Agreement between RC and TOSS for a single test is excellent, while the scatter between tests with different confinements is somewhat larger. The normalization used for Figure 4-27 brings the measured points only slightly closer this time and a RO fit could be found with $R^2=0.93$. Some measured points lay even above the VD30 curve and while the OB mean and OB fit curves lay on each other, none of them are a good fit, a curve between VD15 and VD30 would be the best fit. The W curve once again shows a more significant degradation which does not follow measured behavior, note that C_U was higher than 3 for this sample.

Results for Sample B1 again show the benefits of using the normalized plots; see Figure 4-29 and Figure 4-30. Once again, the RO fit is exceptionally good with $R^2=0.98$ if the very

low strain TOSS measurements are excluded. The trend for the curves are similar as before: OB fit show a too significant degradation, OB mean can be considered a lower bound for measured data, while most of the data are between the VD15 and VD30 curves. The W curve is again far from measured data as with the previous sample.

Similar general observations can be made about Sample B2, except the W curve is much closer to measured values. The RO fit is very good with $R^2=0.96$ and most data points are between the VD15 and VD30 curves while other curves show a too significant degradation.

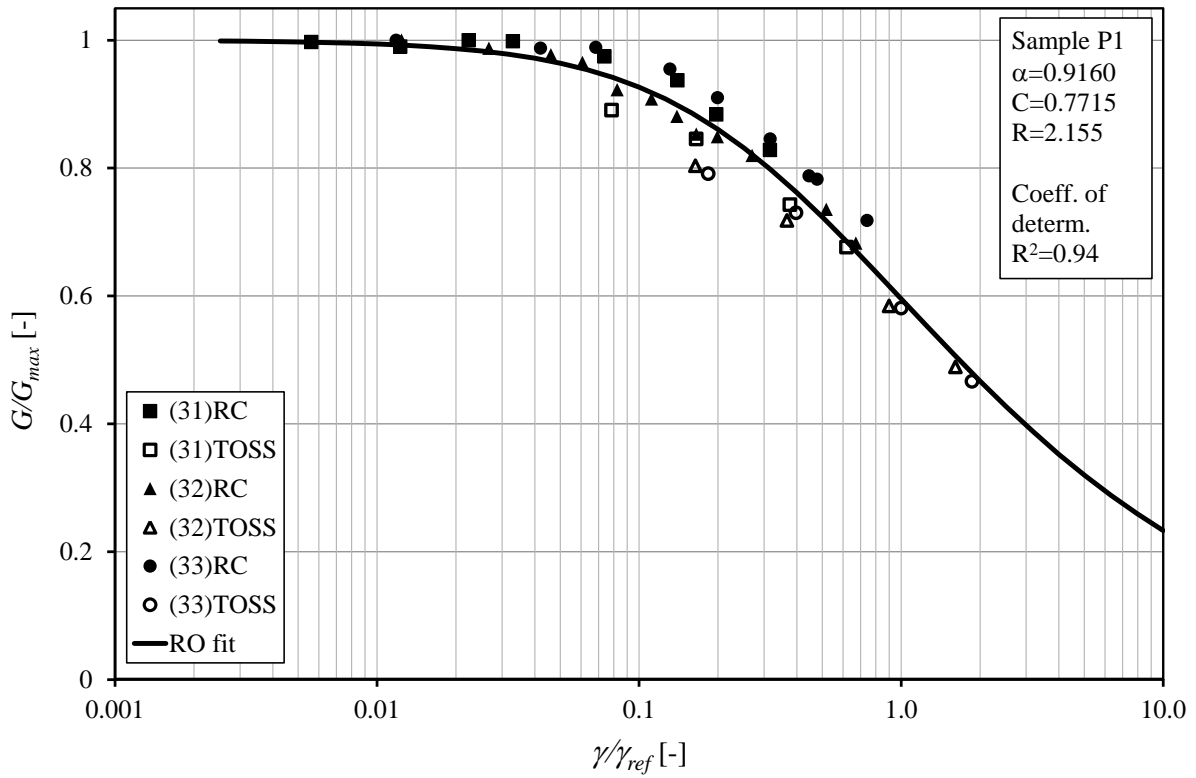


Figure 4-15 Modulus reduction curve for Sample P1 with RO fit

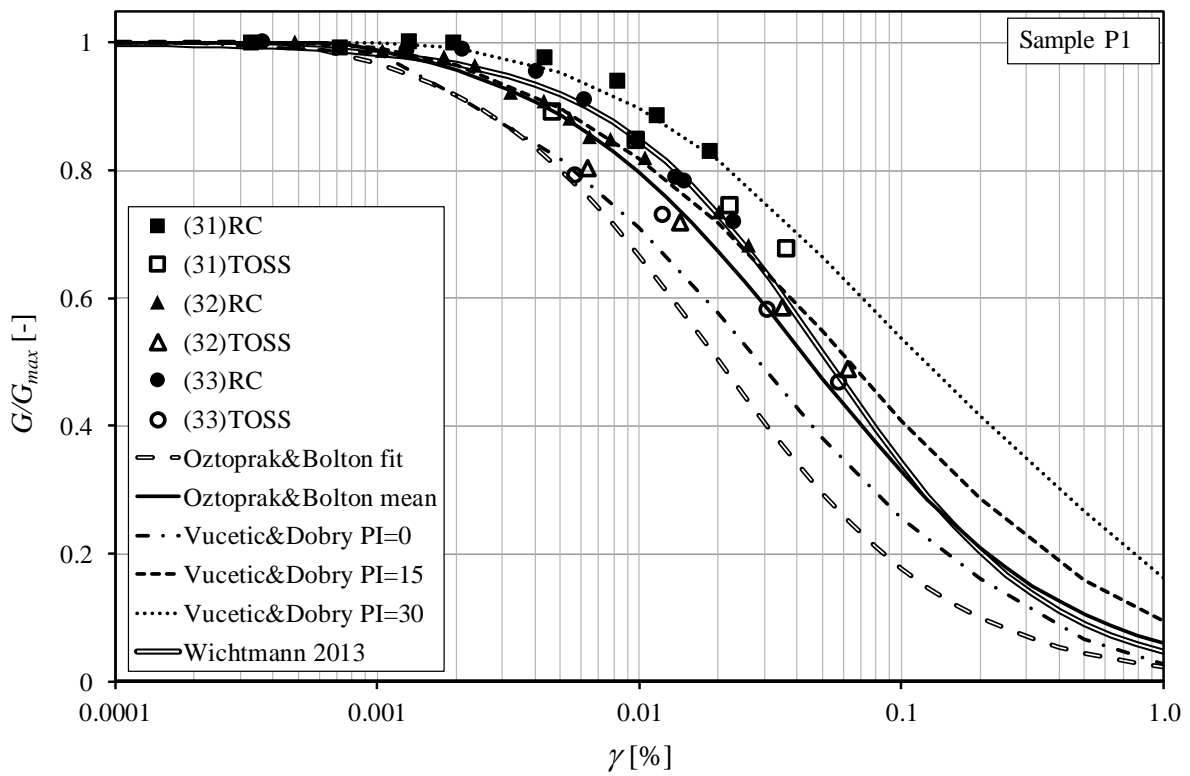


Figure 4-16 Modulus reduction compared to correlations for Sample P1

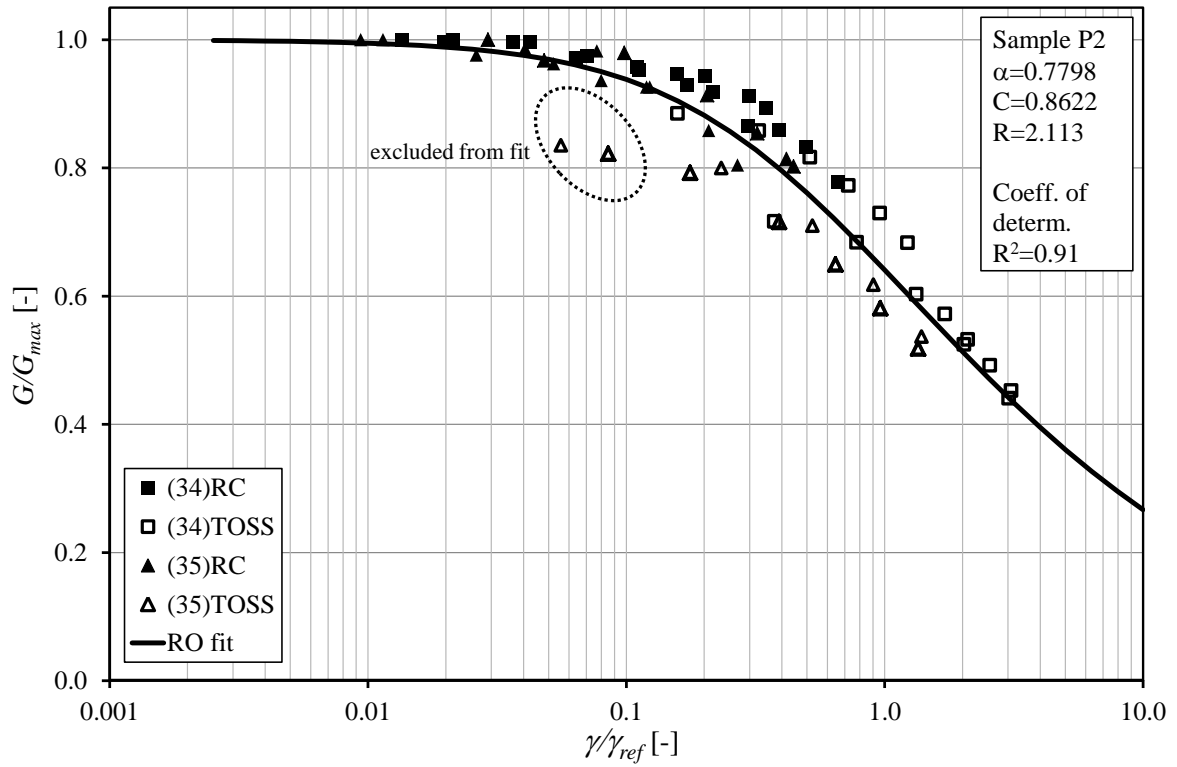


Figure 4-17 Modulus reduction curve for Sample P2 with RO fit

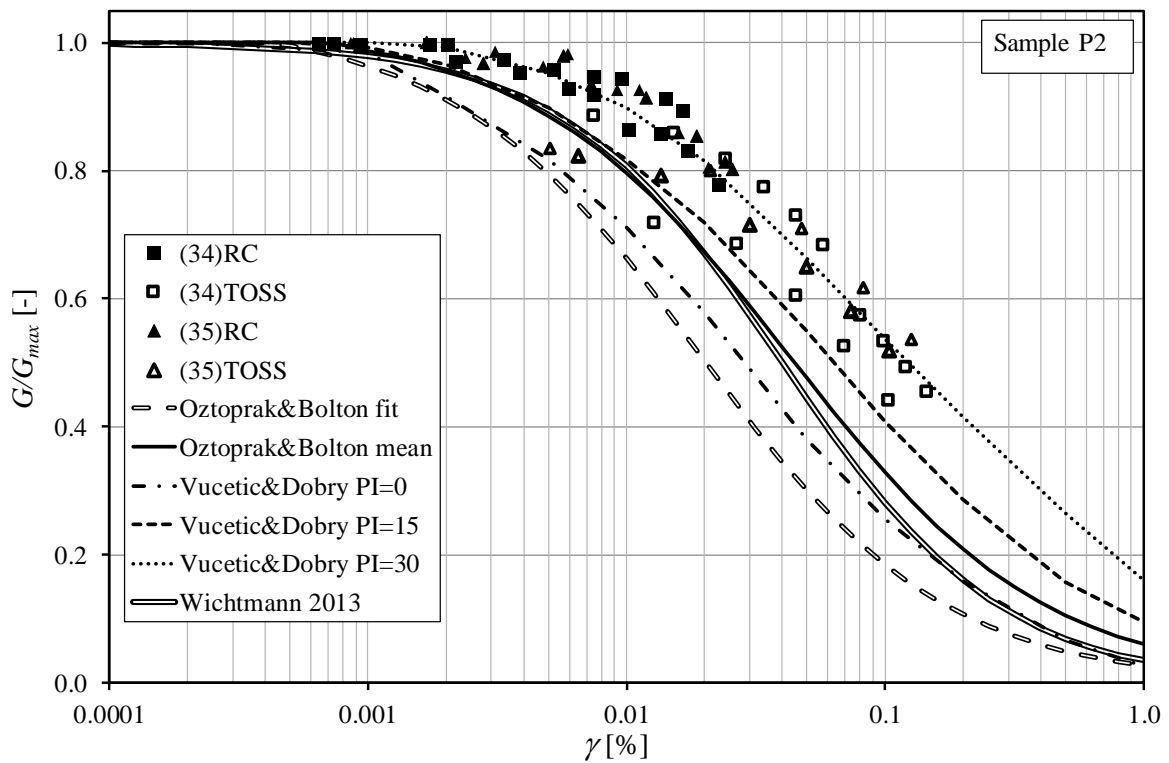


Figure 4-18 Modulus reduction compared to correlations for Sample P2

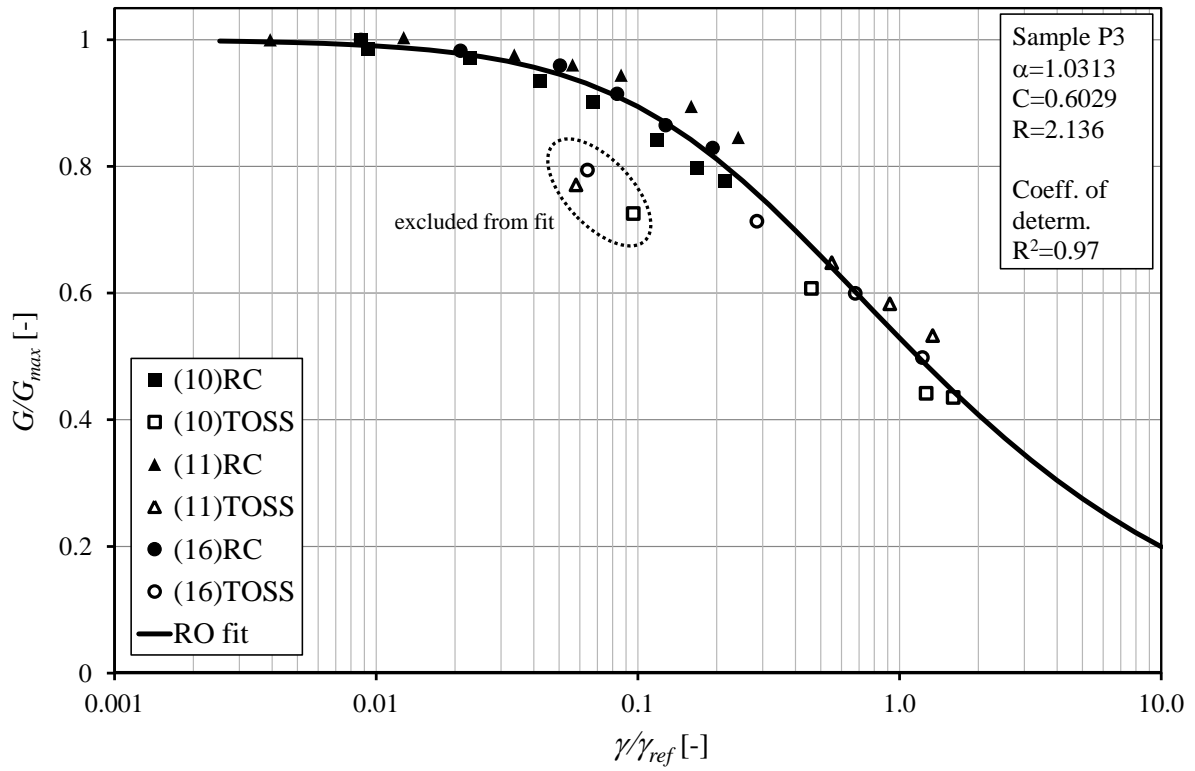


Figure 4-19 Modulus reduction curve for Sample P3 with RO fit

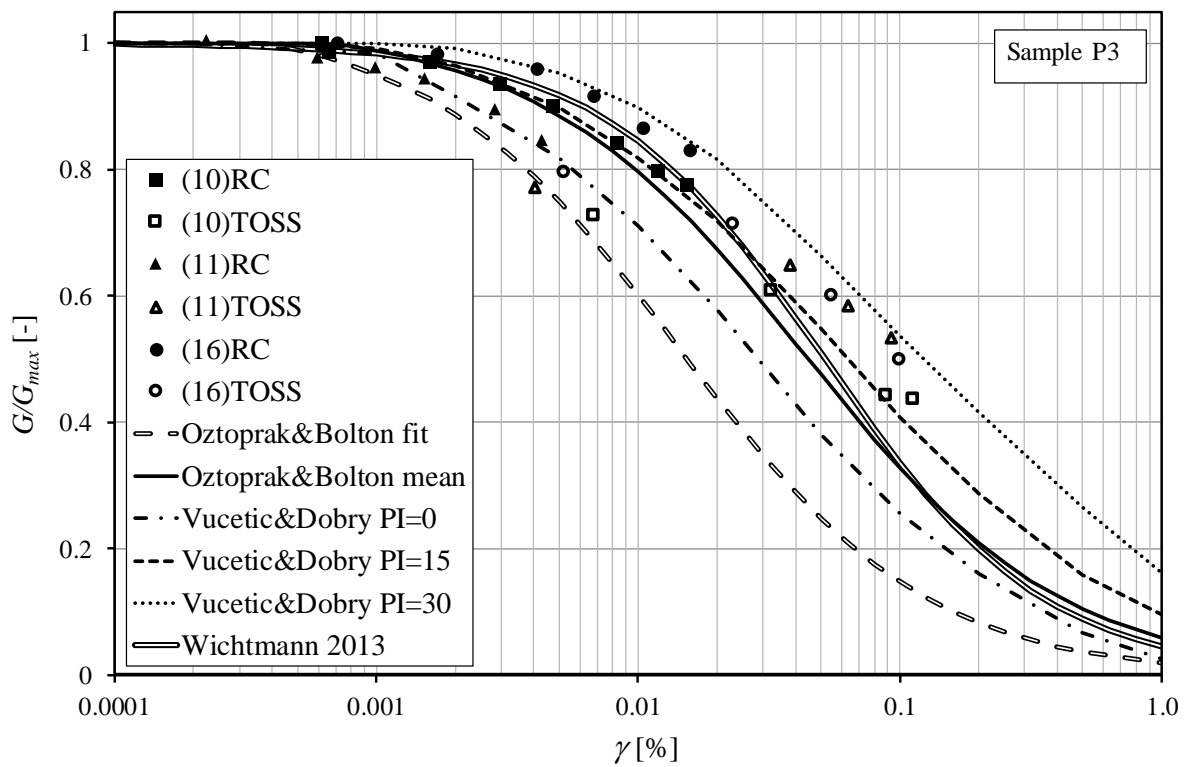


Figure 4-20 Modulus reduction compared to correlations for Sample P3

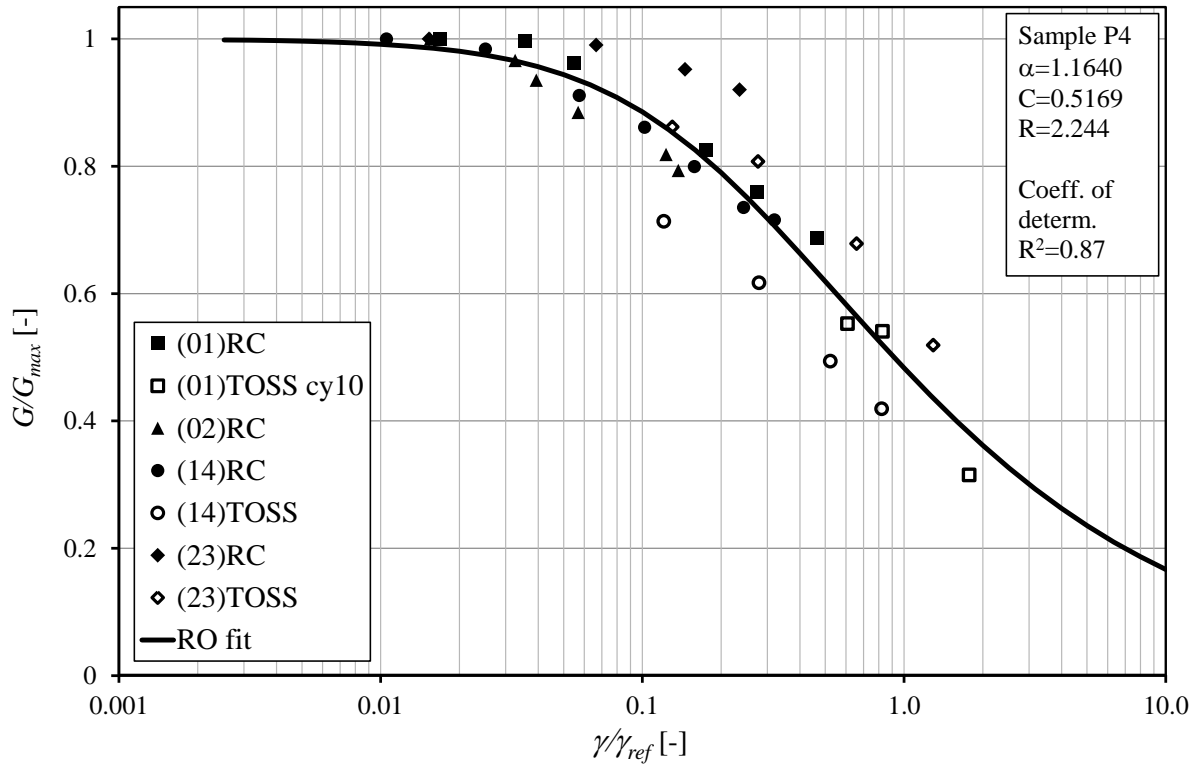


Figure 4-21 Modulus reduction curve for Sample P4 with RO fit

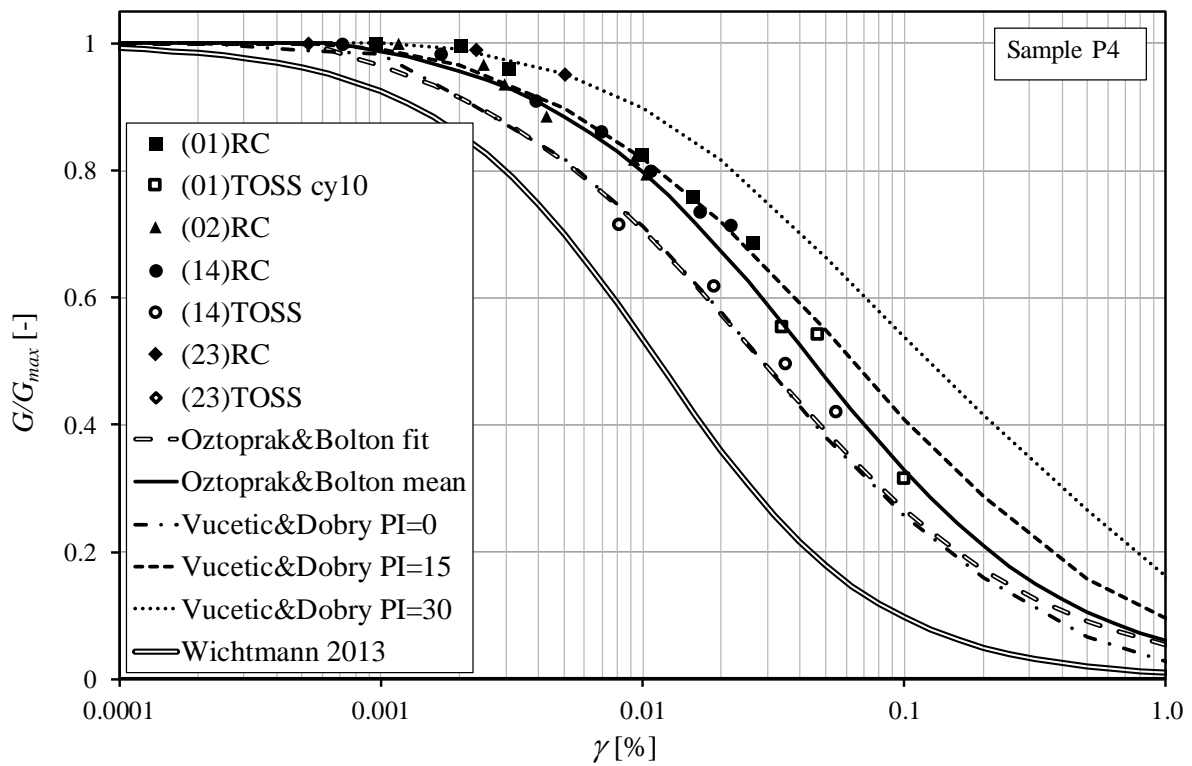


Figure 4-22 Modulus reduction compared to correlations for Sample P4

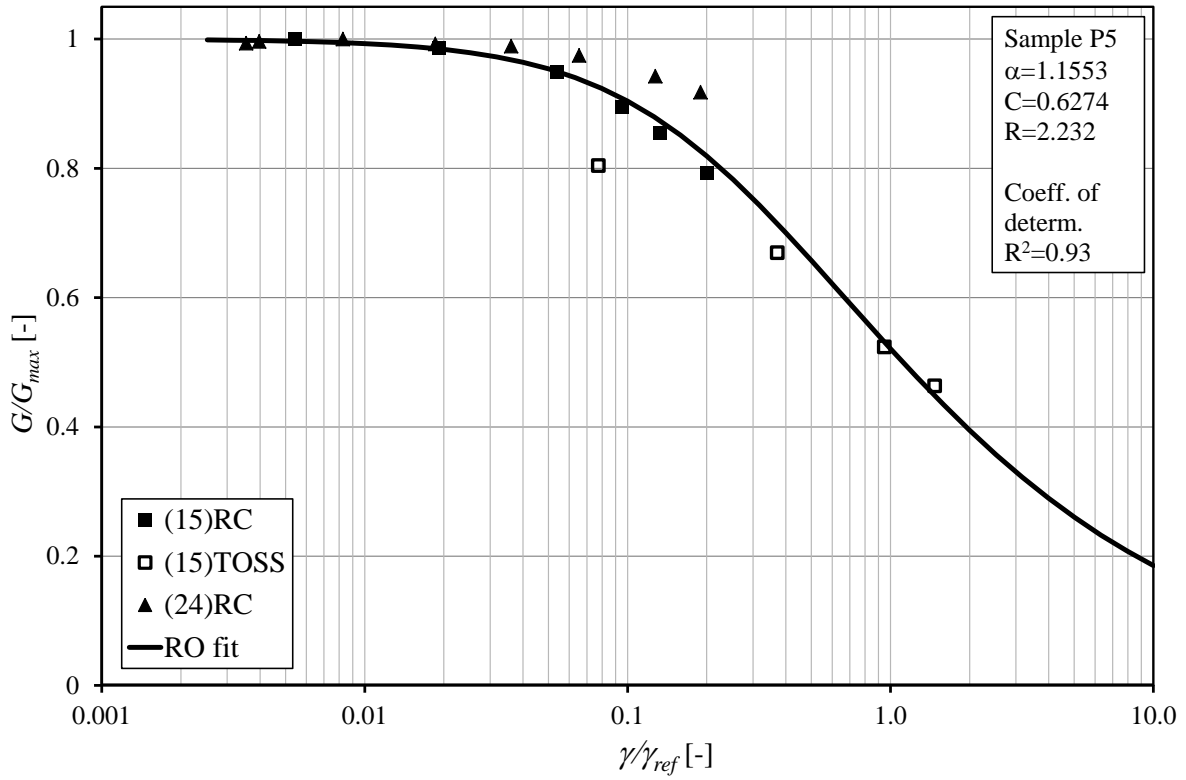


Figure 4-23 Modulus reduction curve for Sample P5 with RO fit

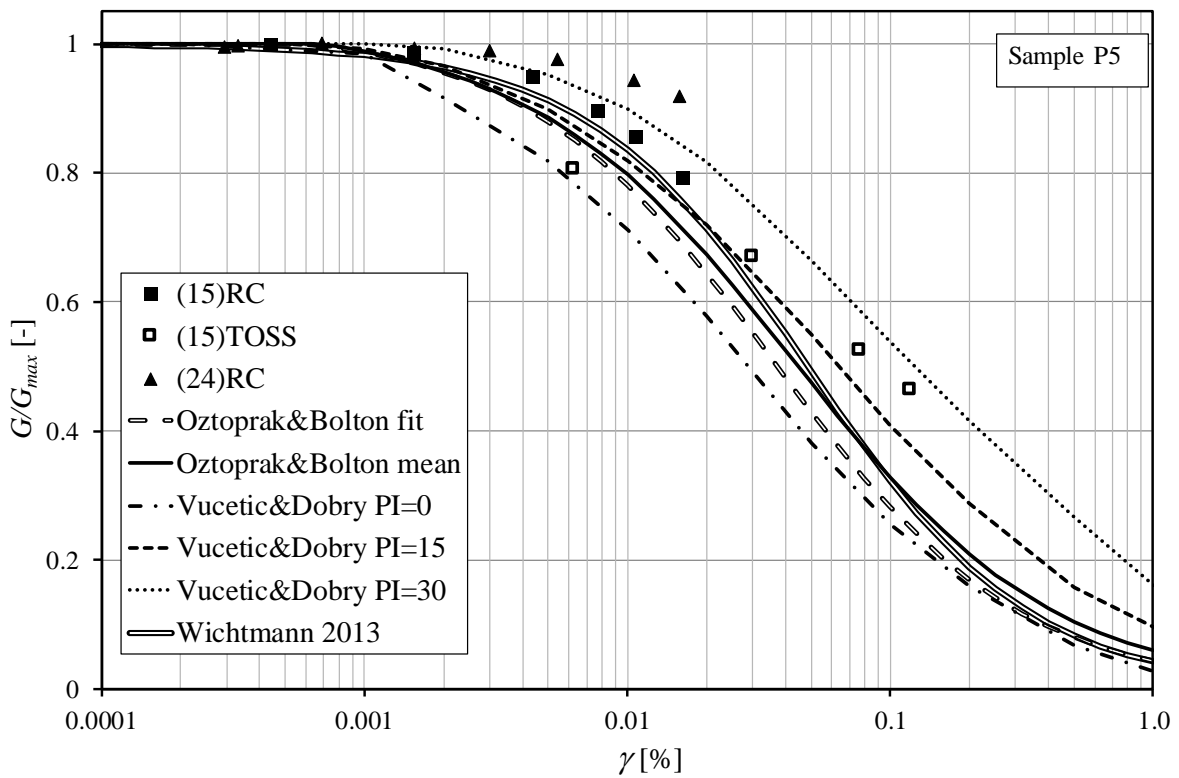


Figure 4-24 Modulus reduction compared to correlations for Sample P5

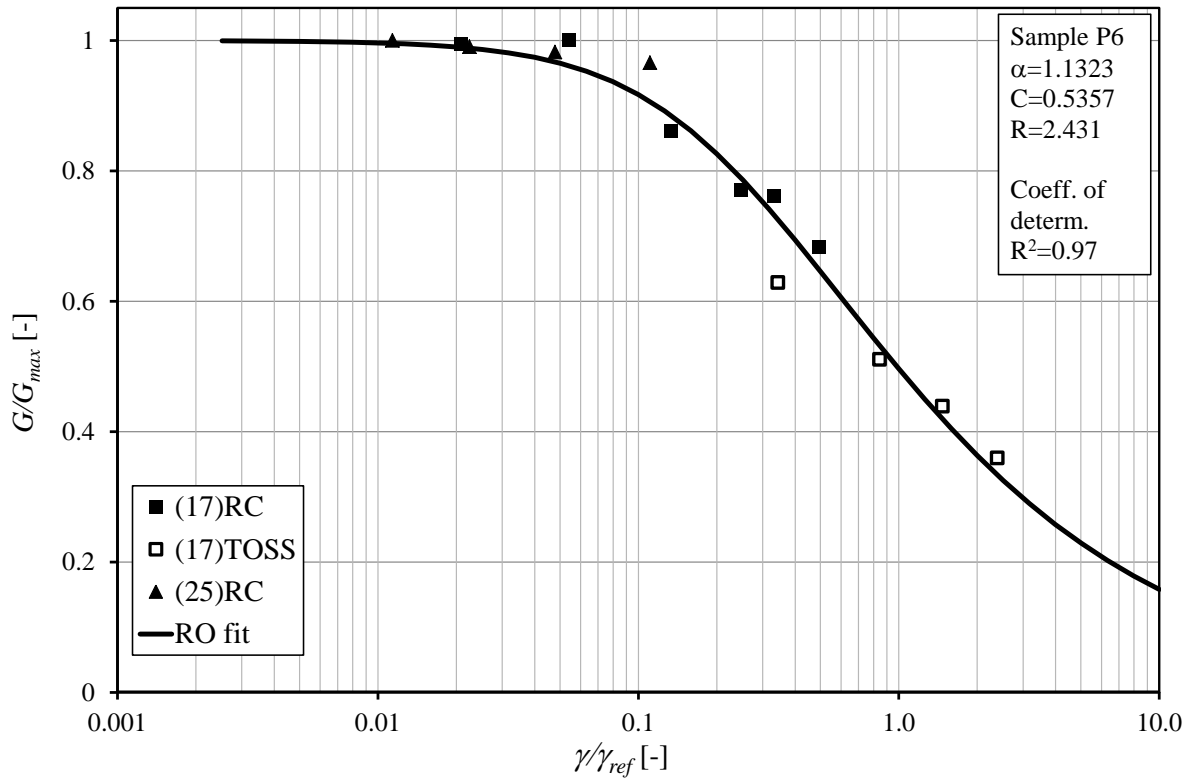


Figure 4-25 Modulus reduction curve for Sample P6 with RO fit

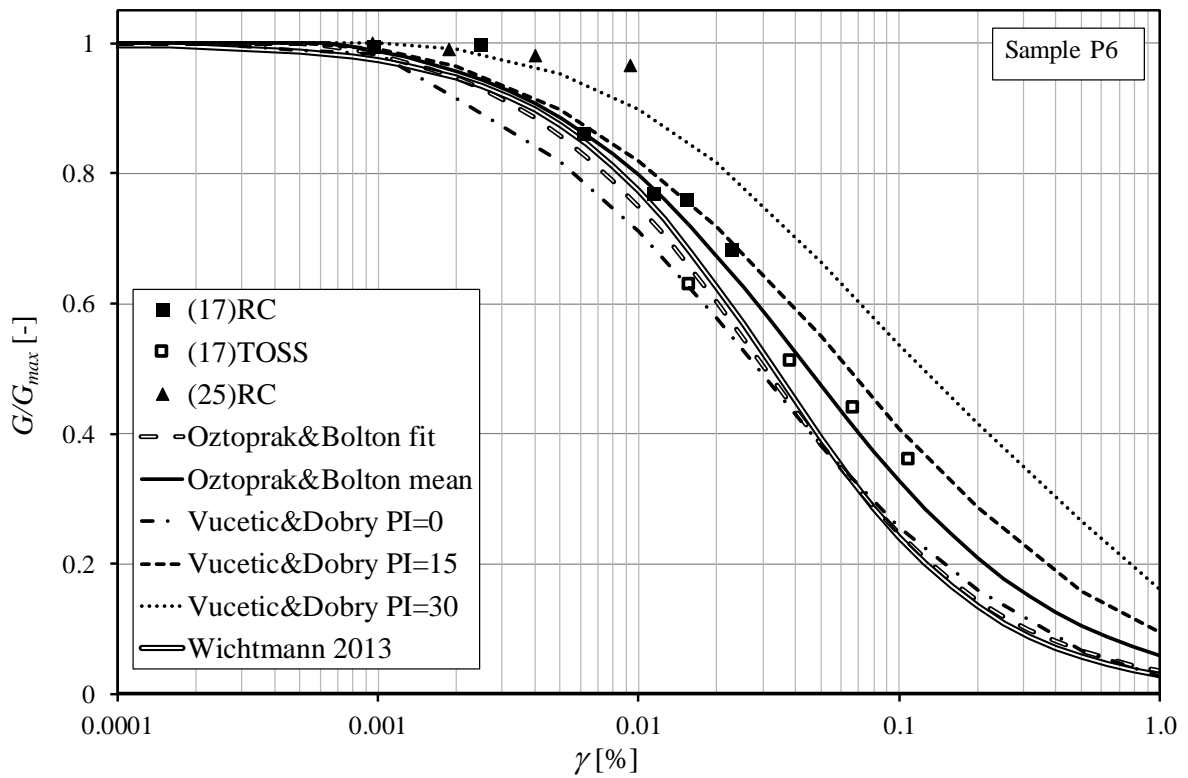


Figure 4-26 Modulus reduction compared to correlations for Sample P6

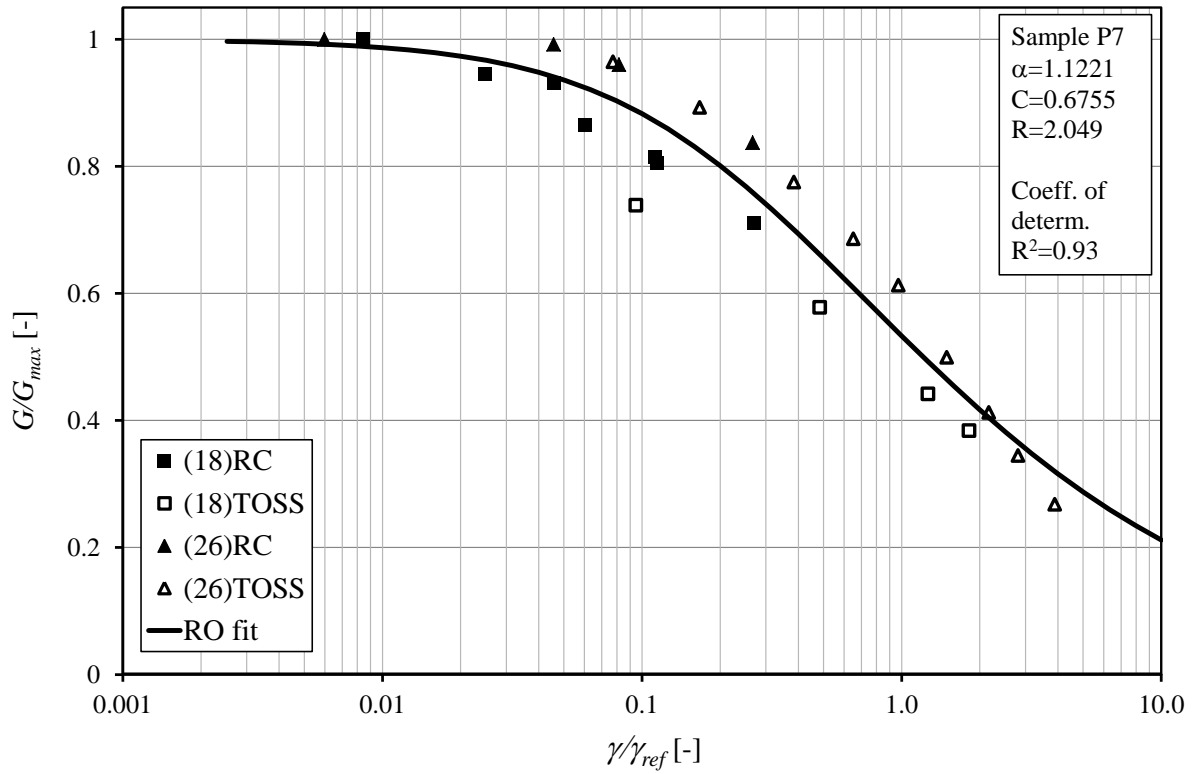


Figure 4-27 Modulus reduction curve for Sample P7 with RO fit

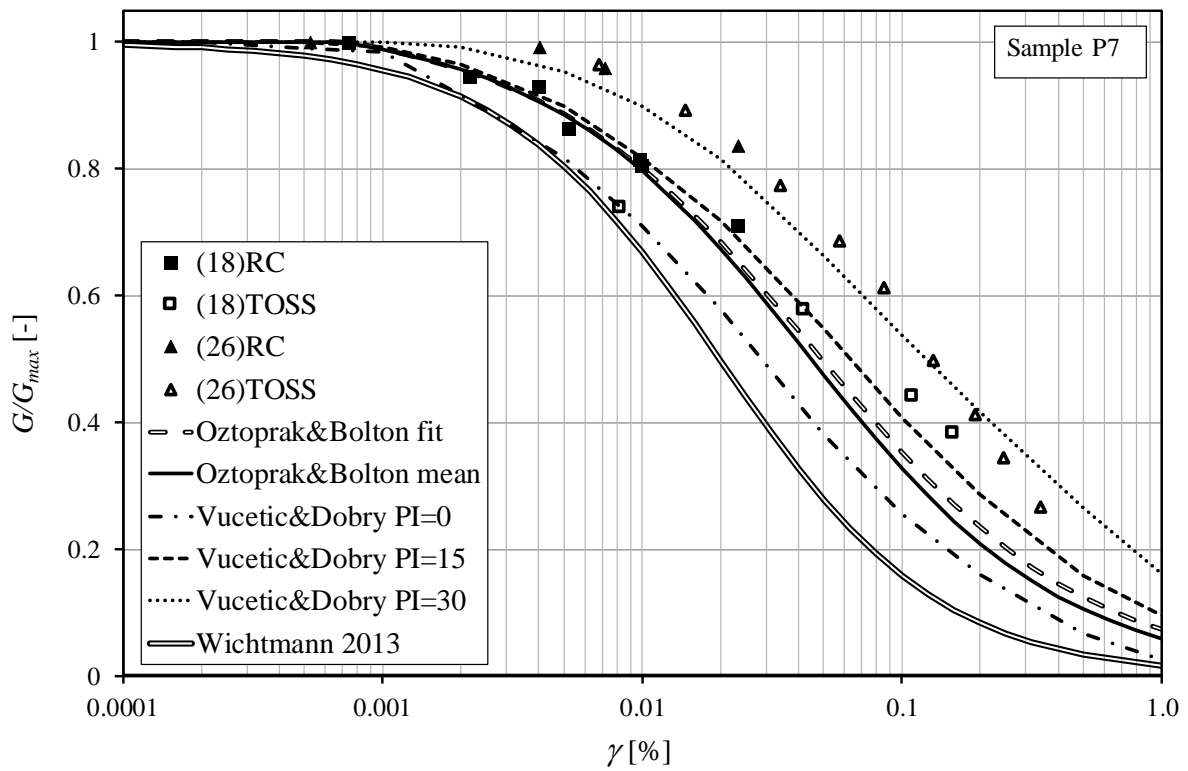


Figure 4-28 Modulus reduction compared to correlations for Sample P7

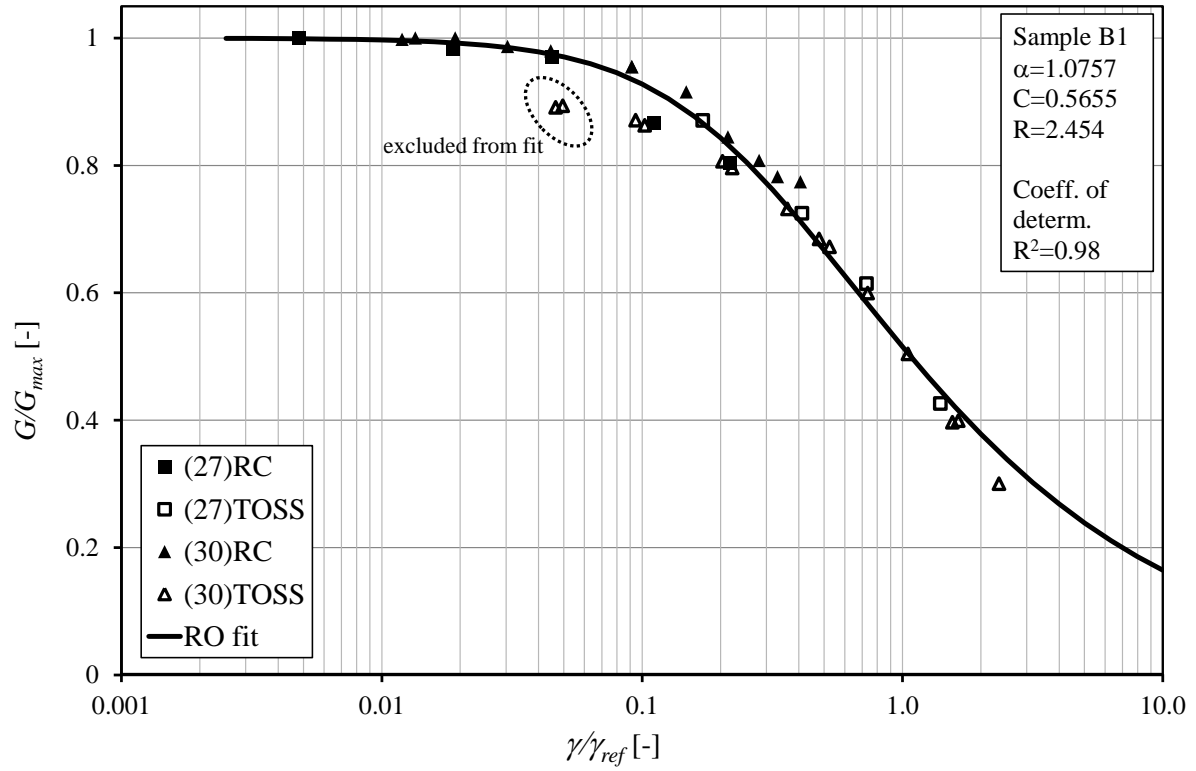


Figure 4-29 Modulus reduction curve for Sample B1 with RO fit

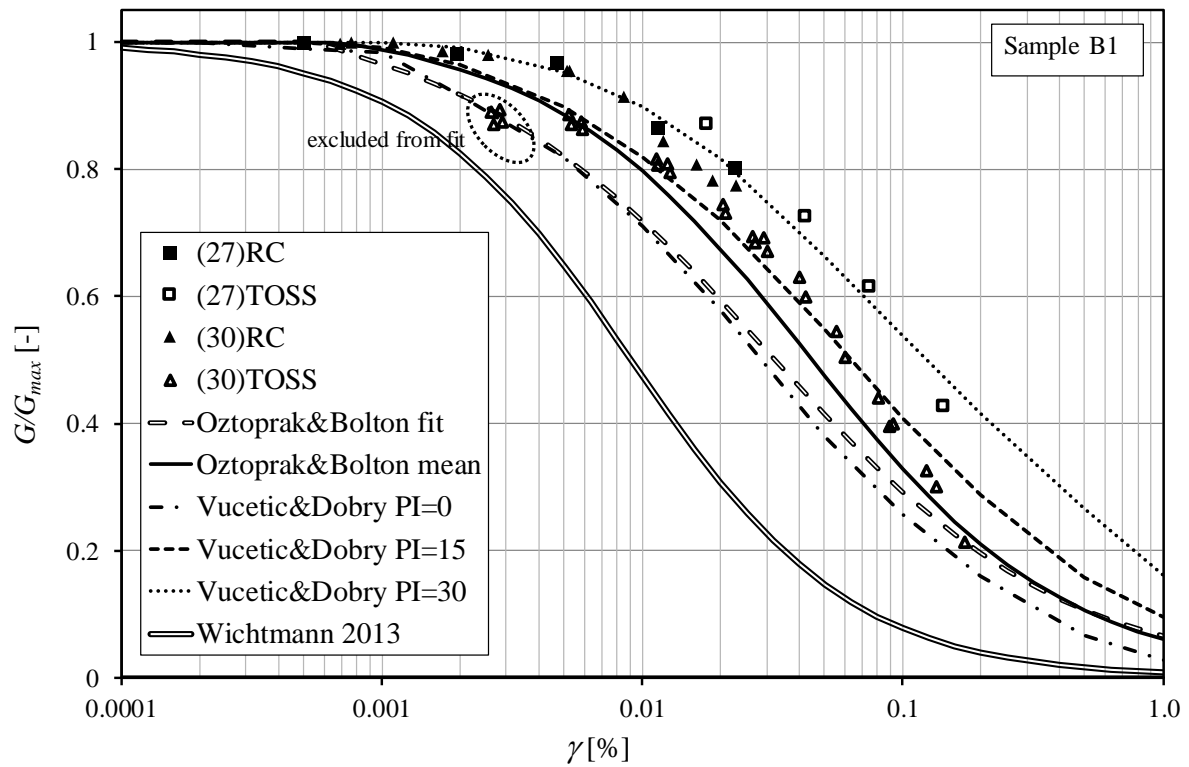


Figure 4-30 Modulus reduction compared to correlations for Sample B1

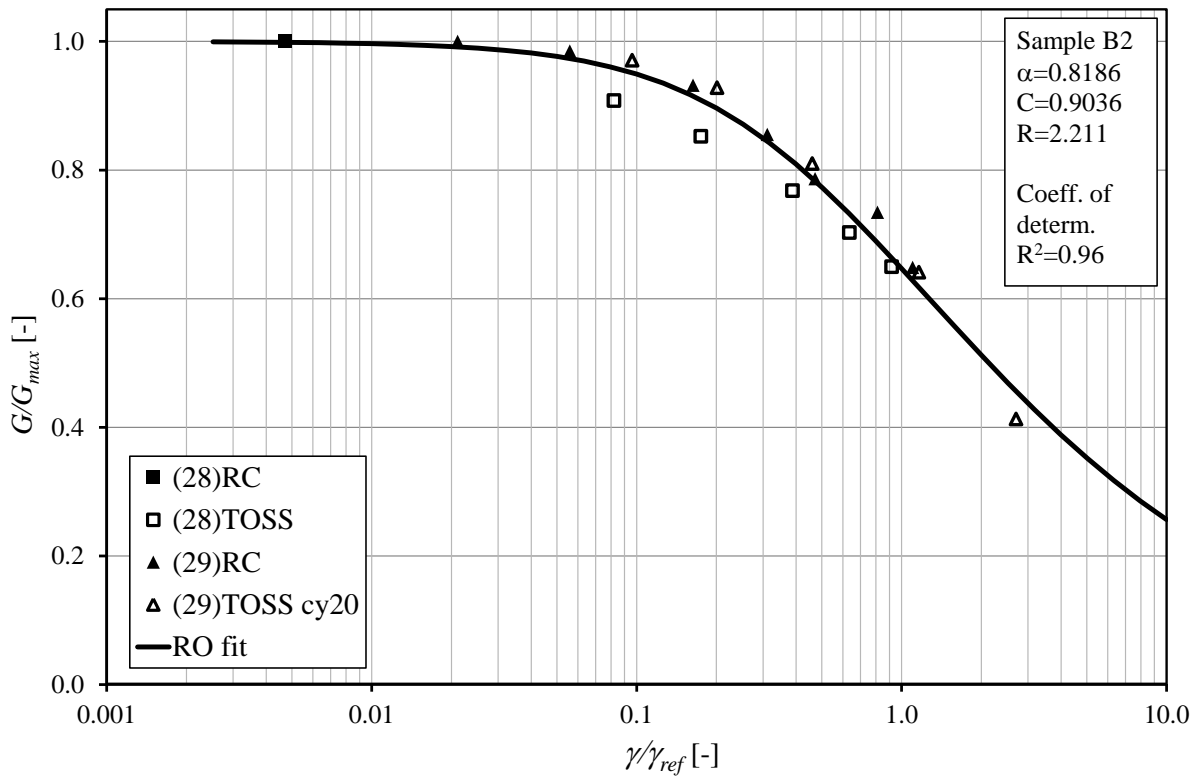


Figure 4-31 Modulus reduction curve for Sample B2 with RO fit

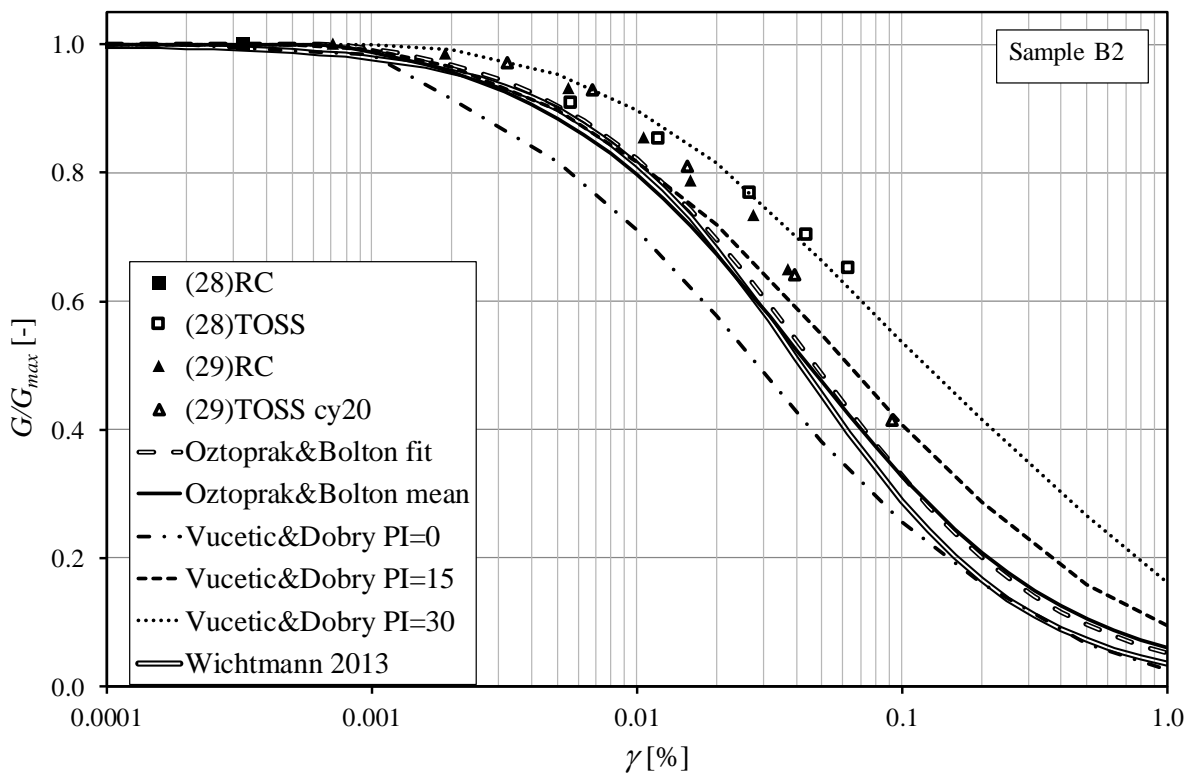


Figure 4-32 Modulus reduction compared to correlations for Sample B2

All 279 measured points of G/G_{max} for all soils are shown in a single plot in Figure 4-33 with a RO fit for all points. The scatter of the points is significant, but a similar range was found in many tests shown in (Oztoprak & Bolton, 2013), see Figure 2-20. At a given strain the scatter is around $\pm 15\%$ in G/G_{max} value. However, the single RO fit for all soils is satisfactory with $R^2=0.89$.

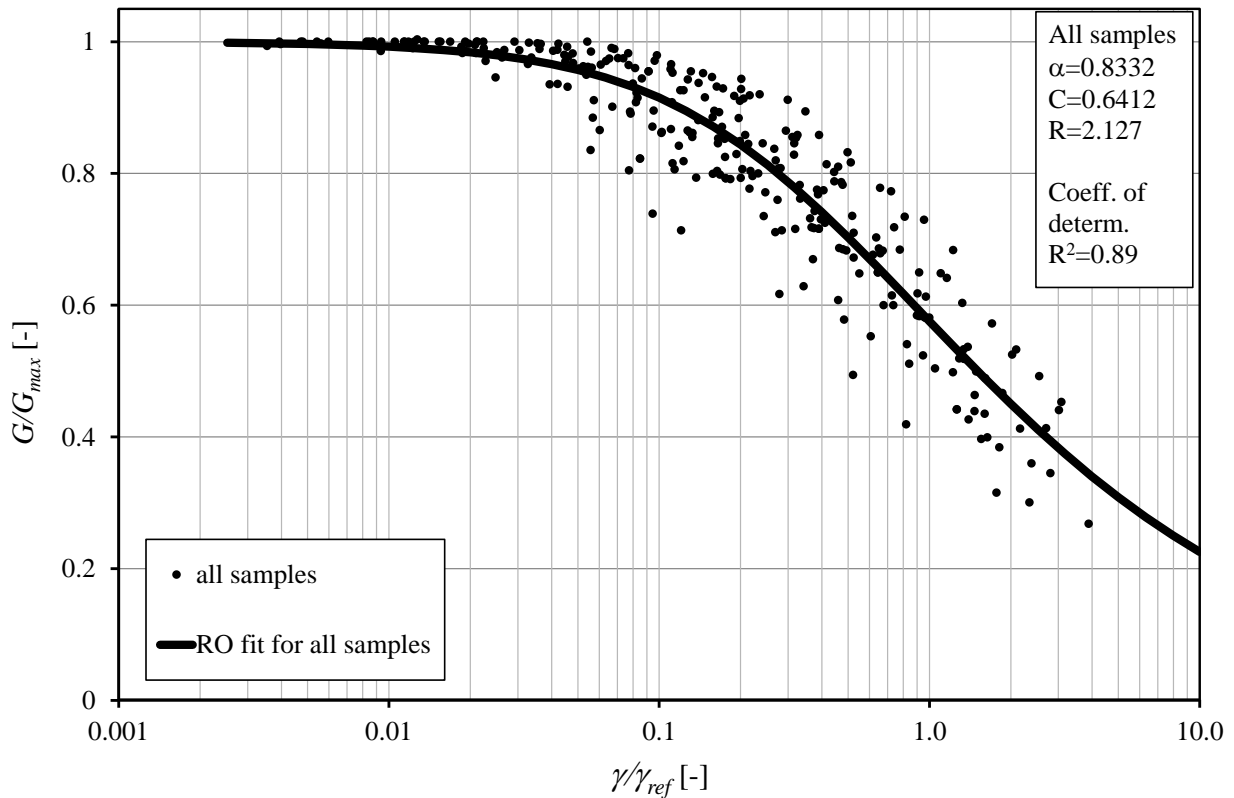


Figure 4-33 Modulus reduction curve for all samples with RO fit

The parameters of the obtained RO fits and the coefficient of determination are summarized in Table 4-4 and all curves are plotted together in Figure 4-34.

Table 4-6 Obtained Ramberg-Osgood material model parameters for all tested soils

Sample ID	Mean particle diameter	Uniformity coefficient	Fines content	RO parameters			Coefficient of determination
	d_{50} [mm]	C_u [-]	FC [%]	α [-]	C [-]	R [-]	R^2 [-]
P1	0.243	2.18	5.69	0.9160	0.7715	2.155	0.94
P2	0.424	2.38	1.32	0.7798	0.8622	2.113	0.91
P3	0.365	2.74	0.25	1.0313	0.6029	2.136	0.97
P4	0.179	20.7	16.75	1.1640	0.5169	2.244	0.87
P5	0.322	2.50	3.26	1.1553	0.6274	2.232	0.93
P6	0.211	2.06	7.56	1.1323	0.5357	2.431	0.97
P7	0.107	9.85	21.11	1.1221	0.6755	2.049	0.93
B1	0.191	30.86	18.84	1.0757	0.5655	2.454	0.98
B2	0.218	2.17	3.05	0.8186	0.9036	2.211	0.96
Fit for all soils	-	-	-	0.8334	0.6386	2.142	0.89

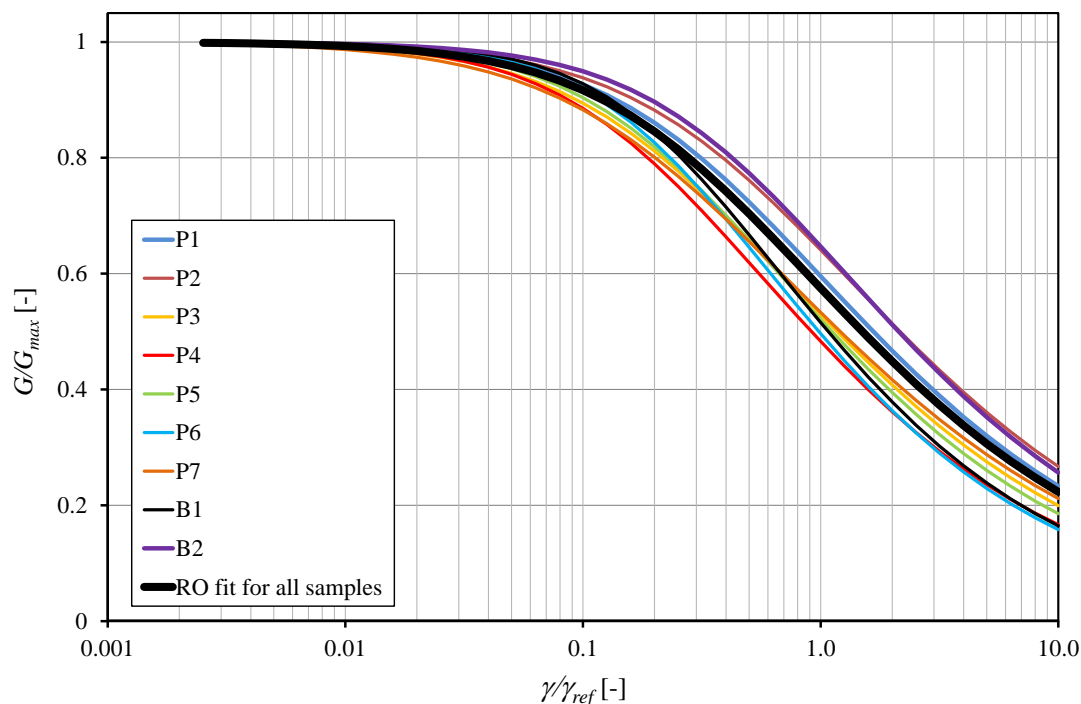


Figure 4-34 RO curves for each soil and the fit for all soils

No significant dependence of the degradation curve on grain size characteristics can be identified from Figure 4-34, which is perhaps because the curves are fairly close to each other

and the scatter in the measurements for a single soil could result in this slight scatter of the degradation curves. This narrow band of degradation curves suggests that the fit obtained for all samples can be considered to be applicable to typical Danube sands.

4.4 Damping curves

The following figures show measured damping values for each soil. Damping was measured in RC testing with the log decrement method and in TOSS testing as hysteretic damping as discussed earlier. It should be noted, that damping values from TOSS tests shown here are calculated from the hysteresis loop of cycle 100. It has to be noted also, that there is a difference between the RC damping obtained by the log decrement method and hysteretic damping obtained by TOSS. While hysteresis loops obtained by TOSS are symmetrical, strain level is clear, in RC the free decay results in a continuously collapsing hysteresis, and hence the strain level is continuously decreasing. For TOSS testing the effect of cycle number has to be considered. If the response in TOSS test changes during cycles, it is suggested to take a hysteresis loop for assessment, where the response corresponds to a “steady state” and not the first couple of cycles. These two effects result in an inherent uncertainty when comparing results of both methods adding to the difficulty of measurement. The scatter in damping is therefore usually bigger than in the modulus degradation. This is found in literature too. While the uncertainty of measurements is not reassuring, it has to be noted, that the effect of damping on practical calculations such as ground response analysis is minor compared to modulus reduction and a scatter of $\pm 2\%$ in the value of D can be considered typical.

Two figures are shown for each soil continuously; the first shows damping vs. strain compared to damping curves given in (Vucetic & Dobry, 1991) (denoted as VD0, VD15 and VD30). The second figure shows measured damping values compared to estimated values by the RO fit obtained based on the degradation curves, given in Table 4-6; as well as estimated values based on the correlations of (Ishibashi & Zhang, 1993), (Zhang, Andrus, & Juang, 2005) and (Wichtmann & Triantafyllidis, 2013). In this figure, $\pm 3\%$ in the value of D is shown with dotted lines.

Altogether 261 values of damping have been measured for all soils either with RC or with TOSS. Some general tendencies can be observed from Figure 4-35 to Figure 4-52. Measured damping values are generally lower than the predictions of the VD0 curve. Even the VD15 curve seems to be an upper bound to measured values. The damping values predicted by the RO fits above $D = 2\%$ are approx. 5% higher, than the measured values and a similar trend is

true for the correlation of (Ishibashi & Zhang, 1993). The correlations of (Zhang, Andrus, & Juang, 2005) and (Wichtmann & Triantafyllidis, 2013) provide better estimates of measured values and in the most cases are within $\pm 3\%$ in the value of D . However for sample B1, which has the highest C_U value, Wichtmann's correlation considerably underestimates damping. Generally, out of the correlations from literature, the one provided by (Zhang, Andrus, & Juang, 2005) describes damping behavior of Danube sands the best.

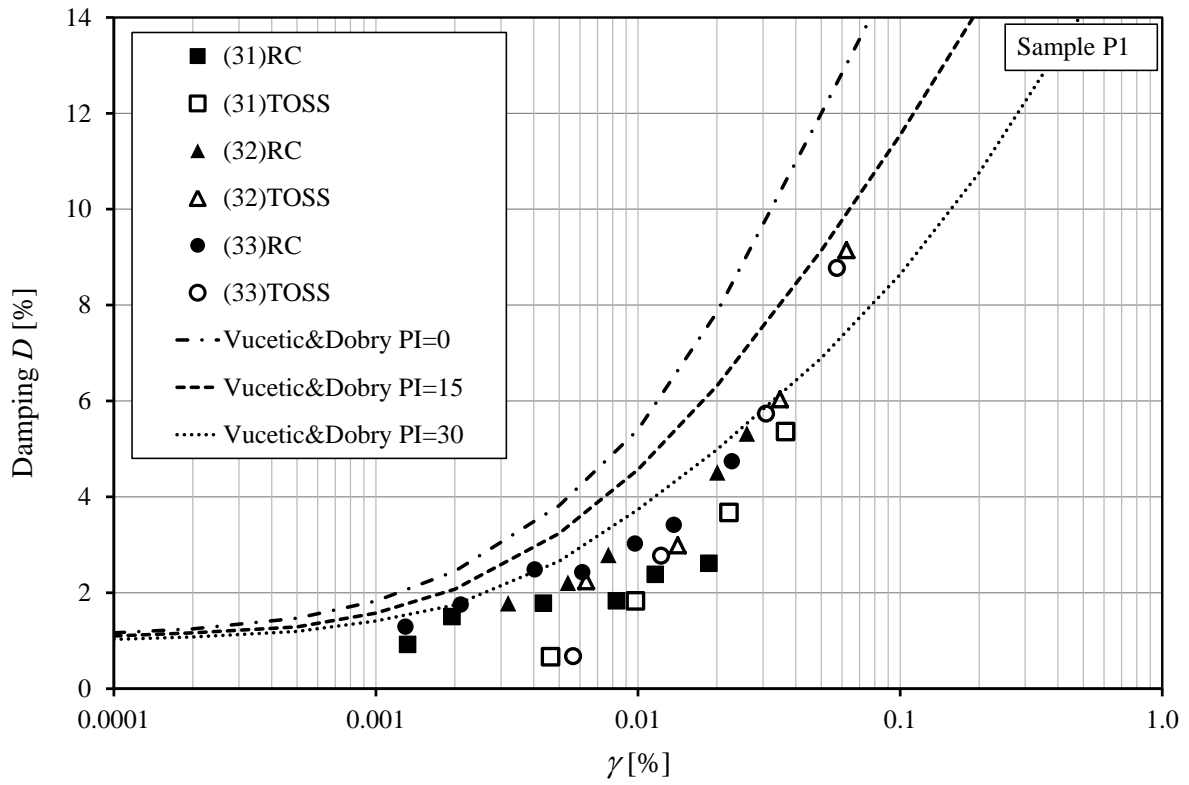


Figure 4-35 Damping curve for Sample P1 compared to correlations

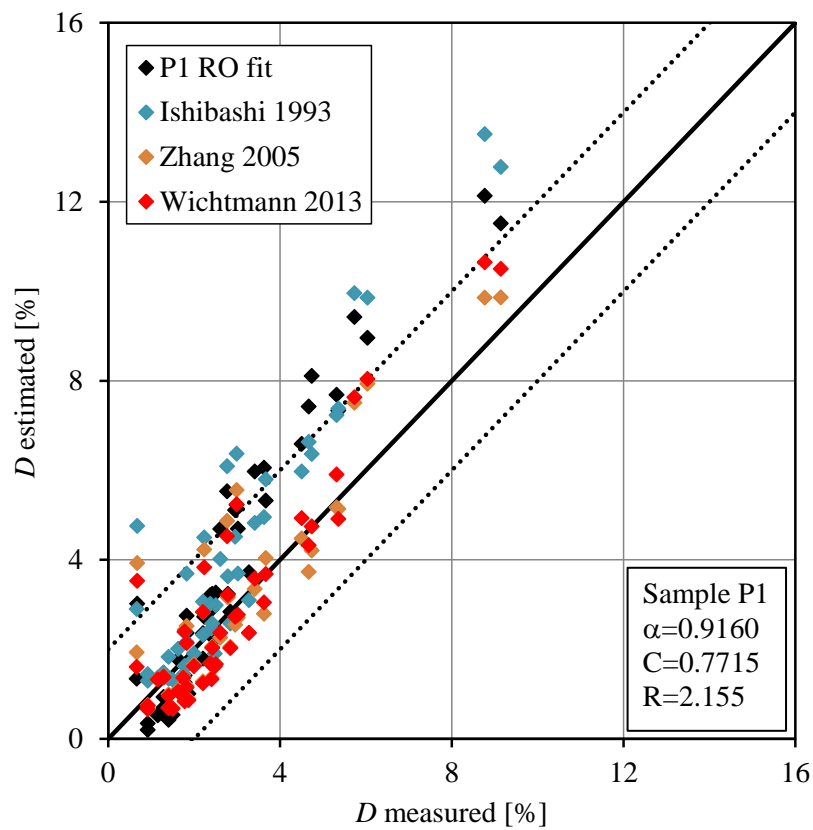


Figure 4-36 Measured vs. estimated values for damping with RO fit for Sample P1

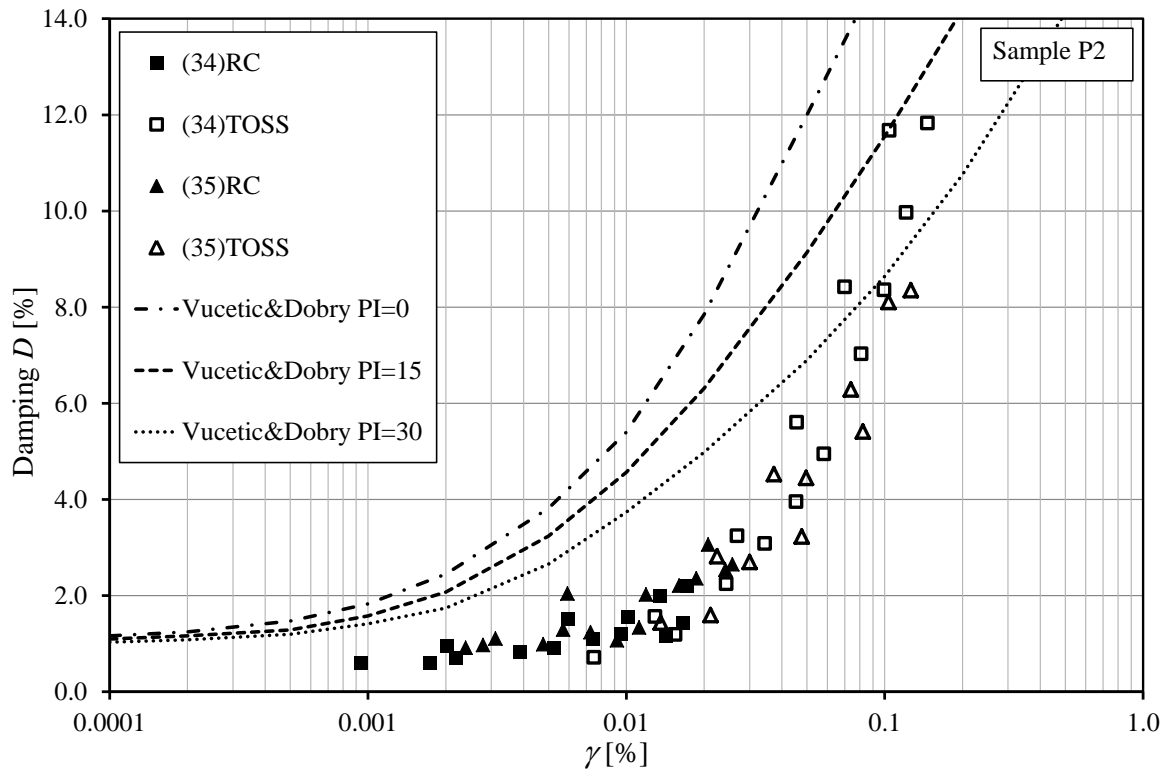


Figure 4-37 Damping curve for Sample P2 compared to correlations

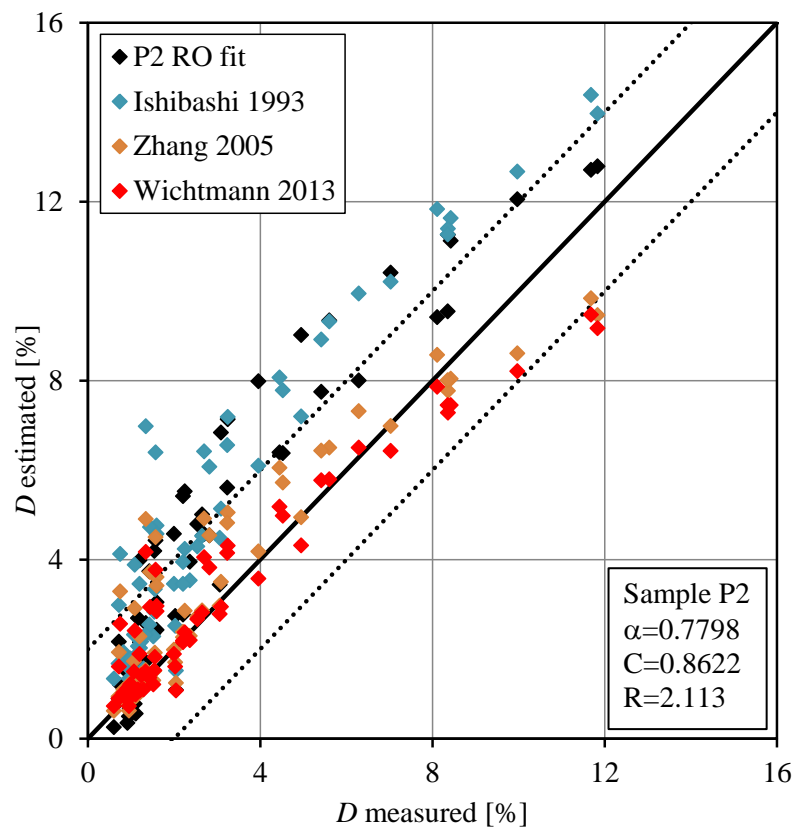


Figure 4-38 Measured vs. estimated values for damping with RO fit for Sample P2

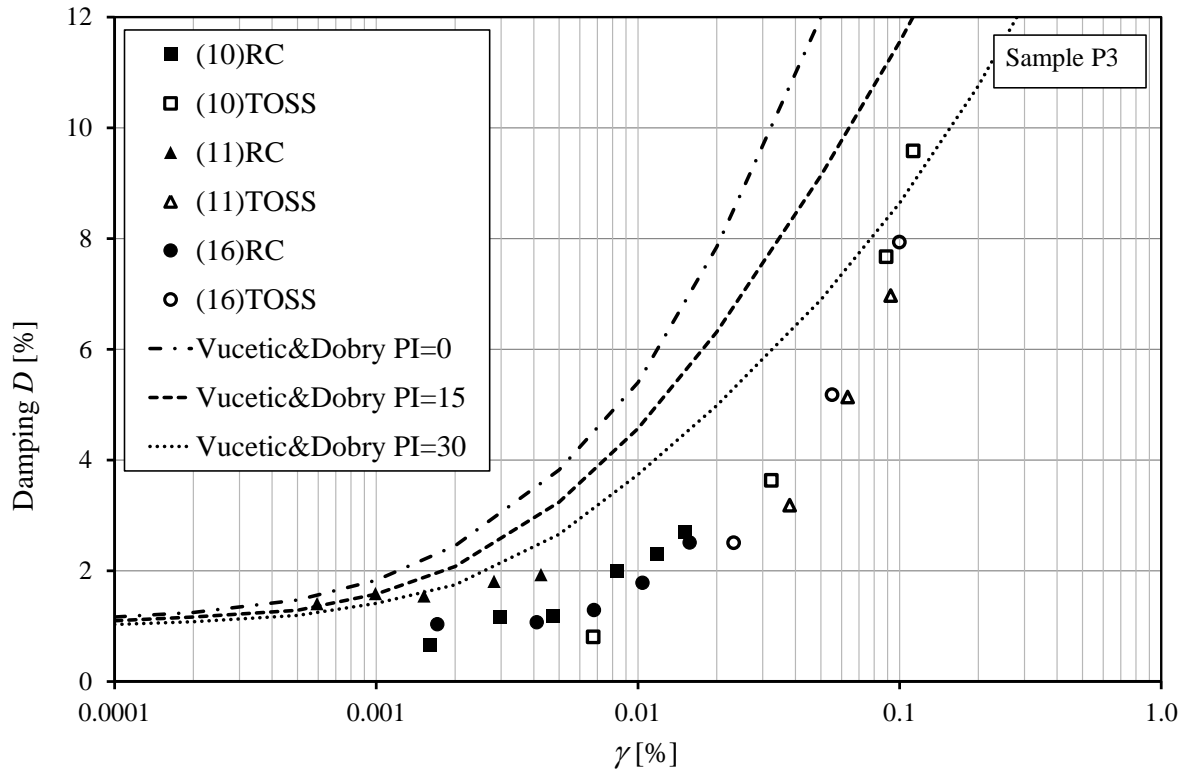


Figure 4-39 Damping curve for Sample P3 compared to correlations

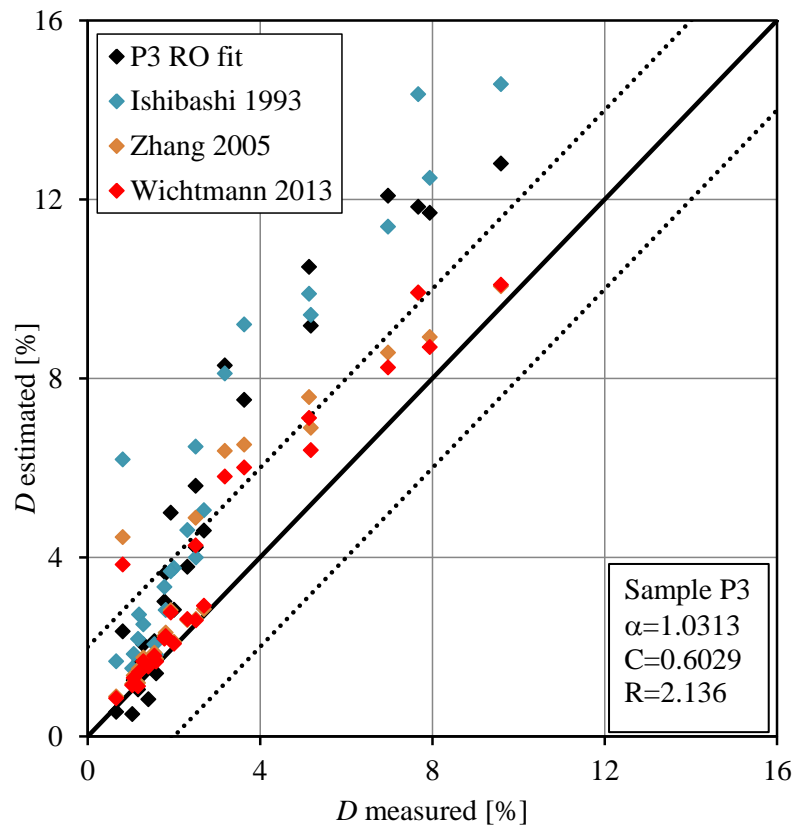


Figure 4-40 Measured vs. estimated values for damping with RO fit for Sample P3

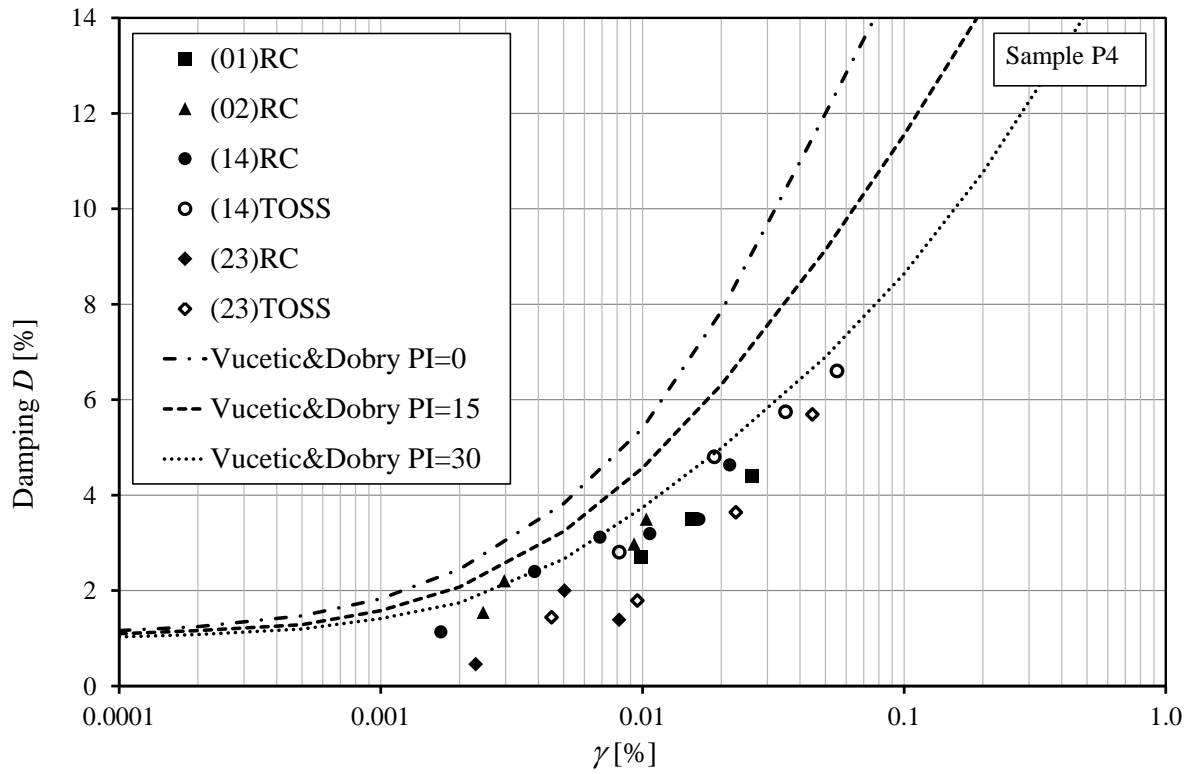


Figure 4-41 Damping curve for Sample P4 compared to correlations

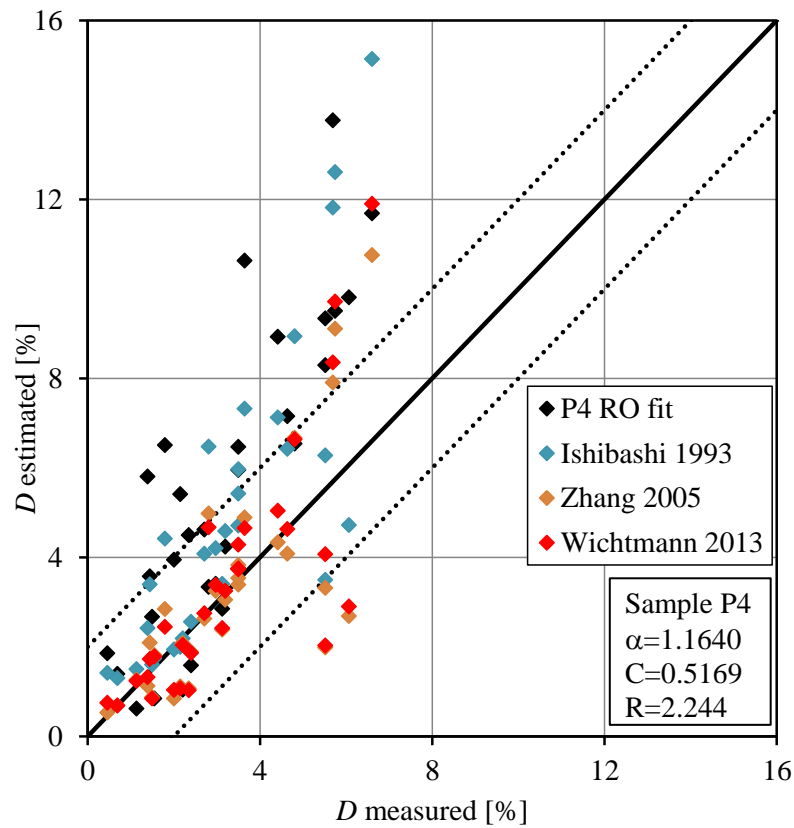


Figure 4-42 Measured vs. estimated values for damping with RO fit for Sample P4

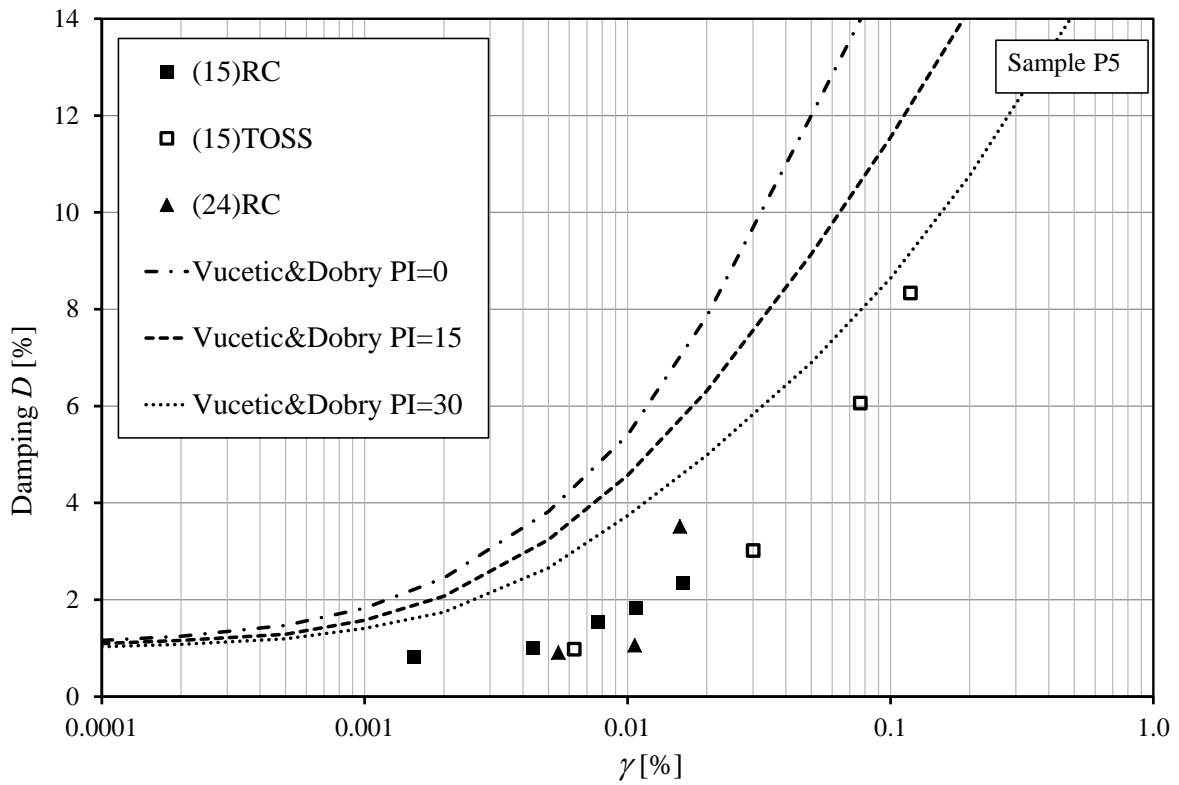


Figure 4-43 Damping curve for Sample P5 compared to correlations

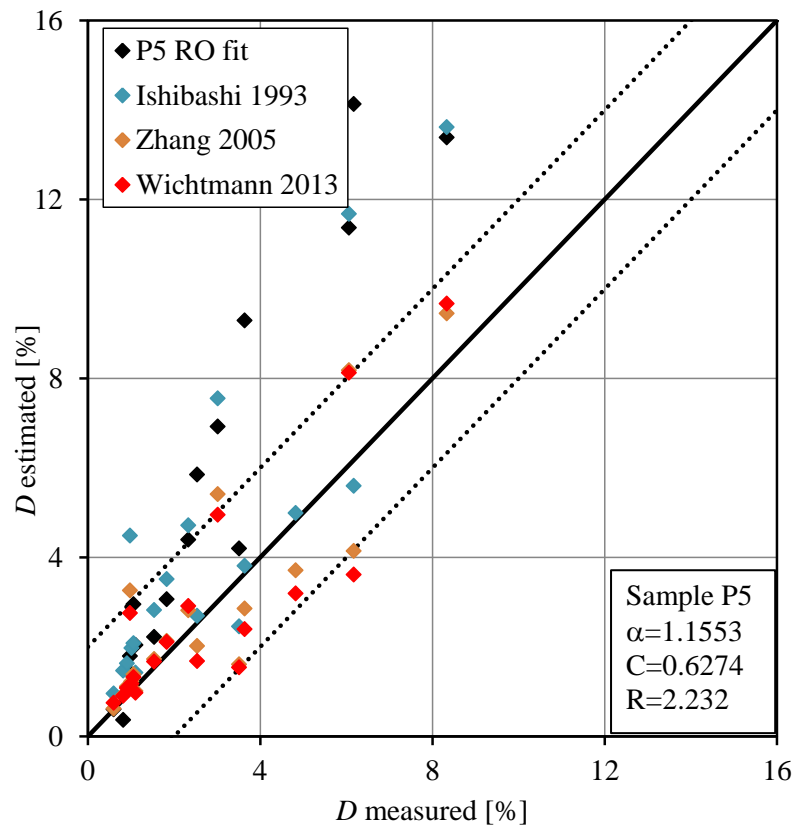


Figure 4-44 Measured vs. estimated values for damping with RO fit for Sample P5

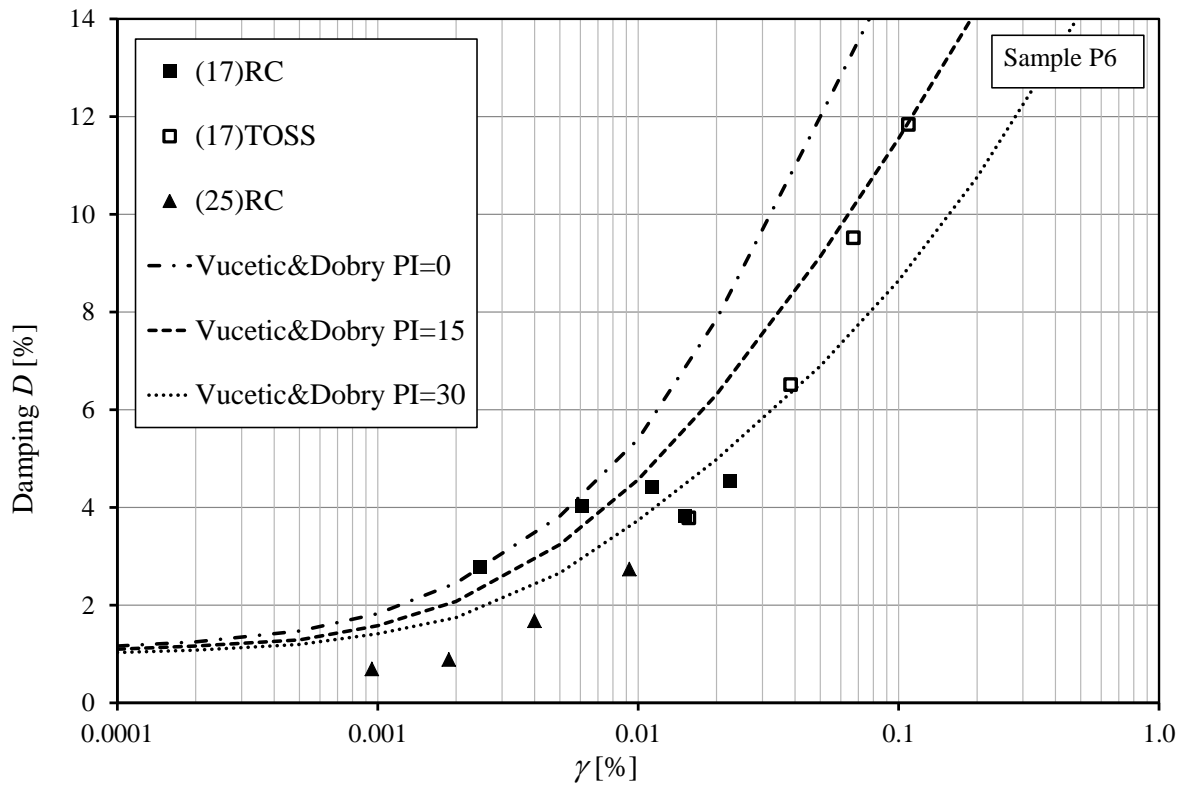


Figure 4-45 Damping curve for Sample P6 compared to correlations

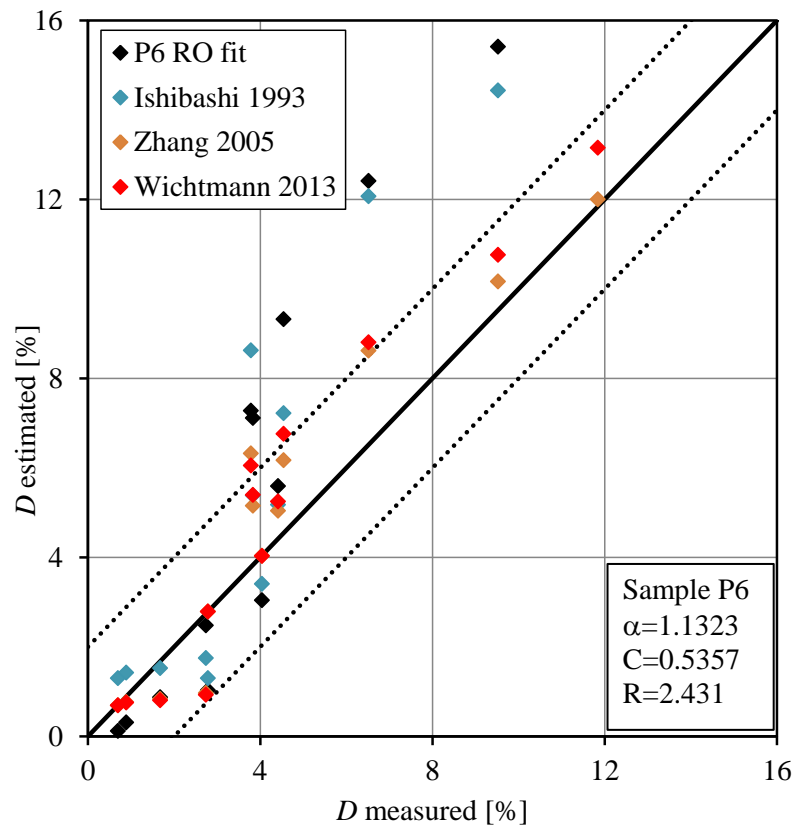


Figure 4-46 Measured vs. estimated values for damping with RO fit for Sample P6

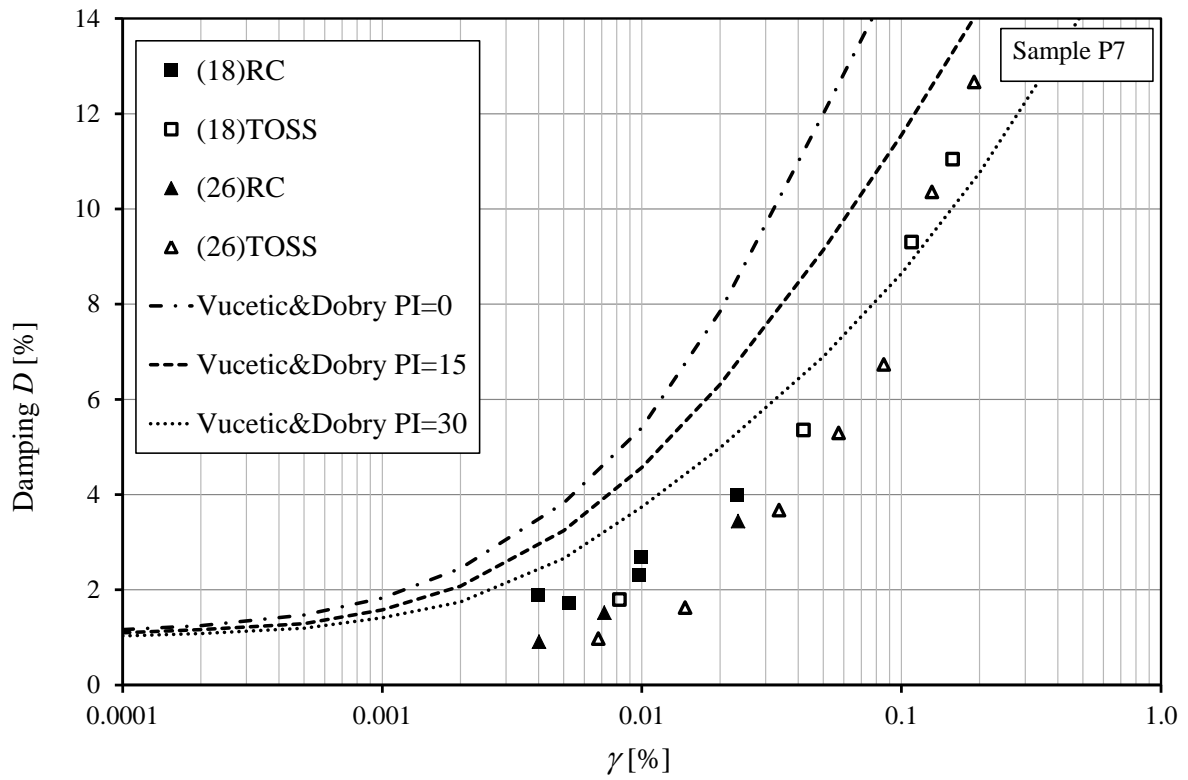


Figure 4-47 Damping curve for Sample P7 compared to correlations

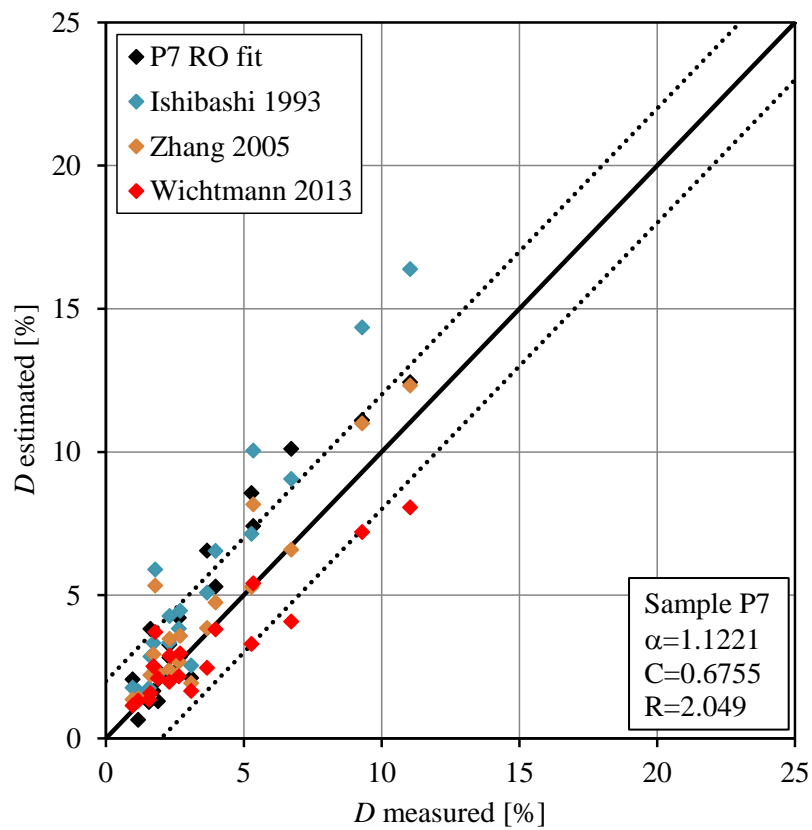


Figure 4-48 Measured vs. estimated values for damping with RO fit for Sample P7

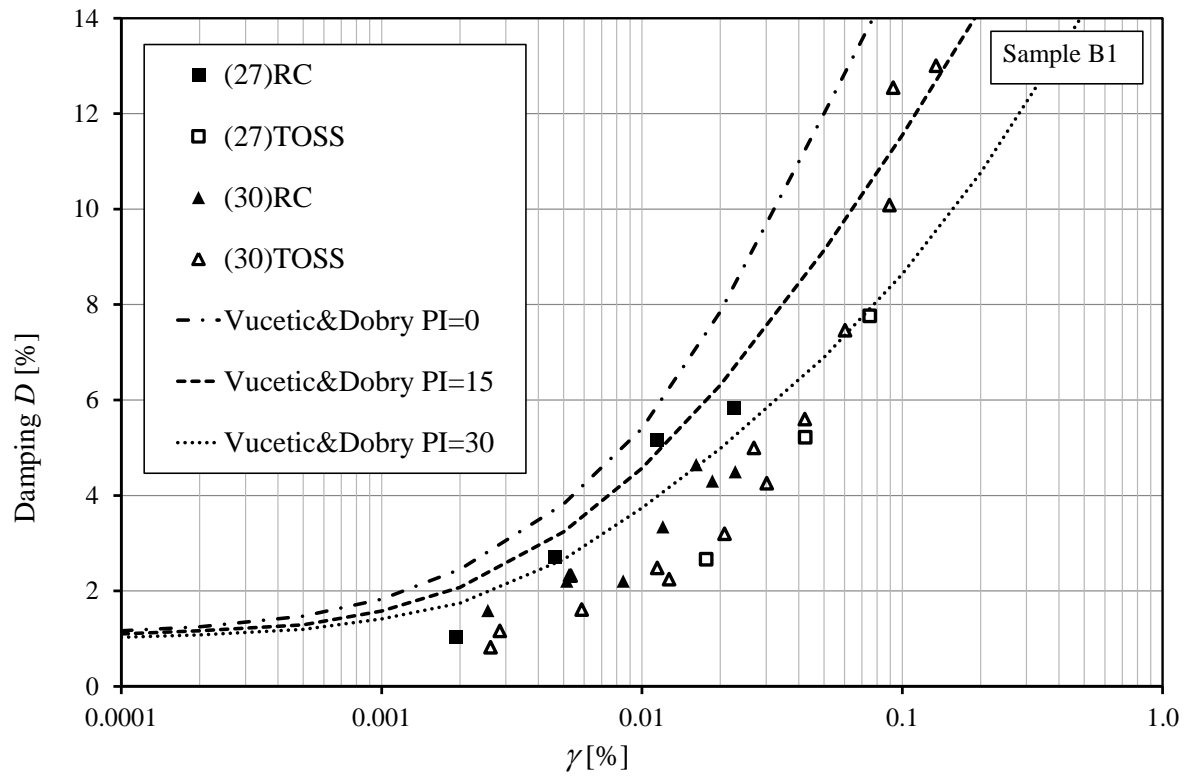


Figure 4-49 Damping curve for Sample B1 compared to correlations

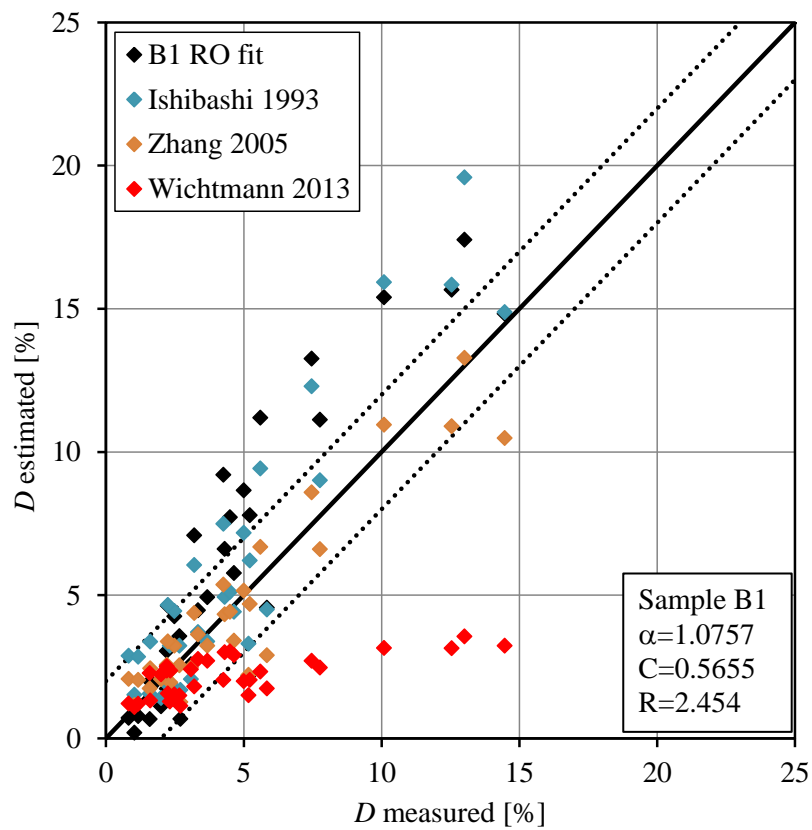


Figure 4-50 Measured vs. estimated values for damping with RO fit for Sample B1

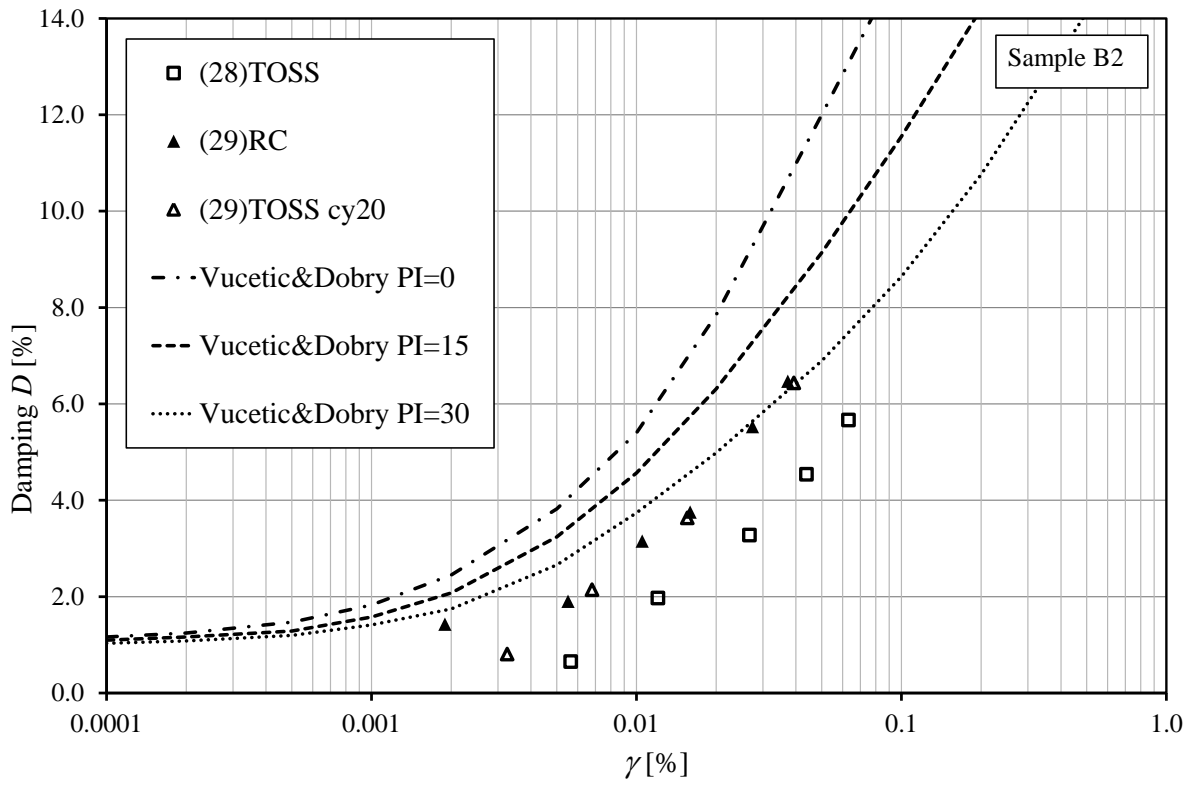


Figure 4-51 Damping curve for Sample B2 compared to correlations

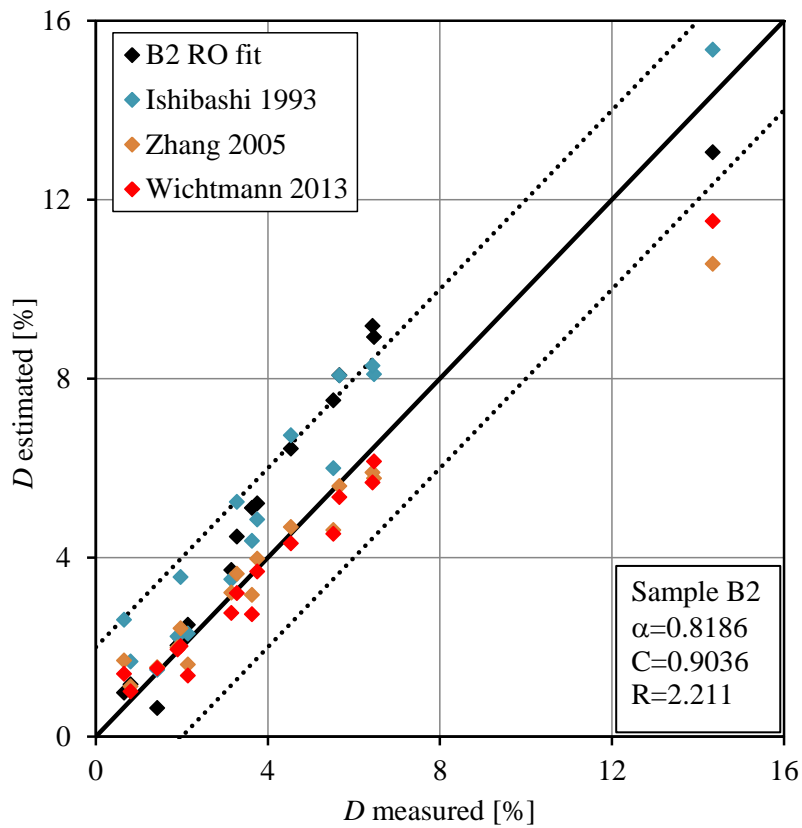


Figure 4-52 Measured vs. estimated values for damping with RO fit for Sample B2

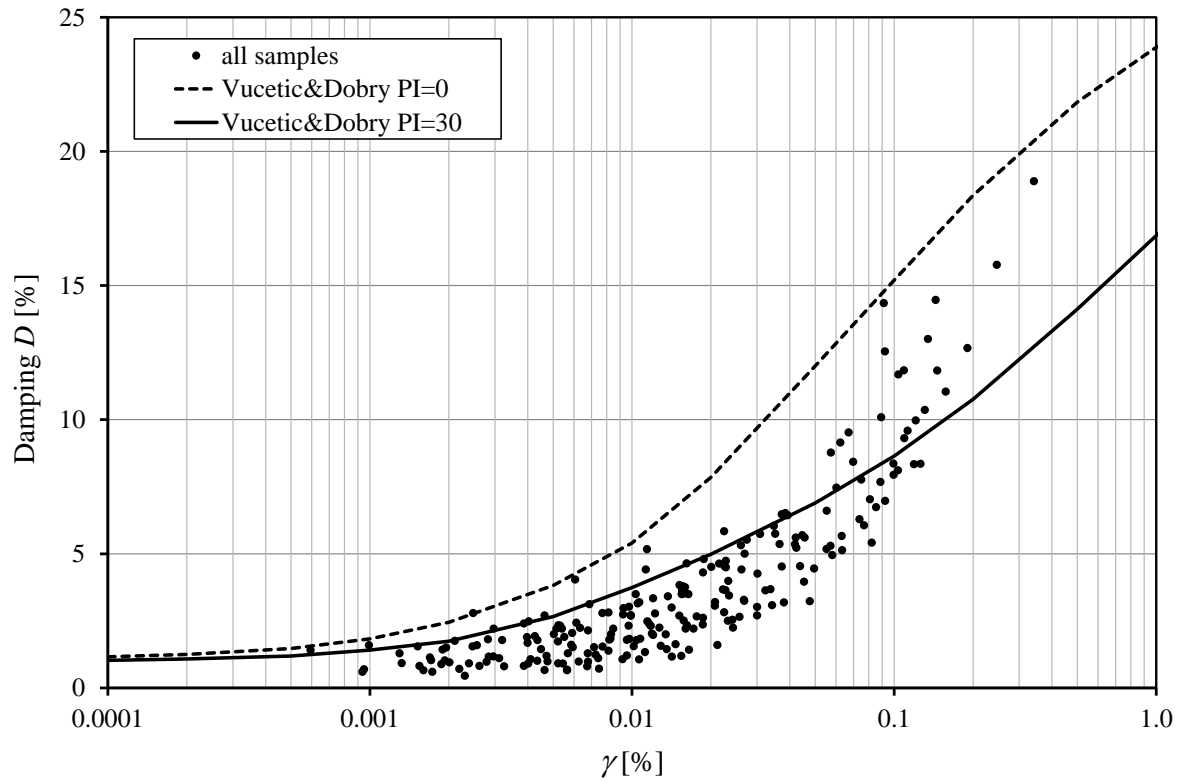


Figure 4-53 Measured damping values from all samples compared to correlations

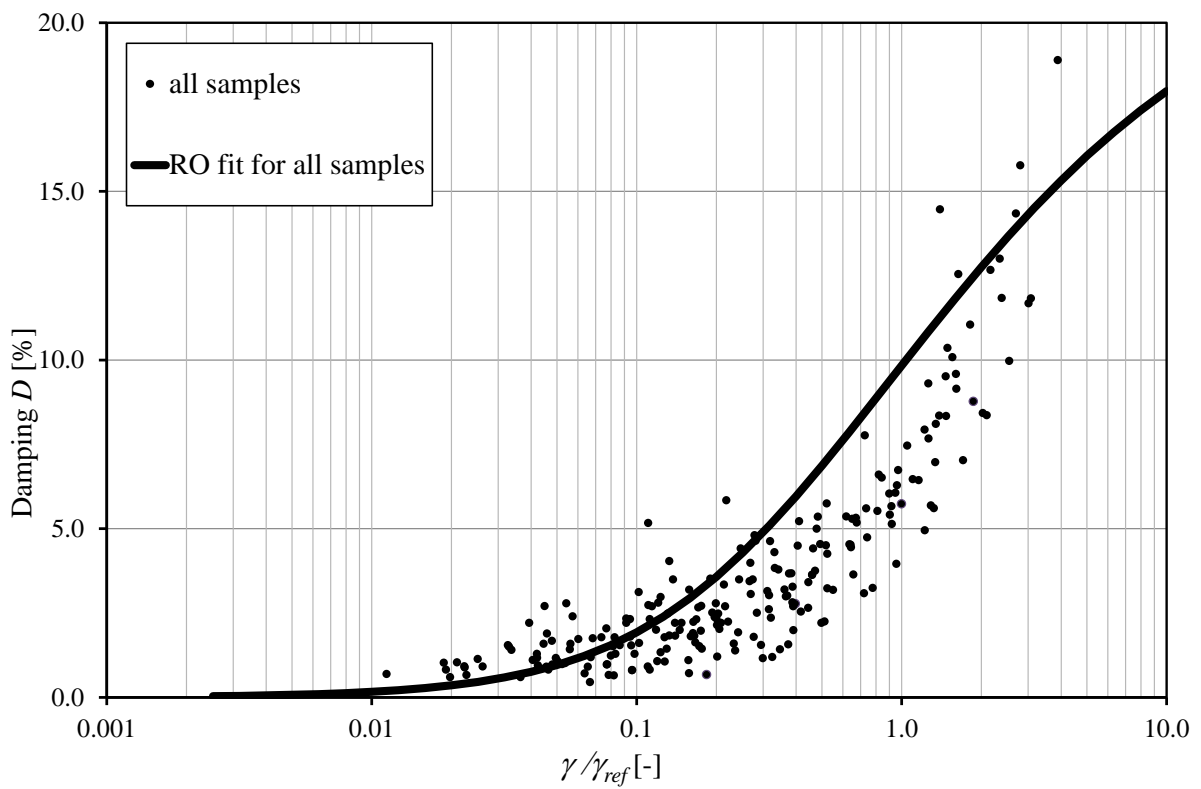


Figure 4-54 Measured damping values from all samples with RO fit

Figure 4-55 shows estimated D values vs. measured values. In this plot the closer the values are to the 45° line, the better the prediction. Coefficients of determination R^2 can also be calculated based on this plot. Obtained values of R^2 were 0.15 for the predictions of RO and (Ishibashi & Zhang, 1993), 0.78 for (Zhang, Andrus, & Juang, 2005) and 0.57 for (Wichtmann & Triantafyllidis, 2013). The correlation by (Zhang, Andrus, & Juang, 2005) can be considered acceptable, however for practical use, some modifications could be beneficial. The correlation given by Equation 2-48 was obtained by fitting the parameters c_1 and c_2 to many RC and TOSS test results and separate values were suggested to be used for RC and TOSS tests.

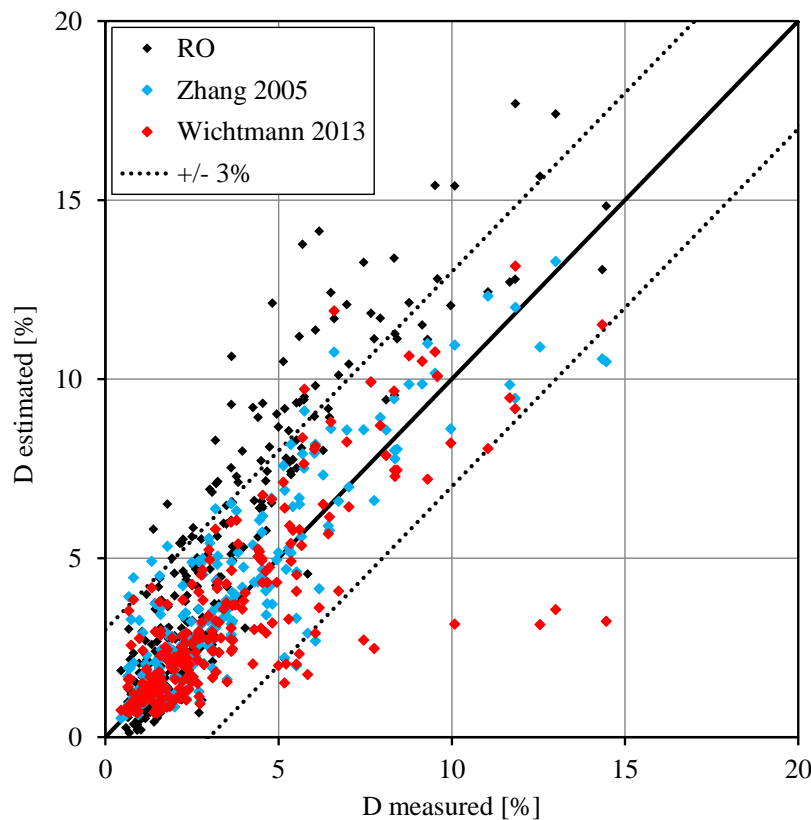


Figure 4-55 Measured vs. estimated values for damping with RO fit for each soil tested in this study

For practical calculations, a single set of constants would be more beneficial, therefore a regression analysis was performed in MS Excel with the GRG method and the following equation was obtained based on the measurements in this study:

$$D [-] = 0.1667 \left(\frac{G}{G_{max}} \right)^2 - 0.3932 \left(\frac{G}{G_{max}} \right) - 0.2165 \quad \text{Equation 4-1}$$

This equation was obtained in the same form as (Zhang, Andrus, & Juang, 2005) proposed Equation 2-48, with the constants $c_1 = 0.1667$, $c_2 = -0.3932$ and $D_{min} = 0.01$. Measured and estimated values with Equation 5-4 for all tested soils are shown in Figure 4-56. Coefficient of

determination R^2 based on this plot is 0.82, so the estimation is slightly better than the correlation of (Zhang, Andrus, & Juang, 2005) and hence it is suggested to be used for typical Danube sands.

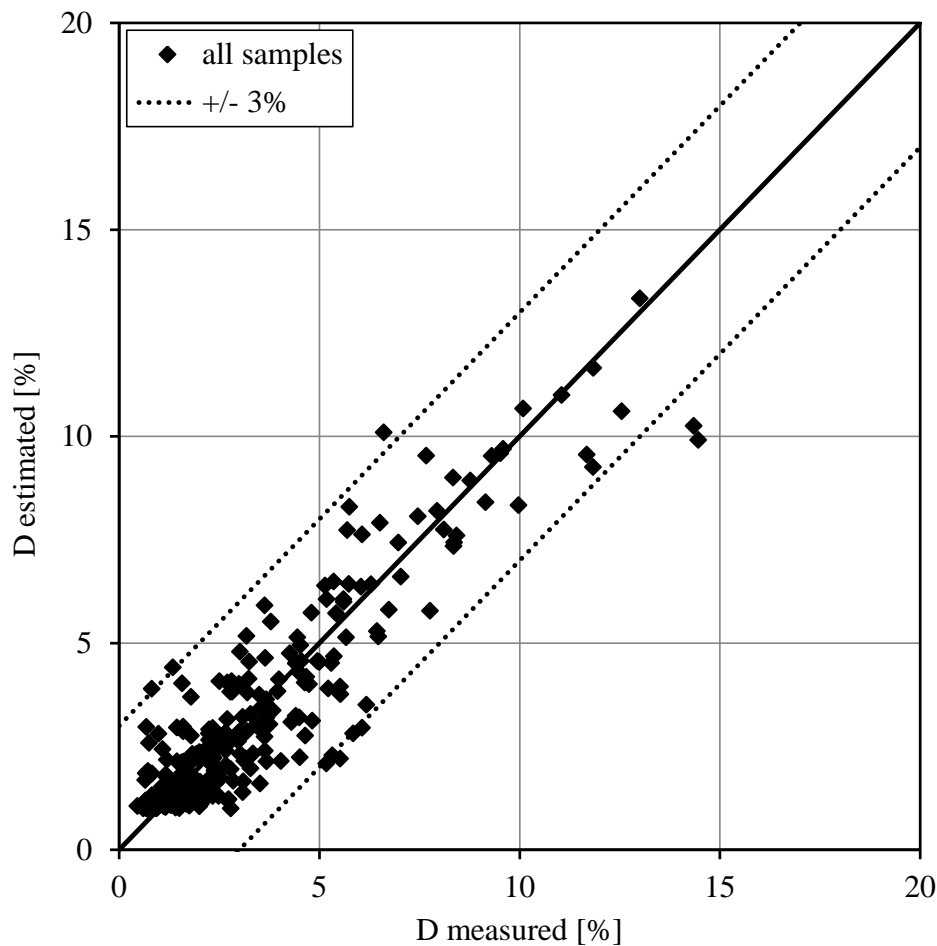


Figure 4-56 Measured vs. estimated values of damping with Equation 5-4

5 Thesis statements

Thesis statements were obtained based on the state-of-the-art combined Resonant Column and Torsional Shear Testing of nine air dry ($w_{max} < 2\%$), typical Danube Sands containing a small amount ($(Cl+Si) < 21\%$) of fine particles with various plasticity ($10\% < I_p < 18\%$), and comprising of sub-angular and rounded grains with $0,11 < d_{50} < 0,42$ mm. 69 RC tests and 19 TOSS tests were performed on samples with wide range of densities ($0,11 < I_D < 0,95$) under relevant confinement pressures ($80\text{kPa} < p' < 300$ kPa). This resulted in 69 measured values of G_{max} , 279 measured values of G/G_{max} and 261 measured values of D .

5.1 Thesis #1

I have shown that the further developed, combined Resonant Column-Torsional Shear Device with the testing procedure presented in this dissertation, which includes device assembly, preparation of hollow cylindrical sample, testing sequence and measurement result interpretation; is capable of measuring the very small strain shear stiffness G_{max} ; the modulus reduction curve and the damping curve of dry sands.

I have compared the obtained very small strain shear stiffness values to an independent set of measurements performed in a separate laboratory with the Bender Element Method by a separate researcher; and obtained acceptable agreement with 78% of the measured data within the $\pm 15\%$ deviation and 91% of the measured data within the $\pm 20\%$ deviation.

References: (Szilvagyi Z. , 2012), (Ray, R. P., Szilvagyi, Z., 2013), (Szilvagyi, Z., Hudacsek P., Ray, R.P, 2016), (Szilvagyi, Panuska, & Ray, 2018)

5.2 Thesis #2

I have developed a procedure to obtain the model parameters for the Ramberg-Osgood material model using small strain shear stiffness, modulus reduction and damping properties of a Danube Sand measured by Resonant Column and Torsional Shear Testing methods, by solving the inverse problem using MS Excel Solver's Generalized Reduced Gradient Method for minimizing the sum of squared errors between predicted and measured values of a hysteresis loop.

I have created a three-dimensional finite element model of the Torsional Shear Test and verified that the Ramberg-Osgood material model implemented in the software Midas GTS NX v2014 is capable of modeling the static Torsional Shear Test performed on a hollow cylinder sample with representation of the nonlinear material behavior concerning modulus reduction with increasing strain.

The verification by the back analysis of the Torsional Shear Test has not been done before with a nonlinear material model and indicates that the Ramberg-Osgood material model can be used in practical calculations requiring the modeling of stiffness degradation.

References: (Szilvagyi Z. , 2010), (Szilvagyi & Ray, 2018)

5.3 Thesis #3

I have compared the very small strain stiffness (G_{max}) of typical Danube sands at a wide range of densities and relevant confinements obtained by the Resonant Column method to correlations from literature and confirmed that out of the presented existing correlations the correlation given by (Carraro, Prezzi, & Salgado, 2009) gives the best estimate for G_{max} .

I have confirmed based on my measurement results with the Resonant Column method, that correlations which have been obtained for sands with non-plastic fines (Iwasaki & Tatsuoka, 1977) and (Wichtmann, Navarrete Hernandez, & Triantafyllidis, 2015), could underestimate G_{max} of sands with plastic fines by 30-35%.

This suggests, that over the content of fine particles, the plasticity of them has an even more dominant effect on G_{max} .

I have measured the very small strain stiffness (G_{max}) of typical Danube sands at a wide range of densities and relevant confinements with the Resonant Column method and obtained the following correlation for G_{max} :

$$G_{max} \text{ [MPa]} = 62 \frac{(2.17 - e)^2}{1 + e} \left(\frac{p'}{p_{atm}} \right)^{0.45} \quad \text{Equation 5-1}$$

where e is void ratio, p' is the mean effective stress in [kPa], and p_{atm} is the atmospheric pressure in [kPa]. The applicability of the most commonly used void ratio function in literature was confirmed by my measurement results and was used in the above equation. Coefficient of determination is $R^2=0.71$.

This correlation can be used in practical calculations for the estimation of G_{max} of typical Danube sands, in the absence of measurements.

References: (Szilvagyi Z. , 2012), (Ray, R. P., Szilvagyi, Z., 2013), (Szilvagyi, Z., Hudacsek P., Ray, R.P, 2016), (Szilvagyi, Panuska, & Ray, 2018)

5.4 Thesis #4

I have measured the stiffness degradation (G/G_{max}) of typical Danube sands at a wide range of densities and relevant confinements with the combined Resonant Column and Torsional Shear test methods and obtained the following degradation curve formulated in the Ramberg-Osgood material model:

$$\frac{G}{G_{max}} = \frac{1}{1 + 0.8334 \left| \frac{\tau}{0.6386 \tau_{max}} \right|^{1.142}} \quad \text{Equation 5-2}$$

where G is the secant shear modulus, G_{max} is the very small strain stiffness, τ is shear stress, τ_{max} is shear strength. Coefficient of determination R^2 is 0.89.

This degradation curve can be used in practical calculations to describe the stiffness degradation behavior of typical Danube sands.

References: (Szilvgyi Z. , 2012), (Ray, R. P., Szilvgyi, Z., 2013), (Szilvgyi, Z., Hudacsek P., Ray, R.P, 2016), (Szilvgyi, Panuska, & Ray, 2018)

5.5 Thesis #5

I have measured the damping (D) increase with strain of typical Danube sands at a wide range of densities and relevant confinements with the Resonant Column and Torsional Shear test method and obtained the following correlation for damping:

$$D [-] = 0.1667 \left(\frac{G}{G_{max}} \right)^2 - 0.3932 \left(\frac{G}{G_{max}} \right) - 0.2165 \quad \text{Equation 5-3}$$

where G/G_{max} is the stiffness degradation value at a given strain level. Coefficient of determination is $R^2=0.82$.

This correlation can be used in practical calculations for the estimation of D of typical Danube sands, in the absence of measurements.

References: (Szilvgyi Z. , 2012), (Ray, R. P., Szilvgyi, Z., 2013), (Szilvgyi, Z., Hudacsek P., Ray, R.P, 2016), (Szilvgyi, Panuska, & Ray, 2018)

6 Summary and future research

In my dissertation I have presented, how small strain stiffness of Danube sands can be described and modeled based on state-of-the art laboratory measurements. A detailed literature review on the modeling of small strain stiffness of soils has been presented to provide insight into the most commonly used model parameters; and their determination based on correlations has also been investigated. A comprehensive laboratory testing program has been performed on nine selected typical Danube Sands with the combined Resonant Column-Torsional Shear device. Measurement results have been compared to an independent set of measurements performed by a fellow

PhD student at a different laboratory with the Bender Element test method. Very good agreement has been found between the results. Besides testing, data interpretation has also been developed by solving the inverse problem of choosing most suitable model parameters, which provide the closest behavior with the used material model as the measurements. For this, the 3D finite element model of the Torsional Shear Test has been developed and the modeling of a TOSS test has been performed with use of the nonlinear Ramberg-Osgood material model. Finally, measurement results have been presented and new correlations have been obtained for the most important parameters, which can be used to estimate them in the absence of measurements.

It has been emphasized, that some features of this complex behavior still need investigations. Some of these topics can be further investigated in laboratory; some can be modeled with the presented FEM modeling process. Laboratory testing should focus on the effects of irregular loading, especially RC testing after TOSS prestraining and perhaps a more precise measurement method of void ratio could be developed. Comparison of laboratory measurements to in-situ testing is another difficult task in this topic and needs further research. Effects of uneven distribution of density, imperfections due to sample preparation could be investigated by further modeling.

An additional topic concerns the application of dynamic soil parameters in modeling, especially in ground response analysis, which can be used to assess the specific value of the earthquake load, based on local soil conditions. Our first studies in this field (Kegys-Brassai, Wolf, Szilvgyi, & Ray, 2017), (Szilvgyi, et al., 2017) confirmed, that the nonlinear behavior of surface near soil layers have a major effect on earthquake loading and if the profile is not homogeneous or nearly so, a substantial degree of amplification can be expected.

References

- Afifi, S., & Richart, F. (1973). Stress-history effects on shear modulus of soils. In *Soils and foundations 13(1)* (pp. 77-95.). <http://doi.org/10.3208/sandf1972.13.77>.
- Alpan, I. (1970). The geotechnical properties of soils. In *Earth-Science Reviews*, 6 (pp. 5-49). <http://doi.org/10.3208/sandf1972.13.77>.
- ASTM. (2015). ASTM D4015-15e1, Standard Test Methods for Modulus and Damping of Soils by Fixed-Base Resonant Column Devices. West Conshohocken, PA: ASTM International.
- Atkinson, J. H., & Salfors, G. (1991). Experimental determination of soil properties. In *Proc. 10th ECSMFE, Vol 3* (pp. 915-956). Florence.
- Ban, Z., Katona, T., & Mahler, A. (2016). Comparison of empirical liquefaction potential evaluation methods. In *Pollack Periodica: An international Journal for Engineering and Information Sciences 11(1)* (pp. 55-66).
- Benz, T. (2006). *Small strain stiffness of soils and its numerical consequences, PhD Dissertation*. http://www.uni-stuttgart.de/igs/content/publications/IGS_Dissertationen/Diss_Benz.pdf: Universitat Stuttgart Institut fur Geotechnik.
- Biarez, J., & Hicher, P. (1994). *Elementary Mechanics of Soil Behavior*. Balkema: ISBN : 9054101571 .
- Brinkgreve, R., & Engin, E. (2013). Validation of geotechnical finite element analysis. In *Proceedings of the 18th International Conference on Soil Mechanics and Geotechnical Engineering* (pp. 677-682.). <http://www.issmge.org/uploads/publications/1/2/677-682.pdf>: ISSMGE TC 103.
- Burland, J. B. (1989). Ninth Laurits Bjerrum Memorial Lecture: Small is beautiful - the stiffness of soils at small strains. In *Canadian Geotechnical Journal, Vol 26(4)* (pp. 499-516). <https://doi.org/10.1139/t89-064>.
- Cai, Y., Dong, Q., Wang, J., Gu, C., & Xu, C. (2015). Measurement of small strain shear modulus of clean and natural sands in saturated condition using bender element test. In *oil Dynamics and Earthquake Engineering 76* (pp. 100-110). <https://doi.org/10.1016/j.soildyn.2014.12.013>.
- Camacho-Tauta, J., Cascante, G., Viana Da Fonseca, A., & Santos, J. (2015). Time and frequency domain evaluation of bender element systems. In *Geotechnique 65(7)* (pp. 548-562). <https://doi.org/10.1680/geot.13.P.206>.

- Carraro, J., Prezzi, M., & Salgado, R. (2009). Shear strength and stiffness of sands containing plastic or nonplastic fines. In *Journal of Geotechnical and Geoenvironmental Engineering, ASCE* (pp. 1167-1178). [https://doi.org/10.1061/\(ASCE\)1090-0241\(2009\)135:9\(1167\)](https://doi.org/10.1061/(ASCE)1090-0241(2009)135:9(1167)).
- Chaudhary, S., Kuwano, J., & Hayano, Y. (2004). Measurement of quasi-elastic stiffness parameters of dense Toyoura sand in hollow cylinder apparatus and triaxial apparatus with bender elements. In *Geotechnical Testing Journal*, 27(1) (pp. 1-13). <https://doi.org/10.1520/GTJ11389>.
- Clayton, C. R. (2011). Stiffness at small strain: research and practice. In *Geotechnique 61, No.1* (pp. 5-37). <https://doi.org/10.1520/GTJ11389>.
- Darendeli, B. (2001). Development of a new family of normalized modulus reduction and material damping curves. In *PhD dissertation* (pp. 1-362). University of Texas at Austin, USA: <http://hdl.handle.net/2152/10396>.
- DGGT. (2001). Empfehlungen des Arbeitskreises 1.4 "Baugrunddynamik" der Deutschen Gesellschaft fur Geotechnik. <https://doi.org/10.1002/bate.199805430>.
- Ferreira, C., A., V. D., & Santos, J. (2006). Comparison of simultaneous bender elements and resonant column tests on Porto residual soil. In H. I. (eds.), *Soil stress-strain behavior: measurement, modeling and analysis geotechnical symposium, Roma* (pp. 523-535). https://doi.org/10.1007/978-1-4020-6146-2_34.
- Fioravante, V. (2000). Anisotropy of small-strain stiffness of Ticino and Kenya sands from. In *Soils and Foundations*, 40(4) (pp. 129-142). https://doi.org/10.3208/sandf.40.4_129.
- Greening, P., & Nash, D. (2004). Frequency domain determination of G₀ using bender elements. In *Geotechnical Testing Journal* 27(3) (pp. 1-7). <https://doi.org/10.1520/GTJ11192>.
- Gu, Y., Yang, J., Huang, M., & Gao, G. (2015). Bender element tests in dry and saturated sand: Signal interpretation and result comparison. In *Soils and Foundations* 55(5) (pp. 952-963). <https://doi.org/10.1016/j.sandf.2015.09.002>.
- Hardin, B., & Black, W. (1966). Sand stiffness under various triaxial stresses. In *Journal of the Soil Mechanics and Foundations Division ASCE* 92(SM2) (pp. 27-42). <https://trid.trb.org/view.aspx?id=38495>.
- Hardin, B., & Drnevich, V. (1972). Shear modulus and damping in soils: Design equations and curves. In *Journal of the Soil Mechanics and Foundations Division, ASCE* 98(SM7) (pp. 667-692). <https://trid.trb.org/view.aspx?id=126413>.

- Hardin, B., & Richart, F. (1963). Elastic wave velocities in granular soils. In *Journal of the Soil Mechanics and Foundations Division Vol89 (SMI)* (pp. 33-65). <https://trid.trb.org/view.aspx?id=140078>.
- Hoque, E., & Tatsuoka, F. (2000). Kinematic elasticity of a granular material. In *In Proc. GeoEng2000, Melbourne*. <https://www.onepetro.org/conference-paper/ISRM-IS-2000-231>.
- Hoque, E., & Tatsuoka, F. (2004). Effects of stress ratio on small-strain stiffness during triaxial shearing. In *Gotechnique 54(7)* (pp. 429-439). <https://doi.org/10.1680/geot.2004.54.7.429>.
- Idriss, I. M., Dobry, R., & Singh, R. D. (1978). Nonlinear behavior of soft clays during cyclic loading. In *Journal of the Geotechnical Engineering Division 104:12* (pp. 1427-1447). <https://trid.trb.org/view.aspx?id=86207>.
- Ishibashi, I., & Zhang, X. (1993). Unified dynamic shear modulus and damping ratios of sand and clay. In *Soils and Foundations Vol33(1)* (pp. 182-191). Japanese Society of Soil Mechanics and Foundation Engineering <http://doi.org/10.3208/sandf1972.33.182>.
- Ishihara, K. (1996). *Soil Behavior in Earthquake Geotechnics*. New York: Oxford University Press [http://doi.org/10.1002/\(SICI\)1096-9845\(199711\)26:11<1187::AID-EQE663>3.0.CO;2-Q](http://doi.org/10.1002/(SICI)1096-9845(199711)26:11<1187::AID-EQE663>3.0.CO;2-Q).
- Iwasaki, T., & Tatsuoka, F. (1977). Effects of grain size and grading on dynamic shear moduli of sands. In *Soils and Foundations Vol17(3)* (pp. 19-35). Japanese Society of Soil Mechanics and Foundation Engineering http://doi.org/10.3208/sandf1972.17.3_19.
- Jamiolkowski, M., Lancellotta, R., & Lo Presti, D. (1995). Remarks on the stiffness at small strains of six italian clays. In *Shibuya&Miura (eds.), Pre-failure Deformation of Geomaterials Vol1* (pp. 817-836). Balkema: Rotterdam: ISBN: 905410399X.
- Jovicic, V., & Coop, M. (1997). Stiffness of coarse-grained soils at small strains. In *Gotechnique Vol47(3)* (pp. 545-561). <https://doi.org/10.1680/geot.1997.47.3.545>.
- Jovicic, V., Coop, M., & Simic, M. (1996). Objective criteria for determining Gmax from bender element tests. In *Gotechnique 46(2)* (pp. 357-362). <https://doi.org/10.1680/geot.1996.46.2.357>.
- Kallioglou, T., Papadopoulou, A., & Ptilakis, K. (2003). Shear modulus and damping of natural sands. In T. D. H. Di Benedetto, *Deformation Characteristics of Geomaterials* (pp. 401-407). Proc. IS-Lyon: A.A. Balkema <https://doi.org/10.1201/NOE9058096043.ch50>.
- Kegyes-Brassai, O. (2016). *Earthquake Hazard Analysis and Building Vulnerability Assessment to Determine the Seismic Risk of Existing Buildings in an Urban Area*.

- Győr: MultidiszciplinÁris Műszaki Tudományi Doktori Iskola, Széchenyi István Egyetem DOI: 10.15477/SZE.MMTDI.2015.002.
- Kegyés-Brassai, O., Ray, R., & Tildy, P. (2015). Predictive equations for soil shear-wave velocities of Hungarian soils based on MASW and CPT measurements around Győr. In *Acta Geodetica et Geophysica Hungarica* 50(4) (pp. 1-22). <https://doi.org/10.1007/s40328-015-0148-y>.
- Kegyés-Brassai, O., Wolf, Á., SzilvÁgyi, Z., & Ray, R. (2017). Effects of local ground conditions on site response analysis results in Hungary. In *Proceedings of 19th International Conference On Soil Mechanics and Geotechnical Engineering* (pp. 2003-2006). Seoul, South Korea: ICSMGE.
- Koch, E., & Hudacsek, P. (2017). Modeling of railway transition zones under dynamic loading (in print). In P. o. Engineering. Seoul, South Korea: International Society for Soil Mechanics and Geotechnical Engineering.
- Kottke, A., Wang, X., & Rathje, E. (2013). Technical Manual for Strata. Geotechnical Engineering Center, University of Texas.
- Kramer, S. L. (1995). *Geotechnical Earthquake Engineering*. New Jersey: Prentice Hall ISBN-13: 978-0133749434.
- Kuwano, R., & Jardine, R. (2002). On the application of cross-anisotropic elasticity to granular materials at very small strains. In *Géotechnique* 52(10) (pp. 727-749). <https://doi.org/10.1680/geot.2002.52.10.727> .
- Lo Presti, D., Pallara, O., Lancellotta, R., Armandi, M., & Maniscalco, R. (1993). Monotonic and cyclic loading behaviour of two sands at small strains. In *Geotechnical Testing Journal* 16(4) (pp. 409-424). <https://doi.org/10.1520/GTJ10281J>.
- Lysmer, J., Udaka, T., Tsai, C., & Seed, H. (1975). FLUSH - A computer program for approximate 3-D analysis of soil-structure interaction problems. In *Earthquake Engineering Research Center, Report No. EERC-75-30* (pp. 1-134). California, Berkeley.
- Masing, G. (1926). Eigenspannungen und Verfestigung beim Messing. In *Proc. 2nd Int. Congr. Appl. Mech.* Zurich.
- McMechan, G. (1983). Seismic tomography in boreholes. In *Geophysical Journal International* Vol74. Issue2. (pp. 601-612). <https://doi.org/10.1111/j.1365-246X.1983.tb01891.x>.
- MIDAS Information Technology Co., L. (2014). Midas GTS NX 2014 v2.1 Analysis Reference, Chapter 4. Materials. <http://midasgtsnx.com/>.

- Oztoprak, S., & Bolton, M. (2013). Stiffness of sands through a laboratory test database. In *Geotechnique* 63 No1 (pp. 54-70). <https://doi.org/10.1680/geot.10.P.078>.
- Payan, M., Khoshghalb, A., Senetakis, K., & Khalili, N. (2016). Small-strain stiffness of sand subjected to sand anisotropy. In *Soil Dynamics and Earthquake Engineering* 88 (pp. 143-151). <https://doi.org/10.1016/j.soildyn.2016.06.004>.
- Puzrin, A. (2012). *Constitutive Modeling in Geomechanics*. Springer Berlin Heidelberg <https://doi.org/10.1007/978-3-642-27395-7>.
- Pyke, R. (1979). Nonlinear soil models for irregular cyclic loadings. In *Proc. ASCE: Journal of the Geotechnical Engineering Division, 105(GT6)* (pp. 715-726). <https://trid.trb.org/view.aspx?id=161072>.
- Ramberg, W., & Osgood, W. R. (1943). Description of stress strain curves by three parameters. In *National Advisory Committee for Aeronautics, Technical Note No. 902*. (p. 28). <https://ntrs.nasa.gov/search.jsp?R=19930081614>.
- Ray, R. P. (1983). *Changes in shear modulus and damping in cohesionless soils due to repeated loading, PhD Dissertation*. University of Michigan [https://doi.org/10.1061/\(ASCE\)0733-9410\(1988\)114:8\(861\)](https://doi.org/10.1061/(ASCE)0733-9410(1988)114:8(861)).
- Ray, R. P. (2014). *Geotechnikai kezikonyv foldrengesre valo merevezeshez*. (I. Lazanyi, Z. Szilvgyi, & . Wolf, Eds.) Budapest: MMK Geotechnikai Tagozat, Artifex Kiado ISBN: 978-963-7754-09-8 .
- Ray, R. P., Szilvgyi, Z. (2013). Measuring and modeling the dynamic behavior of Danube Sands. In *Proceedings 18th International Conference on Soil Mechanics and Geotechnical Engineering: Challenging and Innovations in Geotechnics* (pp. 1575-1578). Paris: <http://www.cfms-sols.org/sites/default/files/Actes/1575-1578.pdf>.
- Ray, R. P., Szilvgyi, Z., & Wolf, . (2014). Talajdinamikai parameterek meghatarozasa s alkalmazasa. In *Sinek Vilaga* 56. (pp. 32-36).
- Ray, R., & Woods, R. (1988). Modulus and damping due to uniform and variable cyclic loading. In *Journal of Geotechnical Engineering* 114.8 (old.: 861-876). ASCE [https://doi.org/10.1061/\(ASCE\)0733-9410\(1988\)114:8\(861\)](https://doi.org/10.1061/(ASCE)0733-9410(1988)114:8(861)).
- Robertson, P., & Cabal, K. (2014). *Guide to Cone Penetration Testing for Geotechnical Engineering*. California, USA: Gregg Drilling & Testing Inc.
- Sahaphol, T., & Muira, S. (2005). Shear moduli of volcanic soils. In *Soil Dynamics and Earthquake Engineering* 25 (pp. 157-165). <https://doi.org/10.1016/j.soildyn.2004.10.001>.

- Santos, J., & Correira, A. (2000). Shear modulus of soils under cyclic loading at small and medium strain level. In *Proceedings of the 12th World Conference on Earthquake Engineering* (pp. 1-8).
- Sawangsurriya, A. (2006). Stiffness-suction-moisture relationship for compacted soils. In *PhD thesis* (pp. 1-259). University of Wisconsin-Madison.
- Seed, H., & Idriss, I. (1970). Soil moduli and damping factors for dynamic response analysis. In *Technical Report EERC 70-10, Earthquake Engineering Research Center, University of Cal. Berkeley*.
- Seed, H., Wong, R., Idriss, I., & Tokimatsu, K. (1986). Moduli and damping factors for dynamic analyses of cohesionless soil. In *Journal of Geotechnical Engineering ASCE* 112(11) (pp. 1016-1032). [https://doi.org/10.1061/\(ASCE\)0733-9410\(1986\)112:11\(1016\)](https://doi.org/10.1061/(ASCE)0733-9410(1986)112:11(1016)).
- Simon, J., & Vigh, G. (2017). Parametric seismic evaluation of highway overpass bridges in moderate seismic areas. In *Earthquakes and Structures Vol12(3)* (pp. 375-388). doi.org/10.12989/eas.2017.12.3.375.
- Smolczyk, U. (2002). *Geotechnical Engineering Handbook*. Berlin: Ernst und Sohn Verlag ISBN13: 9783433014523 .
- SzilvÁgyi, Z. (2010). New development in geotechnical numerical calculations. In *Geotechnical Engineering 20: View of Young European Geotechnical Engineers* (pp. 72-77). Brno: Academic Publishing CERM Ltd.
- SzilvÁgyi, Z. (2012). Dinamikus talajparaméterek meghatározása. In *Tavaszi Szél 2012 Konferenciakötet* (pp. 458-465). Budapest: Doktoranduszok Országos Szövetsége.
- SzilvÁgyi, Z., & Ray, R. (2018). Verification of the Ramberg-Osgood Material Model in Midas GTS NX with the Modeling of Torsional Simple Shear Tests (accepted for publication). In *Periodica Polytechnica Civil Engineering Volxy* (pp. 1-7). <https://doi.org/10.3311/PPci.xyzw>.
- SzilvÁgyi, Z., Hudacsek P., Ray, R.P. (2016). Soil shear modulus from Resonant Column, Torsional Shear and Bender Element Tests. In *International Journal of Geomate 10:(2)* (pp. 1822-1827). <https://doi.org/10.21660/2016.20.39871> .
- SzilvÁgyi, Z., Panuska, J., & Ray, R. (2018). Laboratory Measurement, Analysis, and Comparison of Small Strain Modulus in Danube Sands with Plastic Fines by Resonant Column and Bender Elements (accepted for publication). In *Earthquake Engineering and Engineering Vibration Volxy* (pp. 1-26). ISSN 1993-503X.

- Szilvgyi, Z., Panuska, J., Kegyes-Brassai, O., Wolf, ., Tildy, P., & Ray, R. (2017). Ground Response Analyses in Budapest Based on Site Investigations and Laboratory Measurements. In *International Journal of Environmental, Chemical, Ecological, Geological and Geophysical Engineering Vol11(4)* (pp. 307-317). <http://waset.org/publications/10006887>.
- Szilvgyi, Z., Ray, R. P. (2015). Seismic performance evaluation of an irregular RC frame building. In *Geotechnical Engineering for Infrastructure and Development: XVI European Conference on Soil Mechanics and Geotechnical Engineering* (pp. 4185-4190). Edinburgh: ICE Publishing.
- Szilvgyi, Z., Ray, R. P., & Wolf, . (2014). tfog tervezi szemlletre van szksg a fldrengsre val mretezshez. In *ptsi Megoldsok - Szerkezetek, Technolgik, ptanyagok 3.* (pp. 4-5).
- Tatsuoka, F., Iwasaki, T., & Takagi, Y. (1978). Hysteretic damping of sand under cyclic loading and its relation to shear modulus. In *Soils and Foundations Vol 18(2)* (pp. 25-40). Japanese Society of Soil Mechanics and Foundation Engineering https://doi.org/10.3208/sandf1972.18.2_25.
- Tatsuoka, F., Iwasaki, T., Yoshida, S., Fukushima, S., & Sudo, H. (1979). Shear modulus and damping by drained tests on clean sand specimen reconstituted by various methods. In *Soils and Foundations, Vol19(1)* (pp. 39-54). Japanese Society of Soil Mechanics and Foundation Engineering <https://doi.org/10.3208/sandf1972.19.39>.
- Ther, T., & Kollr, L. (2017). Refinement of Housner's model on rocking blocks. In *Bulletin of Earthquake Engineering 15(5)* (pp. 2305-2319).
- Trs, E. (2006). A szeizmikus mdszer geotechnikai alkalmazsainak kritikai vizsglata. In *PhD Dissertation* (pp. 1-118). Sopron, Hungary.
- Vucetic, M. (1994). Cyclic threshold shear strains in soils. In *Journal of Geotechnical Engineering 120* (pp. 2208-2228). [https://doi.org/10.1061/\(ASCE\)0733-9410\(1994\)120:12\(2208\)](https://doi.org/10.1061/(ASCE)0733-9410(1994)120:12(2208)).
- Vucetic, M., & Dobry, R. (1991). Effect of soil plasticity on cyclic response. In *Journal of Geotechnical Engineering, ASCE, Vol 117* (pp. 89-107). [https://doi.org/10.1061/\(ASCE\)0733-9410\(1991\)117:1\(89\)](https://doi.org/10.1061/(ASCE)0733-9410(1991)117:1(89)).
- Wichtmann, T., & Triantafyllidis, T. (2004). Influence of a cyclic and dynamic loading history on dynamic properties of dry sand, Part i: cyclic and dynamic torsional prestraining. In *Soil Dynamics and Earthquake Engineering, 24(2)* (pp. 127-147). <https://doi.org/10.1016/j.soildyn.2003.10.004>.

- Wichtmann, T., & Triantafyllidis, T. (2009). Influence of the grain-size distribution curve of quartz sand on the small strain shear modulus G_{max} . In *Journal of the Geotechnical and Geoenvironmental Engineering* 135(10) (pp. 1404-1418). [https://doi.org/10.1061/\(ASCE\)GT.1943-5606.0000096](https://doi.org/10.1061/(ASCE)GT.1943-5606.0000096).
- Wichtmann, T., & Triantafyllidis, T. (2009). On the correlation of "static" and "dynamic" stiffness moduli of non-cohesive soils. In *Bautechnik* 86, Special Issue SI "Geotechnical Engineering" (pp. 28-39). <https://doi.org/10.1002/bate.200910039>.
- Wichtmann, T., & Triantafyllidis, T. (2013). Effect of uniformity coefficient on G/G_{max} and damping ratio of uniform to well graded quartz sands. In *Journal of Geotechnical and Geoenvironmental Engineering* Vol 139(1) (pp. 59-72). [https://doi.org/10.1061/\(ASCE\)GT.1943-5606.0000735](https://doi.org/10.1061/(ASCE)GT.1943-5606.0000735).
- Wichtmann, T., Navarrete Hernandez, M., & Triantafyllidis, T. (2015). On the influence of a non-cohesive fines content on small strain stiffness, modulus degradation and damping of quartz sand. In *Soil Dynamics and Earthquake Engineering* Vol69 No. 2. (pp. 103-114). <https://doi.org/10.1016/j.soildyn.2014.10.017>.
- Wolf, .., & Ray, R. P. (2017). Comparison and Improvement of the Existing Cone Penetration Test Results - Shear Wave Velocity Correlations for Hungarian Soils. In *International Journal of Environmental, Chemical, Ecological, Geological and Geophysical Engineering* 11:(4) (pp. 338-347). World Academy of Science Engineering and Technology.
- Wu, S., Gray, D., & Richart, j. F. (1984). Capillary effects on dynamic modulus of sands and silts. In *Journal of Geotechnical Engineering* Vol110(9) (pp. 1188-1203). [https://doi.org/10.1061/\(ASCE\)0733-9410\(1984\)110:9\(1188\)](https://doi.org/10.1061/(ASCE)0733-9410(1984)110:9(1188)).
- Yang, J., & Gu, X. (2013). Shear stiffness of granular material at small strains: does it depend on grain size? In *Geotechnique* 63(2) (pp. 165-179). <https://doi.org/10.1680/geot.11.P.083>.
- Youn, J., Choo, Y., & Kim, D. (2008). Measurement of small-strain shear modulus G_{max} of dry and saturated sands by bender element, resonant column, and torsional shear tests. In *Canadian Geotechnical Journal* 45 (pp. 1426-1438). <https://doi.org/10.1139/T08-069%20>.
- Zhang, J., Andrus, R., & Juang, C. (2005). Normalized Shear Modulus and Material Damping Ratio Relationships. In *Journal of Geotechnical and Geoenvironmental Engineering* Vol131 (pp. 453-464). [https://doi.org/10.1061/\(ASCE\)1090-0241\(2005\)131:4\(453\)](https://doi.org/10.1061/(ASCE)1090-0241(2005)131:4(453)).

Zsarnóczy, Á. (2014). Experimental and Numerical Investigation of Buckling Restrained Braced Frames for Eurocode Conform Design Procedure Development. In *PhD Dissertation, Pál VásÁrhelyi Doctoral School of Civil Engineering and Earth Sciences* (pp. 1-147). Budapest University of Technology and Economics http://www.omikk.bme.hu/collections/phd/Epitomernoki_Kar/2014/Zsarnoczay_Adam/ertekezes.pdf.

List of figures

Figure 2-1 Ratio of dynamic and static moduli presented by (Alpan, 1970)	6
Figure 2-2 External and local measurements in a triaxial test: setup (left) and deviatoric stress-strain curves with zoom into small strains (right) (Puzrin, 2012)	6
Figure 2-3 Stiffness degradation of soil with typical strain ranges after	8
Figure 2-4 Seismic waves (original image by Prof. L. Braile )	8
Figure 2-5 Propagation of shear waves in layered medium and induced deformation	9
Figure 2-6 Deviatoric stress-strain curve: true (left) and normalized (right) (Puzrin, 2012)...	11
Figure 2-7 Nonlinear stress-strain curve for initial loading and hysteresis curve for cyclic loading	12
Figure 2-8 Secant shear modulus and tangent shear modulus	14
Figure 2-9 Hysteresis loop of one cycle showing dissipated energy W_D , and equivalent elastic strain energy W_S	15
Figure 2-10 Hysteresis loops at different strain levels due to harmonic cyclic loading	16
Figure 2-11 Hysteresis loops in symmetric (a) and irregular loading (b) according to the extended Masing rules (redrawn from (Benz, 2006), after (Pyke, 1979)).....	18
Figure 2-12 Stress-strain curves obtained with the Ramberg-Osgood model.....	19
Figure 2-13 Normalized secant and tangent modulus vs. strain obtained with the Ramberg-Osgood model.....	20
Figure 2-14 Mohr diagram for maximum shear stress	21
Figure 2-15 Reduction factor B to account for higher C_U and FC obtained	30
Figure 2-16 Effect of plasticity on the small strain shear modulus of mixtures of Ottawa sand with fines based on (Carraro, Prezzi, & Salgado, 2009). Note: Clayey sand is sand with plastic fines; silty sand is sand with nonplastic fines	33
Figure 2-17 Modulus reduction curves for sand	37
Figure 2-18 Modulus degradation curves for clays and sand ($PI=0$)	37
Figure 2-19 Effect of cyclic stiffness degradation on modulus reduction curves of clays and sand ($PI=0$) by (Vucetic & Dobry, 1991)	38
Figure 2-20 Best fit modulus degradation curves for sands by (Oztoprak & Bolton, 2013) ...	40
Figure 2-21 Damping curves for sand by (Seed & Idriss, 1970) and (Vucetic & Dobry, 1991)	43
Figure 2-22 Damping curves for clays and sand by (Vucetic & Dobry, 1991)	44
Figure 3-1 Combined Resonant Column – Torsional Shear Device (RC-TOSS).....	47

Figure 3-2 Cross section of RC-TOSS testing device	48
Figure 3-3 Raw RC testing data in the measurement controlling spreadsheet.....	52
Figure 3-4 Interpreted TOSS measurement data. Two confinement stages and several shear stress amplitudes are shown with cycle 1 and cycle 100.....	52
Figure 3-5 Effect of number of cycles in TOSS test	53
Figure 3-6 Stress-strain response to an irregular load history in TOSS test	54
Figure 3-7 Numerical integration for obtaining hysteretic damping with the Ramberg-Osgood material model	54
Figure 3-8 Modulus reduction curve obtained with Resonant Column-Torsional Simple Shear device.....	56
Figure 3-9 Hysteresis loops of Torsional Shear tests at different stress (strain) levels.....	57
Figure 3-10 Detail of finite element mesh of soil sample and steel ring (partially invisible)..	57
Figure 3-11 Distribution of horizontal stresses after confinement activation	60
Figure 3-12 Comparison of shear stresses in cross section	60
Figure 3-13 Stress-strain curve by FEM calculation and MIDAS Ramberg-Osgood.....	61
Figure 3-14 Deformed mesh at turnaround point of loading.....	61
Figure 3-15 Distribution of total displacements at turnaround point of loading.....	62
Figure 3-16 Shear strains at turnaround point of loading.....	62
Figure 3-17 Manual load stepping used for stable calculation of hysteresis loop	63
Figure 3-18 Hysteresis loop obtained with FEM calculation.....	63
Figure 3-19 Hysteresis loops obtained from two-way sequential loading in Midas	64
Figure 3-20 Modulus reduction curve by FEM calculation and RC-TOSS tests.....	64
Figure 4-1 Grain size curves for soils tested. (Note that P8 and B1(gr) were only tested by bender elements in the comparative study)	67
Figure 4-2 Effect of confinement time on G_{max}	70
Figure 4-3 Comparison of dry and fully saturated test.....	70
Figure 4-4 Small strain stiffness of all samples measured by RC. (Soils with $FC > 7\%$ are shown with circles).....	71
Figure 4-5 G_{max} normalized by void ratio function vs. confinement for all samples.	73
Figure 4-6 G_{max} normalized by confinement function vs. void ratio for all samples.	73
Figure 4-7 Measured vs. estimated G_{max} using the correlation obtained in this study for all samples in Table 4-4. Ranges of $\pm 15\%$ are given with dotted lines.....	75
Figure 4-8 Measured vs. estimated G_{max} using the correlations given by (Carraro, Prezzi, & Salgado, 2009) in Table 2-2. Ranges of $\pm 15\%$ are given with dotted lines	76

Figure 4-9 Measured vs. estimated G_{max} using the correlation given by (Biarez & Hicher, 1994) in Table 2-3. Ranges of $\pm 15\%$ are given with dotted lines	77
Figure 4-10 Measured vs. estimated G_{max} using the correlations given by (Wichtmann & Triantafyllidis, 2009) and (Wichtmann, Navarrete Hernandez, & Triantafyllidis, 2015) in Equations 2-26 to 2-29. Ranges of $\pm 15\%$ are given with dotted lines	78
Figure 4-11 Measured vs. estimated G_{max} using the correlation given by (Oztoprak & Bolton, 2013). Ranges of 200% and 50% are given with solid lines	79
Figure 4-12 Confinement and void ratio conditions in the comparative study	80
Figure 4-13 Comparison of G_{max} measured with BE and RC in this study.....	81
Figure 4-14 Comparison of G_{max} measured with BE and RC in literature.....	82
Figure 4-15 Modulus reduction curve for Sample P1 with RO fit.....	86
Figure 4-16 Modulus reduction compared to correlations for Sample P1	86
Figure 4-17 Modulus reduction curve for Sample P2 with RO fit.....	87
Figure 4-18 Modulus reduction compared to correlations for Sample P2	87
Figure 4-19 Modulus reduction curve for Sample P3 with RO fit.....	88
Figure 4-20 Modulus reduction compared to correlations for Sample P3	88
Figure 4-21 Modulus reduction curve for Sample P4 with RO fit.....	89
Figure 4-22 Modulus reduction compared to correlations for Sample P4	89
Figure 4-23 Modulus reduction curve for Sample P5 with RO fit.....	90
Figure 4-24 Modulus reduction compared to correlations for Sample P5	90
Figure 4-25 Modulus reduction curve for Sample P6 with RO fit.....	91
Figure 4-26 Modulus reduction compared to correlations for Sample P6	91
Figure 4-27 Modulus reduction curve for Sample P7 with RO fit.....	92
Figure 4-28 Modulus reduction compared to correlations for Sample P7	92
Figure 4-29 Modulus reduction curve for Sample B1 with RO fit	93
Figure 4-30 Modulus reduction compared to correlations for Sample B1	93
Figure 4-31 Modulus reduction curve for Sample B2 with RO fit	94
Figure 4-32 Modulus reduction compared to correlations for Sample B2.....	94
Figure 4-33 Modulus reduction curve for all samples with RO fit	95
Figure 4-34 RO curves for each soil and the fit for all soils	96
Figure 4-35 Damping curve for Sample P1 compared to correlations.....	99
Figure 4-36 Measured vs. estimated values for damping with RO fit for Sample P1.....	99
Figure 4-37 Damping curve for Sample P2 compared to correlations.....	100
Figure 4-38 Measured vs. estimated values for damping with RO fit for Sample P2.....	100

Figure 4-39 Damping curve for Sample P3 compared to correlations.....	101
Figure 4-40 Measured vs. estimated values for damping with RO fit for Sample P3.....	101
Figure 4-41 Damping curve for Sample P4 compared to correlations.....	102
Figure 4-42 Measured vs. estimated values for damping with RO fit for Sample P4.....	102
Figure 4-43 Damping curve for Sample P5 compared to correlations.....	103
Figure 4-44 Measured vs. estimated values for damping with RO fit for Sample P5.....	103
Figure 4-45 Damping curve for Sample P6 compared to correlations.....	104
Figure 4-46 Measured vs. estimated values for damping with RO fit for Sample P6.....	104
Figure 4-47 Damping curve for Sample P7 compared to correlations.....	105
Figure 4-48 Measured vs. estimated values for damping with RO fit for Sample P7.....	105
Figure 4-49 Damping curve for Sample B1 compared to correlations	106
Figure 4-50 Measured vs. estimated values for damping with RO fit for Sample B1	106
Figure 4-51 Damping curve for Sample B2 compared to correlations	107
Figure 4-52 Measured vs. estimated values for damping with RO fit for Sample B2	107
Figure 4-53 Measured damping values from all samples compared to correlations.....	108
Figure 4-54 Measured damping values from all samples with RO fit	108
Figure 4-55 Measured vs. estimated values for damping with RO fit for each soil tested in this study.....	109
Figure 4-56 Measured vs. estimated values of damping with Equation 5-4	110

List of symbols

a	Curve fitting coefficient
a_{peak}	Peak acceleration
A	Curve fitting coefficient
A_{loop}	Area of hysteresis loop
b	Parameter used to define general Ramberg-Osgood relationship
B	Reduction factor of G_{max} to account for fines content
c'	Cohesion
c_1	Coefficient used in Damping correlations
c_2	Coefficient used in Damping correlations
C	Ramberg-Osgood model parameter
Cl	Mass percentage of clay particles in sample
C_U	Uniformity coefficient
d_{peak}	Peak displacement
d_{10}	Effective particle diameter
d_{50}	Mean or average particle diameter
d_{60}	Particle diameter at which 60% of a sample's mass is comprised of smaller particles
D	Damping ratio
D_i	Inner diameter of sample
D_o	Outer diameter of sample
D_r	Relative density
e	Void ratio
e_{max}	Maximum void ratio
e_{min}	Minimum void ratio
$e_{rel,avg}$	Average of relative errors
$ e_{rel} _{avg}$	Average of absolute values of relative errors
E_d	Dynamic modulus
E_s	Static modulus of elasticity
f_1	Function used for numerical integral of damping
f_2	Function used for numerical integral of damping
$F(e)$	Void ratio function

FC	Fines content
G	Shear modulus
G_0 or G_{max}	Maximum shear modulus or very small strain shear modulus
G_{sec}	Secant shear modulus
G_{tan}	Tangent shear modulus
h_{max}	Ramberg-Osgood model parameter in Midas formulation
I	Mass polar moment of inertia of sample
I_p	Plasticity index of fine particles in sample
I_0	Mass polar moment of inertia of device
I_D	Density index
k	Curve fitting coefficient
K_0	Jaky's at rest earth pressure coefficient
$K_{2,max}$	Coefficient for G_{max} estimation
L	Height of sample
n	Curve fitting coefficient
N	Number of load cycles
N_G	Material constant accounting for cyclic increase of G_{max}
OCR	Over-consolidation ratio
p'	Mean effective stress
p_a or p_{atm}	Atmospheric pressure
PI	Plasticity index
q	Deviatoric stress
q_L	Deviatoric limiting stress
q_y	Deviatoric yield stress
R	Ramberg-Osgood model parameter
R^2	Coefficient of determination
Si	Mass percentage of silt particles in sample
v_p	P-wave velocity
v_s	Shear wave velocity
w_l	Liquid limit
w_{max}	Maximum water content
w_p	Plastic limit
W_D	Dissipated energy

W_S	Maximum strain energy of equivalent elastic material
x	Function used to define Ramberg-Osgood relationship
y	Argument of function used to define Ramberg-Osgood relationship
z_N	Acceleration amplitude at cycle N
Z	Acceleration amplitude reading

α	Ramberg-Osgood model parameter
β	Ramberg-Osgood model parameter in Midas formulation/device constant
δ	Logarithmic decrement
ϵ_1	Major principal strain
ϵ_3	Minor principal strain
ϵ_s	Shear strain (in triaxial stress state)
ϵ_{sr}	Relative shear strain (in triaxial stress state)
ϵ_{sL}	Limiting shear strain (in triaxial stress state)
φ'	Friction angle
γ or γ_s	Shear strain
γ_c	Cyclic shear strain
γ_d	Dry density
γ_e	Elastic threshold strain
γ_p or γ_l	Shear strain at turnaround point
γ_r or γ_{ref}	Reference shear strain
$\gamma_{ref,1}$	Reference shear strain at 100 kPa confinement
γ_{static}	Static shear strain
ν	Poisson's ratio
ρ	Density
ρ_s	Specific density
σ'_0	Average confinement pressure
σ_1	Major principal normal stress
σ_3	Minor principal normal stress
σ_v	Effective vertical overburden pressure
τ	Shear stress

τ_{max}	Shear strength
τ_p or τ_l	Shear stress at turnaround point
τ_{static}	Static shear stress
ω_n	Resonant frequency